Optical measurement of partially specular surfaces by combining pattern projection and deflectometry techniques

Masterarbeit

im Studiengang Elektrotechnik und Informationstechnik

Vertiefungsrichtung Photonik

an der

vorgelegt von

Marc Philipp Sandner

Matrikelnummer: 8514895

Datum der Abgabe:	15.01.2015
Erstgutachter:	Prof. Dr. rer. nat. Jürgen Jahns (Fernuniversität Hagen)
Zweitgutachter:	Dr. rer. nat. Jan Burke (BIAS)

Ich erkläre, dass ich die vorliegende Masterarbeit selbstständig und ohne unzulässige Inanspruchnahme Dritter verfasst habe. Ich habe hierbei nur die angegebenen Quellen und Hilfsmittel verwendet und die aus diesen wörtlich, inhaltlich oder sinngemäß entnommenen Stellen als solche den wissenschaftlichen Anforderungen entsprechend kenntlich gemacht. Die Versicherung selbstständiger Arbeit gilt auch für Zeichnungen, Skizzen oder graphische Darstellungen. Die Arbeit wurde bisher in gleicher oder ähnlicher Form weder derselben noch einer anderen Prüfungsbehörde vorgelegt und auch noch nicht veröffentlicht.

Bremen, 15.01.2015

Marc Philipp Sandner

Zusammenfassung

Geometrisch-optische Phasenmesstechniken (GOP) können zur schnellen, kontaktlosen, hochpräzisen sowie robusten Oberflächenmessung verwendet werden. Die GOP Streifenprojektion und Phasenmessende Deflektometrie sind jeweils für die Messung von diffus reflektierenden sowie glänzend reflektierenden Oberflächen konzipiert. Technische Oberflächen sind jedoch im Allgemeinen gleichzeitig diffus sowie glänzend reflektierend und lassen sich dadurch nicht in eine dieser beide Kategorien einordnen. Gerade bei technischen Oberflächen müssen umfangreiche Voruntersuchungen durchgeführt werden um zu bestimmen ob Streifenprojektion oder Phasenmessende Deflektometrie die geeignete Messmethode ist. Die Messung von Oberflächen mit unbekannten oder räumlich variiendenden Reflexionseigenschaften mittels einer einzelnen GOP ist bislang nicht möglich.

In dieser Arbeit wird eine neuartige, kombinerte GOP zur Messung von technischen und anderen Oberflächen mit gemischtem Reflexionsverhalten präsentiert, die auf einer Fusion der Messdaten aus Streifenprojektion und Phasenmessender Deflektometrie beruht. Nach Darlegung des zugrundeliegenden Prinzips der geometrisch-optischen Phasenmessung und der Bedeutung der Messparameter wird der neuartige Auswertealgorithmus beschrieben und Messungen mittels der entwickelten GOP präsentiert.

Abstract

Geometric-optical phase measuring metrology techniques (GOP) can be used for fast, contactless, highly precise and robust surface measurement. The GOPs Fringe Projection and Phase Measuring Deflectometry are designed for the measurement of diffusely reflective and specularly reflective surfaces respectively. Technical surfaces however usually show both specular and diffuse reflective behavior and thus cannot be assigned to a single of these classes. Especially for technical of surfaces, deciding whether to use Fringe Projection or Phase Measuring Deflectometry for measurement requires extensive testing. Measurement of surfaces with unknown reflective characteristics or with spatially varying reflective characteristics using a single one of these techniques is not feasible.

In this work, a novel combined GOP for the measurement of technical or other surfaces with mixed reflective characteristics is presented, which involves the fusion of measurement data from Fringe Projection and Phase Measuring Deflectometry measurements. After explaining the basic principle of geometric-optical phase measuring and the importance of the measurement parameters, the novel algorithm is described and measurements with a combined GOP setup are presented.

Contents

1 Introduction

With rising automation in many production environments, means of automatically measuring the quality of the produced parts gets more important. In contrast to visual inspection, machine-based inspection and measurement is robust, fast and gives an exact description of physical properties of the measured parts, such as geometric features. For contemporary production processes the need for metrology techniques, and the demands concerning measurement uncertainty and precision are rising in the course of *Six Sigma* quality management [Pyz03] and *Zero Defect production* [MegF]. Besides quality control, the data generated by in-line (in production line) and on-line (bypass of specimen, measurement close to the production line) [Kes06] object surface measurement in production systems can also be used for in-process control. In the recently concluded EU project MEGaFiT [MegF], a closed loop control system for production has been built in which deviations in the measured object shape data are consolidated with a model of the production process for readjustment of the manufacturing tool's process parameters.

Optical metrology techniques are contactless, non-destructive and have the capability of providing measurement data with high spatial resolution, which is why they can be considered as a premium choice for measurements of parts in quality assurance. In the domain of optical metrology techniques, *geometric-optical phase measurement* (GOP) techniques have the advantage of being very robust against environmental pertubations such as vibrations, air turbulences and temperature gradients, which make them very well suitable for industrial production environments. The GOP techniques of *Phase Measuring Deflectometry* (PMD) and *Fringe Projection* (FP) can be used for fast, full-frame measurement of objects of different sizes and shapes. An overview of use cases for PMD is shown in Figure 1.

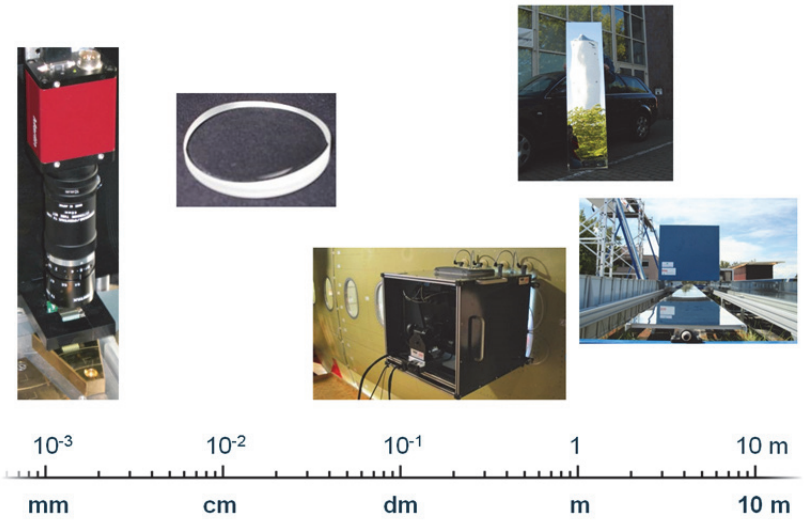

Figure 1: The geometric-optical phase measurement technique (GOP) Phase Measuring Deflectometry (PMD) can be used for shape measurement of objects with measurement field sizes in a large range, from millimeters (leftmost image, microproduction part) to meters (rightmost image, parabolic reflector for usage as solar thermal concentrator).

Despite the advantages of GOP techniques, they are limited to different classes of object surfaces that can be measured with them. While specular, partly reflective surfaces can be measured with PMD, partly scattering surfaces can be measured with FP [Bau08]. As most technical surfaces show hybrid (i.e. locally mixed) specularly reflective and scattering behavior [Sch96], choosing the correct GOP technique usually requires test measurements with both techniques and measurement parameter optimization. For the areal shape measurement of objects with spatially varying reflective behavior, neither of the techniques can be used.

In this work, a novel combined FP / PMD measurement technique is presented which can be used for measurement of surfaces with hybrid or spatially varying reflective behavior. The assembly and calibration of a combined FP / PMD setup is described and results from shape calculation based on the developed *Hybrid Reflectometry regularization* (HRR) [San14] data fusion approach is presented.

2 State of the art

Before characterizing geometric-optical phase measurement techniques, a short description of optical reflection is given in order to clarify the relationship between different approaches of geometric-optical phase measurement and reflective properties of surfaces.

2.1 Scalar reflection properties of surfaces

For a plane electromagnetic wave in vacuum, the direction of propagation is given by the Poynting vector ***S*** [Hec01] which is described by:

$$\boldsymbol{S} = \frac{1}{\mu_0}\, \boldsymbol{E} \times \boldsymbol{B}\,, \tag{1}$$

with the vacuum permeability μ_0, the electric field ***E*** and the magnetic field ***B***. If an electromagnetic wave approaches a single interface of media with different refractive indices n_i, part of the wave is transmitted and part of it is reflected, see Figure 2.

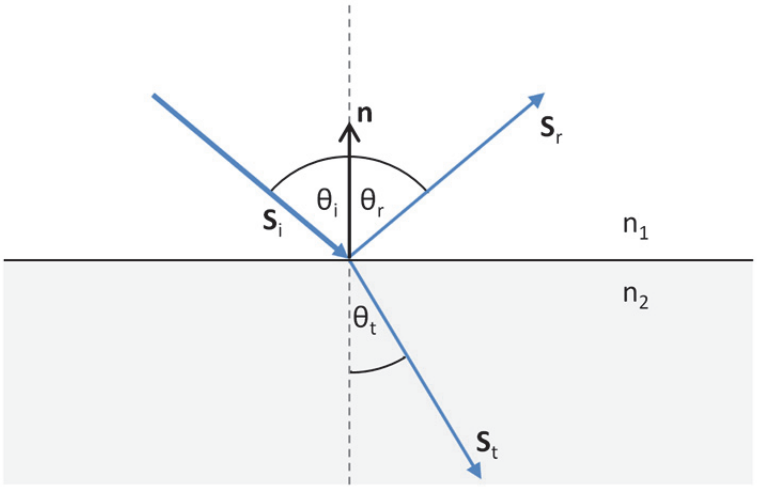

Figure 2: Reflection and transmission of incident electromagnetic wave with Poynting vector S_i at the interface between media with refractive indices n_1 and n_2, for $n_2 > n_1$. Angles of reflection and transmission are defined towards the normal axis defined by the normal vector *n* perpendicular to the interface.

The incident angle θ_i and reflection angle θ_r are defined as the angle of Poynting vectors of incident and reflected waves to the surface normal ***n***. From Fermat's principle, it can be shown that the following relationship between incident angle θ_i and reflection angle θ_r holds:

$$\theta_r = -\theta_i\,. \tag{2}$$

In general, the amplitude and polarization of the reflected and transmitted waves are dependent on the incident angle θ_i. For dielectric ($\mu \approx \mu_0$), linear, isotropic, homogeneous and non-dispersive media, the ratio of incident to reflected amplitude is given by the Fresnel

coefficients r_{TE} and r_{TM} for transversal electric[1] and transversal magnetic polarization, respectively [Sal91]:

$$r_{TE} = \frac{n_1 \cdot \cos(\theta_i) - n_2 \cdot \cos(\theta_t)}{n_1 \cdot \cos(\theta_i) + n_2 \cdot \cos(\theta_t)} \quad , \quad r_{TM} = \frac{n_2 \cdot \cos(\theta_i) - n_1 \cdot \cos(\theta_t)}{n_2 \cdot \cos(\theta_i) + n_1 \cdot \cos(\theta_t)} , \tag{3}$$

$$with \ \cos(\theta_t) = \sqrt{1 - \left(\frac{n_1}{n_2}\right)^2 \cdot \sin^2(\theta_i)} \, . \tag{4}$$

For metallic surfaces, no light is transmitted and the amplitude of the reflected wave has a weaker dependence on the incident angle [Hec01].

If polarization of the wave and time dependence is neglected, the field can be described as a scalar function $U(z_p)$, depending on propagation distance z_p. If additionally a single wave with infinitely small wavelength is assumed, diffractive phenomena can be neglected and the wave propagates linearly in direction of ***S***, suggesting the propagation of the wave as a *ray* of light. The domain in optics which utilizes this concept of rays of light is called *geometrical* or *ray optics*. As in the scope of this work, effects related to polarization and spectral properties of light fields are not regarded, in the following the description of specular reflection will be based on the concept of ray optics.

An interface of different media can be found at the surface of an object surrounded by a homogeneous medium, such as air. The geometric structure of such an object surface has a dominant influence on its reflective behavior. A coarse classification of object surfaces by their geometric structure can be performed by labeling surfaces as being *smooth* or *rough*. From definitions of surface shape components from DIN 4760 [DIN82] and DIN EN ISO 4287 [DEI98], depicted in Table 1, roughness is the surface's microstructure, which itself is divided into subclasses.

Table 1: Shape components following definitions in norm DIN 4760 [DIN82], filters defined in DIN EN ISO 11562 [DEI98b] as phase-preserving high pass, low pass or band pass filters with cut-off wavelength Λ_c [Jung10]

Shape component	Description	Wavelengths Λ_c (structure period)
Form 	Macroscopic shape component: simple or complex geometric structures	$\Lambda_c > 8$ mm
Waviness 	Deviations from form, with low spatial frequencies (often from manufacturing)	$\Lambda_c > 8$ mm
Roughness 	Microstructure (essential for optical reflectivity)	Depending on class: $\Lambda_{c1} < 0.08$ mm, up to $\Lambda_{c5} < 8$ mm

[1] Electromagnetic waves with the electric field vector ***E*** perpendicular to the plane on incidence are defined as *transversal electric* (TE), waves with ***E*** in the plane of incidence are defined as *transversal magnetic* (TM).

For smooth surfaces, neighbored surface normals are almost parallel to each other. For real objects, this means that in small regions the surface has constant or near-constant local curvature. As shown in Figure 3a, for reflection of parallel rays of light at an ideally smooth (and also flat) surface the reflected rays of light are also parallel, which is called *directional reflection*. This makes the surface an ideal mirror, which in this context will be defined as mirrors for which reflection results in no or uniform modulation of the geometric relationship between the rays.

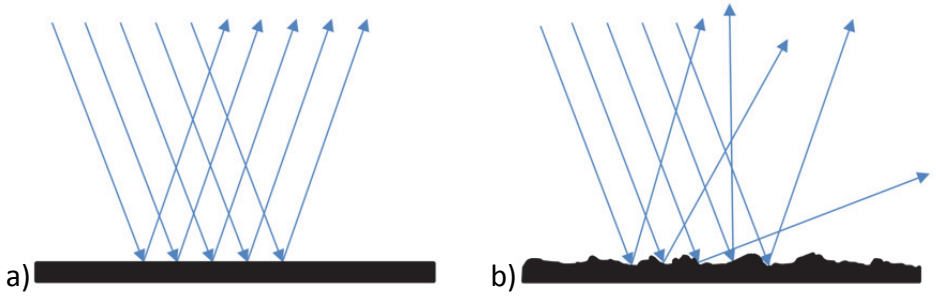

Figure 3: Reflection of light rays at test objects with different surface characteristics: a) Specular reflection at smooth surface; b) Non-directional reflection at a rough surface. For non-metallic surfaces, scattering in the volume of the test object occurs, because part of the incident electromagnetic field is transmitted through the object surface.

From this definition of smooth surfaces, rough surfaces can be defined as surfaces which cause a non-uniform modulation of the geometric relationship between the reflected rays. Reflection on a rough surface, as shown in Figure 3b, is also termed *diffuse* reflection or *scattering*. For rough dielectric and translucent media, also *volume scattering* occurs, where light is transmitted into the medium and reflected there. While ideally specularly reflective surfaces show no scattering (see Figure 4c), for ideally scattering objects, *Lambertian reflectance* occurs, where the incident light is scattered independent of its incident angle to the surface [Bor97] (see Figure 4a). Real surfaces however mostly show both directional and diffuse reflective behavior, shown in Figure 4b. Here, the light reflected has its maximum radiant intensity at a certain angle, which decreases for neighbored angles. The scattering lobe, shown in Figure 4 as dashed curves, shows the scattered angle-dependent radiant intensity. In the following description of the signal flow in a measurement system, for light reflected or scattered from a surface only the geometric-optical description is used.

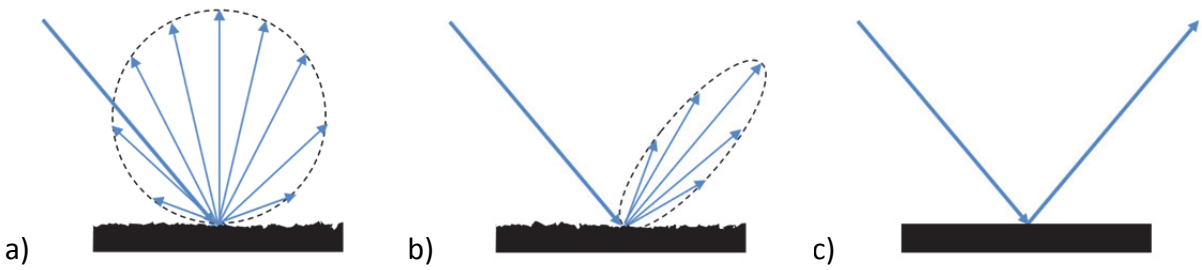

Figure 4: Reflective behavior and scattering lobe: a) Ideally diffuse Lambertian reflection: A rough surface (e.g. a piece of paper) scatters incident light isotropically, i.e. non-directionally; b) Partially diffuse reflection: A semi-rough surface directionally scatters light as indicated by the scattering lobe (dashed ellipse); c) Specular reflection: A smooth surface reflects incident light without scattering.

2.2 Geometric-optical phase measurement techniques (GOP)

Geometric-optical phase measurement techniques (GOP) are triangulation-based geometric-optical metrology techniques, which incorporate the measurement of the phase of a sinusoidal reference pattern. As shown in Figure 5, Phase Measuring Deflectometry (PMD) and (Phase Measuring) Fringe Projection (FP) are two GOP techniques. Mentioning the term ''*Phase Measuring*'' in the name of the techniques is used as a distinction to the deflectometric scanning technique also known as Small Angle Deflectometry [Ehr14], and other projective triangulation techniques using other reference patterns, such as Gray code [Wah86]. In this section, these two GOPs for surface shape measurement are characterized, including the measurement geometry, the requirements on the measurement surface, and different techniques for data evaluation.

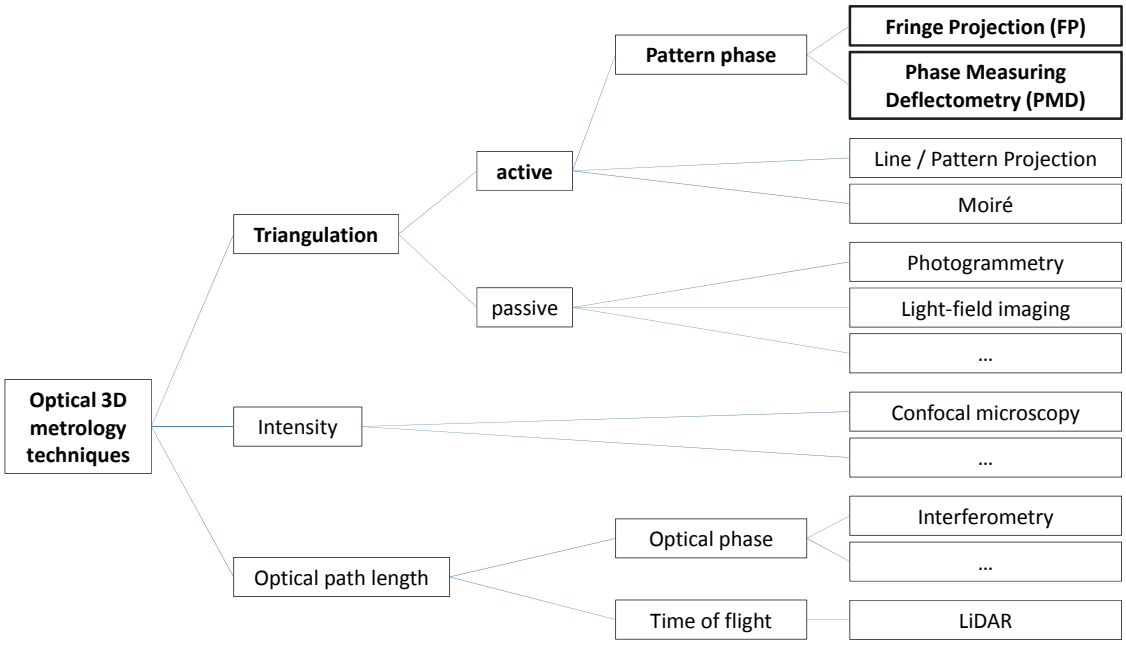

Figure 5: Overview of optical 3D metrology methods. The geometric-optical phase measurement techniques (GOP) (Phase Measuring) Fringe Projection and Phase Measuring Deflectometry can be classified as triangulation-based, active (meaning a reference pattern is used) reference pattern phase measuring techniques (from [Bey12], modified).

2.2.1 Geometric-optical phase measurement

As the term indicates, the physical description of light propagation in geometric-optical phase measurement techniques is based on the ray optics model. Since this model does not include a spectral description, the term *phase measurement* is not related to the measurement of the phase of an optical wave or of an optical path length. In GOP techniques, the signal source is a reference pattern with 1-dimensional or 2-dimensional [Li14] sinusoidal intensity modulation. As sinusoidal patterns are composed of a single spatial frequency, linear filtering of the pattern solely results in a scaling of the pattern modulation and the respective frequency peak in the spectrum, and does not lead to a substantial change of the pattern. Sinusoidal patterns are thus invariant to defocussing

which is advantageous for the measurement geometries in GOP setups. The object to be measured is illuminated with the light field from the signal source, and one or multiple imaging sensors capture the pattern which is deformed by either specular or diffuse reflection on the object surface, see Figure 6.

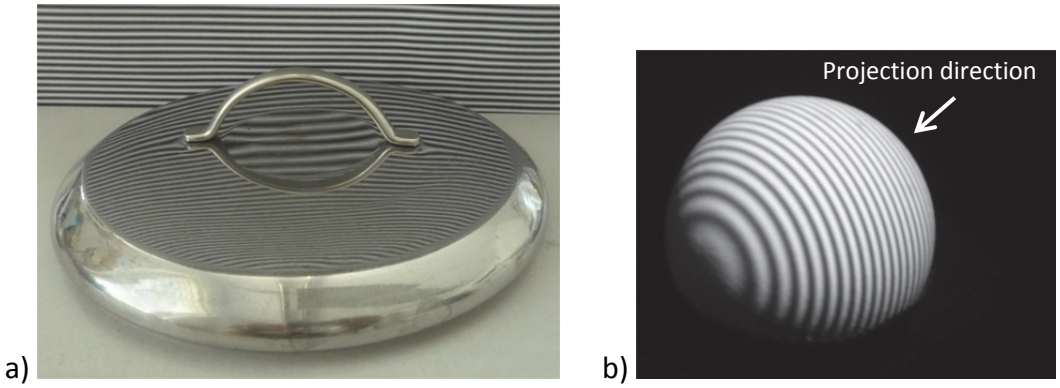

Figure 6: Deformation of straight sinusoidal fringe pattern induced by the object surface: a) Smooth object surface (saucepan lid), with part of the surface specularly reflecting a printed-out fringe pattern; b) Spherical object with rough surface, scattering a straight fringe pattern projected from the direction indicated by the white arrow.

In a broader sense, GOP techniques also include transmitted-light techniques [Fis14], but in the following only Phase Measuring Deflectometry (PMD) and Fringe Projection (FP) are considered, which are used to measure opaque objects. In phase measurement, a coordinate in the reference pattern plane is measured using the phase shifting technique, which consists of sequentially imaging and evaluating shifted sinusoidal reference patterns. Many algorithms for phase shifting are available; a popular variant known as the 4-step algorithm uses 4 reference patterns, which are shifted by a phase of π/2 (i.e. 1/4 of a wavelength of the sinusoidal pattern). For each sensor pixel coordinate (x,y), the recorded pattern phase φ(x,y) is calculated from the recorded intensities I_1(x,y), I_2(x,y), I_3(x,y) and I_4(x,y) from images I_1, I_2, I_3 and I_4 of the shifted patterns by [Cre88]:

$$\varphi(x,y) = \arctan\left(\frac{I_4(x,y)-I_2(x,y)}{I_1(x,y)-I_3(x,y)}\right). \tag{5}$$

The measurement of phase images in horizontal direction and calculation of the pattern phase is shown in Figure 7. From the acquired phase-shifted images in Figure 7a, the phase calculated from Eq. (5) is shown in Figure 7b. The calculated phase image has a dynamic range of [0, 2π], and a sawtooth-like appearance due to the restricted domain of the arctan function. Using *phase unwrapping* techniques [Nad96], multiples of 2π are systematically added to the values in the image in order to retrieve a continuous phase distribution. The demodulated phase image resulting from the phase unwrapping, shown in Figure 7b, is not limited to the range of [0, 2π] and encodes the absolute reference pattern position.

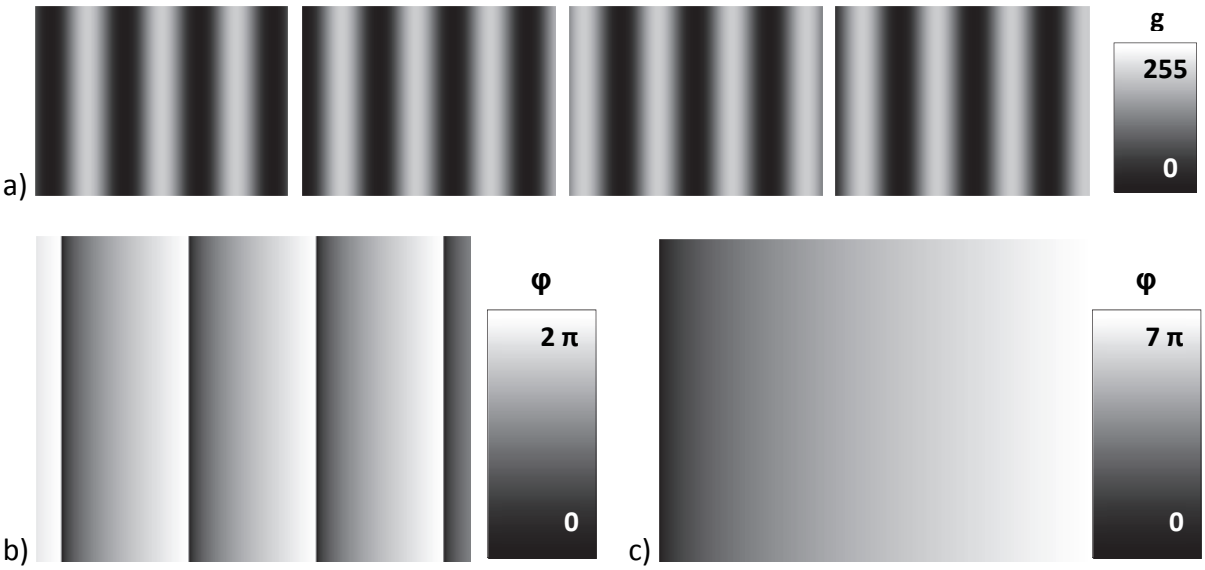

Figure 7: Phase measurement in horizontal direction using phase shifting technique: a) Simulated camera images (8 bit grayscale value *g*) of the sinusoidal reference pattern in initial and phase shifted states (4-step phase shift, π/2 per phase shift); b) Pattern phase *φ*(x,y) calculated from camera images; c) Demodulated phase image *φ*(x,y) with value range > 2 π, giving a spatially resolved mapping of the sensor pixels to (in this case horizontal) reference pattern coordinates.

If the phase measurement is performed in two perpendicular directions, two-dimensional pattern positions are retrieved for each sensor pixel. With a calibrated signal source, imaging sensor and scene geometry, the object's shape can be calculated from this phase mapping. An estimate for the uncertainty of the measured phase related to sensor noise can be retrieved by calculating the repeat accuracy from a measurement series, but also from parameters calculated from the images recorded in a single measurement [Fis12]. From the recorded intensities $I_n(x,y)$ for phase shift n, a shift angle α and a total count N of phase shifts, the fringe modulation M (dependence on (x,y) omitted in the following) can be calculated from [Bot08]:

$$M = \frac{2}{N} \cdot \sqrt{{M_s}^2 + {M_c}^2} \tag{6}$$

$$, with\ M_s = \sum_1^N I_n \cdot \sin(n \cdot \alpha)\ ,\quad M_c = \sum_1^N I_n \cdot \cos(n \cdot \alpha)\ .$$

M has a reciprocal dependence on the estimated signal-to-noise ratio $\varphi/\sigma\varphi$ (with noise given as standard deviation $\sigma\varphi$ of the measured phase value) of the measured phase:

$$\frac{\varphi}{\sigma\varphi} \propto M\ . \tag{7}$$

Thus, the modulation can be regarded as a pixelwise quality estimator of the phase measurement noise and, through error propagation, as an estimator of the uncertainty of the shape calculated from the measured phase.

2.2.2 Phase Measuring Deflectometry (PMD)

Phase Measuring Deflectometry (*PMD*), also known as *Raster* or *Fringe Reflection Technique*, is a GOP technique that is used for non-contact measurement of reflective or partially reflective surfaces [Ike81, San88, Bey97, Pet04, Kna04, Bot04, Bal10]. Deflectometry refers to using the reflection of a known reference pattern by the surface under test, which is commonly assumed to be perfectly specular. Slope changes of the surface lead to distortions of these fringes that can be evaluated quantitatively, which is why PMD is understood as a slope measurement technique. From the native slope data, an absolute shape can be calculated by numerical integration [Kna06], e.g. by using a Fourier transform approach [Fra88], or by performing a non-linear optimization [Bal12].

Figure 8 shows a typical PMD setup, consisting of a reference pattern display and a camera for capturing the virtual image that is generated by reflection of the reference pattern on the measured object. In order to achieve an optimal lateral resolution on the object surface and to avoid moiré effects between sensor and display pixels, the camera is usually not focused on the plane of the reference pattern display but in the object plane [Bal10]. Sinusoidal patterns thus are optimal for usage in PMD measurement, since they are invariant to defocussing (see section 2.2.1). For PMD systems, the mapping of camera pixels to reference pattern coordinates is facilitated by reflection from the measured surface. The result can be expressed in terms of a ray-of-sight vector $\boldsymbol{r}_s$ associated with a sensor pixel (obtained by camera calibration) and a monitor pixel position p_M, both in a common world coordinate system (obtained by calibrating the orientation of the reference pattern monitor with respect to the camera, see section 5.1.4).

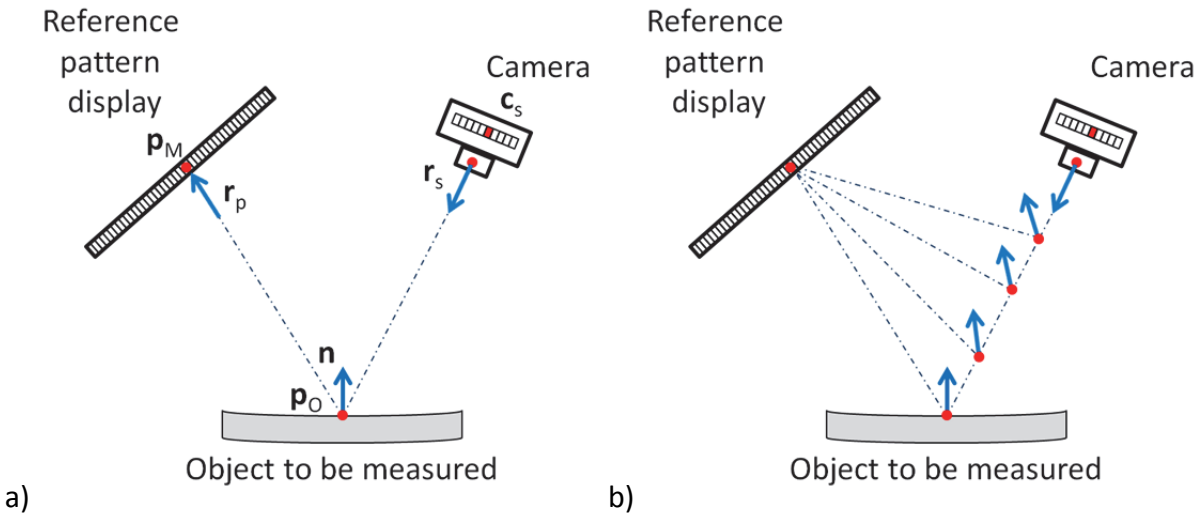

Figure 8: Principle of Phase Measuring Deflectometry (PMD) and inherent slope/distance ambiguity: a) In PMD phase measurement, the reference pattern is displayed on a TFT monitor. The camera records the virtual image of the reference pattern which is formed by reflection of the light emerging from the TFT monitor by the measurement object surface at point p_O. As a result of the phase measurement, a mapping between pixel coordinate c_s in the imaging sensor and pattern point p_M on the reference pattern display is retrieved; b) Without additional knowledge, the information from phase measurement and system calibration is ambiguous: As the reference pattern TFT monitor does not illuminate the object directionally, r_P is not known, which results in an ambiguity between distance and slope for every measured point. The mathematical description of this ambiguity is described in [Wer11] as the *Deflectometric Problem*.

For the calculation of the local object surface normal $\boldsymbol{n}$, knowledge of $\boldsymbol{r}_s$ and $\boldsymbol{p}_M$ alone is not sufficient. From [Bal10] and using the notation shown in Figure 8, the surface normal $\boldsymbol{n}$ is defined by:

$$\boldsymbol{n} = \frac{\boldsymbol{r}_p - \boldsymbol{r}_s}{|\boldsymbol{r}_p - \boldsymbol{r}_s|}, \qquad \boldsymbol{r}_p = \frac{\boldsymbol{p}_M - \boldsymbol{p}_O}{|\boldsymbol{p}_M - \boldsymbol{p}_O|}\ , \tag{8}$$

with $\boldsymbol{r}_p$ being the unit vector on the straight line connecting $\boldsymbol{p}_M$ with the point $\boldsymbol{p}_O$ at the intersection of the line of sight with the object surface. For an object surface with undefined position and thus unknown point of reflection on the object surface $\boldsymbol{p}_O$, equation (8) cannot be solved to calculate the local normal $\boldsymbol{n}$ without additional information. In this situation, for each sensor ray of sight $\boldsymbol{r}_s$ a set of normals is retrieved that includes exactly one correct normal $\boldsymbol{n}$, along with others related to incorrect location of $\boldsymbol{p}_O$ on $\boldsymbol{r}_s$.

In the past decades, research on PMD has targeted *deflectometric regularization* approaches (for definition see [Bal08, Bal10]) of using additional information which for calculating a unique and correct normals distribution on the object surface.

2.2.2.1 Retrieval of surface normals and shape from PMD phase data

Out of the regularization approaches described in [Bal10] and [Wer11], the most common approach is *Stereo PMD* [Kna04], which is based on simultaneous phase measurement with two cameras from different perspectives. To retrieve the object surface normals distribution, the two normal fields acquired from different perspectives as shown in Figure 9b, are matched using a global disparity measure [Bal10].

Although Stereo PMD works for the measurement of most surfaces, for some smooth concave surfaces multiple solutions to the normals distribution exist. An algorithm for the generation of such surfaces is given in [Wer11b].

Reference Distance regularization (RDR)

The *Reference Distance* or *FixedPoint* regularization (*RDR*) approach for PMD uses the knowledge of the distance d of a single point $\boldsymbol{p}_O$ on the surface to the entrance pupil of the camera [San13]. As can be seen in equation (8), with the knowledge of $\boldsymbol{p}_O$, the normal $\boldsymbol{n}$ at $\boldsymbol{p}_O$ can be calculated. With information about the height and surface normal at one point, the height of points in the area surrounding $\boldsymbol{p}_O$ can be estimated and the respective normals calculated, so that a distribution of normals on the whole surface can be generated iteratively, which is implemented using the Fourier transform approach. Different implementations of setting the object distance in measurement systems used for RDR PMD exist: An estimation of the distance d can either be performed by adjusting the object surface position or measurement with a distance sensor. In the following, the value d_z will be used (see Figure 9a) which is the component of d parallel to the z-axis of the reference plane coordinate system to be introduced in section 5.1.3.

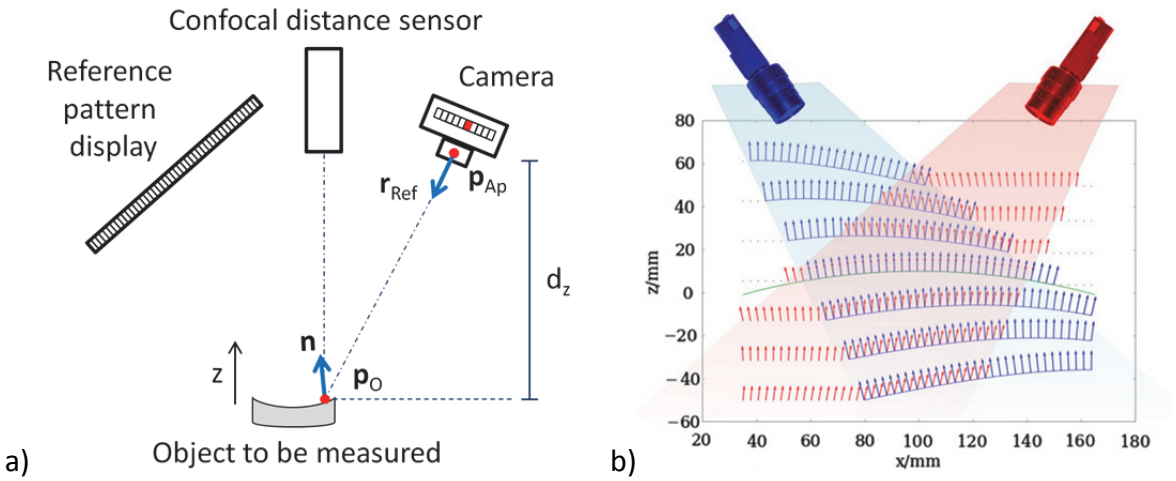

Figure 9: PMD regularization approaches for the deflectometric problem; a) Due to an unknown orientation of the ray of sight r_p emerging from the reference pattern display, a unique solution for the calculation of normal n at the viewed object point p_O cannot be retrieved without additional information. In the *Reference Distance* regularization (*RDR*) approach, the distance *d* between a single point p_O of the object surface to a center p_{Ap} of the camera lens aperture is assumed to be known (e.g. by measuring the distance indirectly with a confocal distance sensor), allowing calculation of normal *n* at p_O and, from this, iterative reconstruction of the normal distribution on the whole surface; Shown here is d_z, the component of *d* parallel to the z coordinate of the object reference plane coordinate system (see section 5.1.3) b) Stereo PMD: For an unknown object surface position, the object surface normals are retrieved by performing measurements with two cameras which each induce a separate normal field. In the intersection of the cones of sight of the cameras, a subset of the normals, representing the object surface normal distribution, is selected using a normal disparity measure (from [Bal10]).

For preparing the PMD setup to manual positioning of the object surface, two low-power laser pointers are added to the setup, and adjusted so that their beams intersect at a point in space, which by definition is taken to be in the measurement plane. This point, known as the system's reference point, is then implicitly measured in the system geometry orientation measurement (see section 5.1.3). Prior to measurement, the test object is then positioned so that the object's surface includes the reference point. Especially for specular surfaces, this procedure is complicated by the low intensity of light scattered from the surface. For the manual adjustment of the object surface, an uncertainty of ± 250 µm of the final object position and thus of d_z is expected [San11]. Using a confocal distance sensor for the measurement of d_z allows automation of the measurement with low measurement uncertainty for d_z in the range of ± 1 µm. As shown in [Li12], for RDR-based evaluation the uncertainty of d_z is crucial for the uncertainty of the calculated shape: the measurement error distribution $\Delta z(x,y)$ resulting from a deviation Δd_z between the estimated and actual object distance d_z is given by:

$$\Delta z(x) \approx \frac{\Delta d_z \cdot (x^2+y^2)}{2 \cdot {d_z}^2}. \tag{9}$$

An incorrect value for d_z thus results in a parabolic shape error, which was also shown experimentally in [San11], see Figure 10. In summary, for d_z with low uncertainty, shape data with very low uncertainty can be retrieved using RDR, which is shown also in the measurement example in Figure 11. As the shape calculation is based on the relationship between neighboring data points, RDR is only feasible for continuous surfaces.

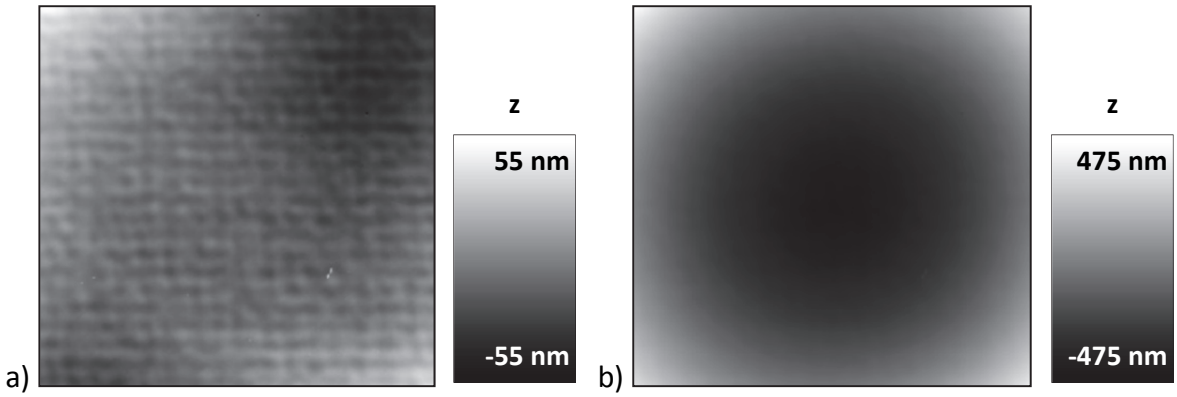

Figure 10: Shape data with tilt removed, from measurement of high-precision optical flat (λ/10 flatness deviation, lateral size: 47 x 50 mm²) with RDR PMD: a) When using a confocal distance sensor for measuring d_z with an uncertainty of ±1 µm, the resulting shape has a low dynamic range of 110 nm, which can be regarded as the measurement uncertainty; b) To mimic the uncertainty of ±250 µm for manual adjustment of d_z , the shape calculation was performed with an input value d_z which was 250 µm lower than the measured value. In the calculated shape, a parabolic error is present, which has a dynamic range of roughly 1 µm (from [San11]).

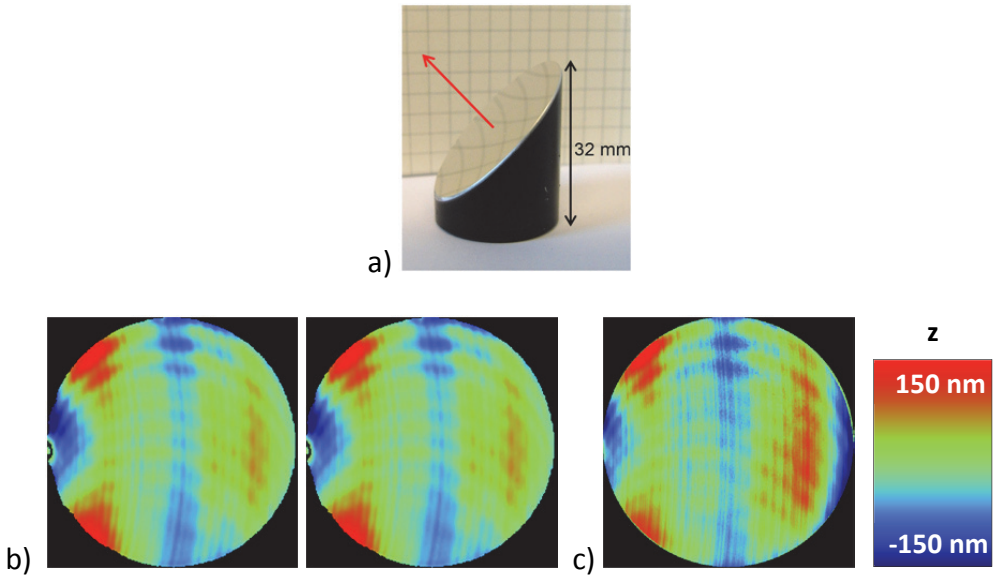

Figure 11: Measurement of a diamond-turned off-axis parabolic mirror with RDR PMD, using a confocal distance sensor for measurement of d_z : a) Photo of the measured object, with orientation of the optical axis of the confocal distance measurement sensor indicated by arrow on surface; b) Deviations from off-axis parabolic shape, measured with Fizzeau interferometer setups (viewing perspectives of 0°, 90° on the specimen), showing tooling traces; c) Deviations from off-axis parabolic shape, measured with PMD setup with confocal distance sensor (viewing perspective of 45° on the specimen), using RDR for shape calculation, laterally rescaled for comparability with images b. Lateral size of images in b and c: 24 mm (Data from [San11]).

Initial Shape regularization (ISR)

Another regularization approach for single-camera based PMD systems termed *Initial Shape* or *IniShape* regularization (*ISR*), uses a-priori knowledge about the object surface shape for interpretation of the measured phase values [San13]. Starting with an initial guess for the object distance d_z, a normals distribution is calculated from the measured phase and compared to the expected normals distribution from the a-priori model of the shape with a disparity measure, similar to the treatment in Stereo PMD. Iteratively, the estimated d_z is varied and the evaluation is repeated.

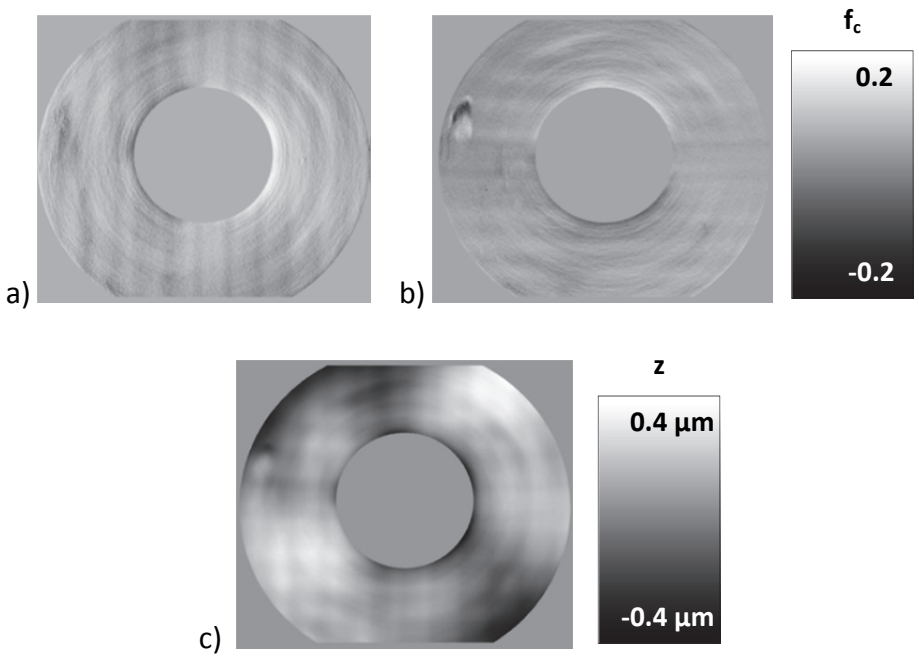

Figure 12: Reconstruction of a smooth parabolic object surface with unknown focal length using the Initial Shape regularization (ISR) with parabolic shape model; a) and (b) final cost functions f_c of the normal matching process: Deviation of x (left) and y (right) components of the calculated normals to the best-fit form (scale: relative units); c) Shape deviation to best-fit paraboloid (from [Bur13]).

The objective function for the optimization process is given by the mean disparity at different input d_z, guiding the sign and step width for choosing an estimate for d_z in the next iteration. While the a-priori shape model needs to be a parametric description of the object surface, shape parameters, such as the radius for a spherical shape model, do not have to be known. When convergence is reached, the calculated normal distribution is integrated using the Fourier transform approach. An example for an ISR shape reconstruction with a generic shape model is shown in Figure 12. The ISR algorithm has been shown to converge within a few iterations and to give satisfying results for the calculated shape but is not suitable for the measurement of objects with unknown shape and, as the RDR algorithm, for discontinuous surfaces.

2.2.3 Fringe projection (FP)

The term *Fringe Projection* (FP) is used for triangulation-based pattern projection profilometry techniques employing sinusoidal fringes as reference patterns. It is also a GOP technique and is used for non-contact measurement of diffusely scattering surfaces. In FP measurements, straight, sinusoidal fringes are projected on the measurement object [Hal89], and the light scattered on the object surface is recorded with one or multiple cameras. A typical FP setup with two cameras is shown in Figure 13a. As can be seen here, the object has to be at least partly scattering so that light coming from the projector reaches the cameras, making phase measurement possible. Specular reflections usually lead to oversaturation in the recorded image and result in artifacts in the measured phase. As shown in Figure 13b, after phase measurement and demodulation, a mapping of sensor pixels $\boldsymbol{c}_{s1}$ and $\boldsymbol{c}_{s2}$ to pattern positions $\boldsymbol{c}_p$ is coded in the recorded phase images. In contrast to

PMD, the phase pattern is projected directionally, so that from calibration of the cameras and the projector not only the rays of sight $\boldsymbol{r}_s$ for the camera sensor pixel positions $\boldsymbol{c}_s$ are known, but also the rays of sight $\boldsymbol{r}_p$ for the projector pixel positions $\boldsymbol{c}_p$. For the evaluation of the phase measurement, different methods exist [Bey12]. If the projector is calibrated, $\boldsymbol{r}_p$ is known and a surface point can either be calculated from intersection of $\boldsymbol{r}_{s1}$, $\boldsymbol{r}_{s2}$, or both with $\boldsymbol{r}_p$. As a substantial difference to PMD, the projected phase is constant with the object surface for all imaging perspectives on the object surface. This allows for a different evaluation scheme: If an uncalibrated projector is used, pixel positions $\boldsymbol{c}_{s1}$ and $\boldsymbol{c}_{s2}$ of common phase can be found in the images of both cameras, and the respective $\boldsymbol{r}_{s1}$, $\boldsymbol{r}_{s2}$ are intersected. By performing this triangulation for all recorded pattern positions, the surface shape is calculated in the volume generated by the intersection of the cones of sight of camera(s) and projector.

As an example, the shape retrieved from measurement of a scattering object (with highlights) using FP is shown in Figure 14.

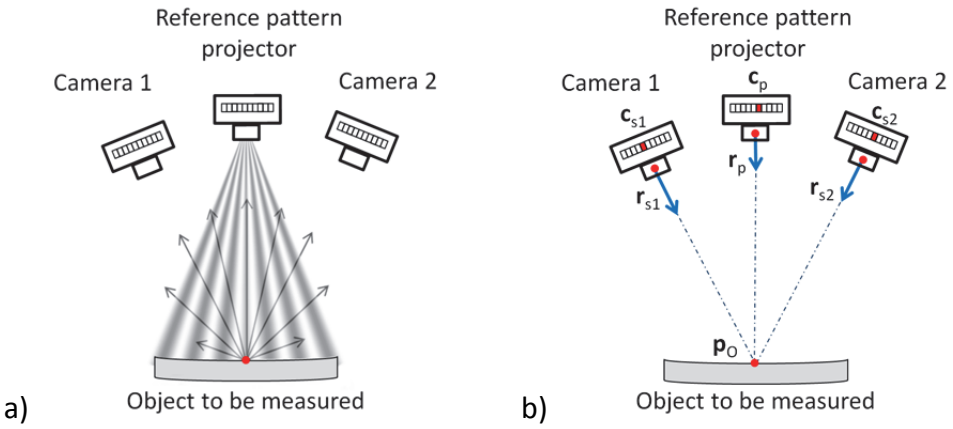

Figure 13: Principle of Fringe Projection (FP): a) In phase measurement, a sinusoidal pattern is projected on the measurement surface, light diffusely scattered by the surface (shown here: Lambertian surface) is recorded by the cameras. The object needs to be at least partly scattering in order to reach the cameras and make a phase measurement possible; b) After measurement and demodulation, subpixel positions of common phase are found in the phase images of both cameras, and the respective rays from the both cameras are intersected.

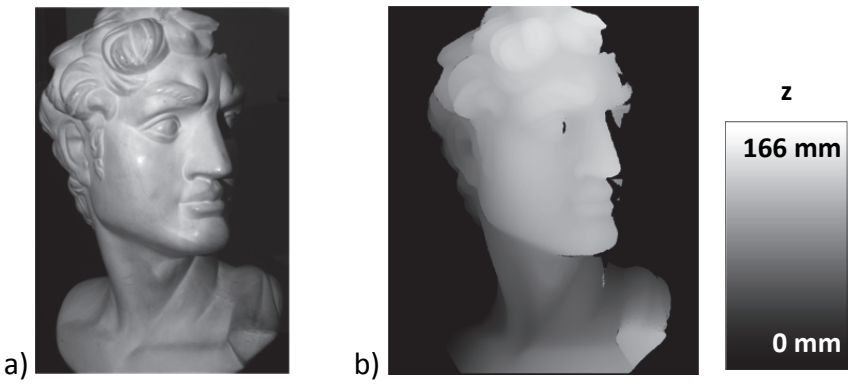

Figure 14: Shape measurement with the Fringe Projection (FP) technique: a) Photo of the measurement object, a scattering object with highlights; b) Shape measured with FP setup (Data from [San12]).

Although FP works best for the measurement of rough object surfaces, for the measurement of highly reflective surfaces the fringe modulation *M* and thus the shape measurement uncertainty can be improved by using projectors which emit radiation in the UV spectral band [Zwi11]. The reason is that using illumination sources with shorter wavelengths increases the ratio between surface roughness and wavelength and thus increases the fraction of scattered light [He91].

3 Comparison of GOP techniques

As described in the previous sections, PMD and FP are designed for the measurement of specularly reflective and scattering object surfaces, respectively. With the reflective behavior of a surface being dependent on its roughness, the fringe modulation *M* is related to the roughness of the object surface differently for FP and PMD techniques: Rougher surfaces induce higher values of *M* in FP measurements, and lower values of *M* in PMD measurements. The effect for PMD phase measurement has been shown by simulation in [Höf13] and experimentally in [Abh14] and [Kow12].

To compare the dependence of *M* on the surface roughness for FP and PMD, phase measurements of standard object *Rugotest 104*[2] (see Figure 15a) for surface-grinding induced roughness have been performed. The standard is divided into eight regions with specified one-dimensional roughness along one axis (indicated by arrow in the image), from R_a = 0.025 µm to R_a = 3.2 µm. Phase measurements were performed with the gradient of the sinusoidal reference pattern parallel to this axis, as depicted in Figure 15a. For each of the eight regions, the average value of *M* was calculated. The results of the measurement series are shown in the graphs in Figure 15b.

a)

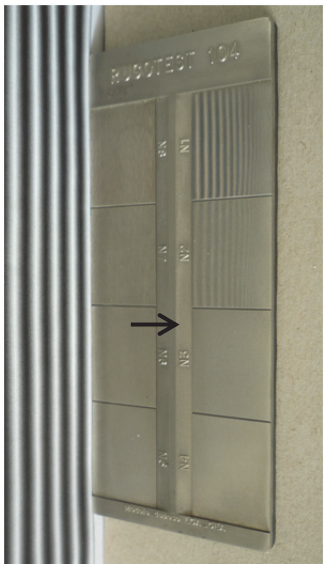

b)

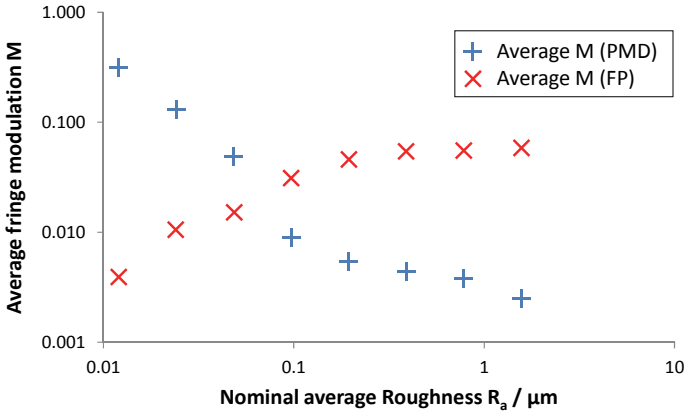

Figure 15: Dependence of fringe modulation M on surface roughness for PMD and FP measurements: a) Photo of the *Rugotest 104* roughness standard which has eight local patches of varying, specified one-dimensional roughness along the direction indicated by the black arrow. For the patches on the right side of the object, the surface roughness increases from top to bottom. As can be seen, for a sinusoidal pattern with gradient in the direction of the arrow, *M* drops for increasing roughness (lower patches); b) Phase measurements of the roughness normal with fringe gradient in the direction of the roughness were performed using PMD and FP (fringe period *P* for both measurements series: 200 pixels), and the average value of M in each of the patches was evaluated. The tendency of the graphs shows that for increased roughness R_a , *M* increases for FP and decreases for PMD.

[2] http://shop.vogel-germany.de/product_info.php?info=p5331_oberflaechen-vergleichsplatten--rugotest---planschleifen.html

The tendency of the graphs show that for increased roughness R_a , M increases for FP and decreases for PMD. As actual physical surfaces show both specular and scattering behavior to some degree, it is difficult to choose the GOP technique better suitable for surface measurement. This is particularly true for technical surfaces with comparable and angle-dependent contributions of both reflective behaviors. Technical surfaces, such as diamond-turned, rolled, die-cast, molded, sand-blasted, etched and spark-eroded metallic surfaces show mixed reflective and scattering behavior. The selection of the appropriate GOP technique for shape measurement of technical surfaces is not trivial and has to be decided on by performing test measurements with PMD and FP systems with varying parameters, such as the fringe period P of the sinusoidal reference pattern. As shown in [Bot08], with decreasing period P, the phase gradient and thus the sensitivity of the phase measurement generally increases. Detrimental effects are observed if materials with uncooperative properties (scattering surfaces for PMD, reflective surfaces for FP) are measured, where small P leads to a decreased fringe modulation M [Woi13]. The dependence of M on P for PMD and FP for a phase measurement with a semi-reflective flat metal plate is shown in Figure 16b.

a) 

b) 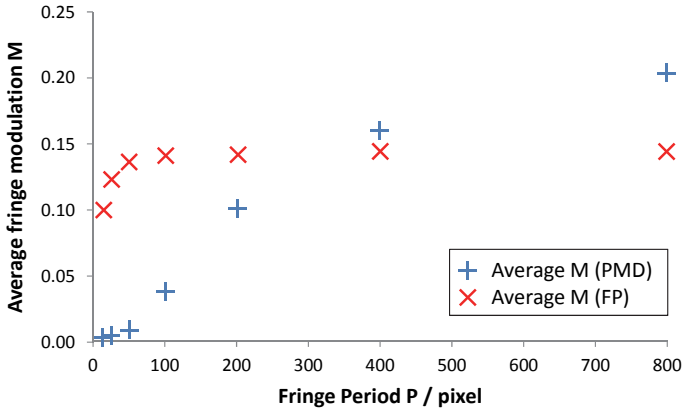

Figure 16: Dependence of fringe modulation *M* on the period *P* of the sinusoidal reference pattern for different GOPs: a) Photo of the measurement object, a semi-reflective flat Invar plate; b) The graph for *M*(*P*) for phase measurement on object in (a) with PMD and FP.

In literature, various estimates for the uncertainty and resolution of PMD shape measurements exist for perfectly specular surfaces. Estimations have been given phenomenologically [Bot04] and theoretically [Häu08] that the achievable resolution in the shape data retrieved from PMD measurements is in the order of 1 nm (for local surface angle: less than 10 arcsec [Seß04], for local curvature: less than 0.02 dpt [Kna04]). From the measurement of a flat high-precision mirror with a measurement field size of 47x50 mm², a global shape measurement uncertainty of 110 nm has been achieved [San11]. Although the PMD shape measurement uncertainty is higher for scattering surfaces [Höf13], it is expected to be still in the sub-µm range. The depth resolution of shape data from FP measurements can

be estimated following a rule of thumb from [Bot03]: Depending on the triangulation angle between the optical axes of camera and projector, a good estimate for the depth resolution is the measurement field width multiplied by 1/10000, giving approximately 4 µm for a field of 40x40 mm². Recently performed uncertainty estimates for a system of approximately this field of view have found an uncertainty between 1.7 and 3.1 µm [Jon15].

Table 2: Comparison of geometric-optical phase measurement (GOP) techniques, showing that FP and PMD are used for different but overlapping classes of object surfaces, and have different depth resolution and approaches to surface reconstruction. PMD measurements give a resolution of >10³ better than FP measurements, but need additional information for shape calculation.

GOP technique	Applicable surface types	Depth resolution for field size 40x40 mm²	Surface reconstruction
Phase Measuring Deflectometry (PMD)	Smooth, partially reflective	1 nm [Häu08]	Additional information needed (Regularization)
Fringe Projection (FP)	Rough, partially scattering	4 µm [Bot03]	Directly from phase measurement

4 Hypothesis

4.1 Problem description

As shown in section 3, due to their measurement principles, GOP techniques PMD and FP can be used for specular reflective or scattering object surfaces, respectively. Perfectly specular reflection, and scattering (as from an ideal Lambertian surface) however can usually not be observed for real objects. This is especially true for many technical surfaces, which show both specular and diffusely reflective reflective behavior [Sch96], in some cases also varied over different areas. For geometric measurement of real object surfaces, it is thus complicated or sometimes even impossible to select the GOP technique best suitable.

4.2 Proposed solution

Comparing PMD and FP (see Table 2) it becomes evident that although the techniques are designed for different object surface types, they can both be used for measuring object surfaces that show both scattering and specularly reflective behavior. While FP measurements directly deliver shape data, PMD measurements need extra information (such as an initial shape guess) for shape calculation, but have a superior measurement uncertainty. A combination of PMD and FP techniques could be employed for the measurement of this class of surfaces to benefit from the strengths of both techniques via fusion of the measurement data acquired with the individual sensors. As PMD measurements require additional information for calculating the object shape from measured data by *regularization* of the underlying mathematical problem (see section 2.2.2), a new regularization approach could be developed using the data generated from FP measurements as additional information. This would allow for the first time to perform measurements of unknown surfaces, and of unconnected surface regions, without the need for exact positioning in the measurement volume with a single-camera PMD system. An algorithmic implementation could be performed by modifying an existing shape integration algorithm, using the shape data measured with FP as the input shape data of the algorithm.

A combined measurement with both techniques and fusion of the data has been proposed in [Wer11]. For the measurement of free form surfaces, a combined PMD / FP setup has been presented in [Bre09], comprised of a projector and TFT monitor as reference pattern sources, and two cameras which are both used for FP and PMD measurement. Although in [Bre09] both measurements with the PMD and FP subsystems are performed, the data acquired with the PMD and FP subsystems are evaluated independently, with Stereo PMD regularization being used for the evaluation of the PMD phase measurements.

In summary, the combination of PMD and FP techniques using a combined setup and fusion of the data acquired from PMD and FP measurements can be regarded as a promising approach, and has not yet been investigated.

5 Set-up of a combined GOP system

As a first step for building up a combined GOP system, the geometry of the whole measurement system was developed. To enable PMD and FP measurement, such a system must contain a TFT monitor and projector as signal sources, one camera for PMD measurement, and one or two cameras for fringe projection. For the FP subsystem, a setup with two cameras was chosen, for which calibration of the reference pattern projector can be omitted. As the PMD and FP measurements were planned to be performed sequentially, in the setup only two cameras were needed out of which one of the cameras was to be used mutually for PMD and FP measurements. A principle drawing of the combined GOP system geometry is shown in Figure 18.

In order to save on hardware, a camera (*camera 2*) and an LCD reference pattern projector available in the lab were integrated into an existing PMD test setup, consisting of a TFT reference pattern monitor and a camera (*camera 1*). A photo of the combined GOP system developed is shown in Figure 18b. The projector called *MiniPro* is a device custom-built at BIAS for the fringe projection measurement on small to mid-size areas. Images with a lateral resolution of 1024x768 can be projected and the device is addressed with 12-Bit grayscale values . The maximum working distance (from projection-sided end of housing to projection plane, see Figure 17a) for a focused projection is 146 mm, with an illuminated field of 65 x 48 mm². The projector is equipped with a lens with focal length of 50 mm (non-focusable), set to an F-number of 8, combined with a focusing unit, see Figure 17b.

a) b)

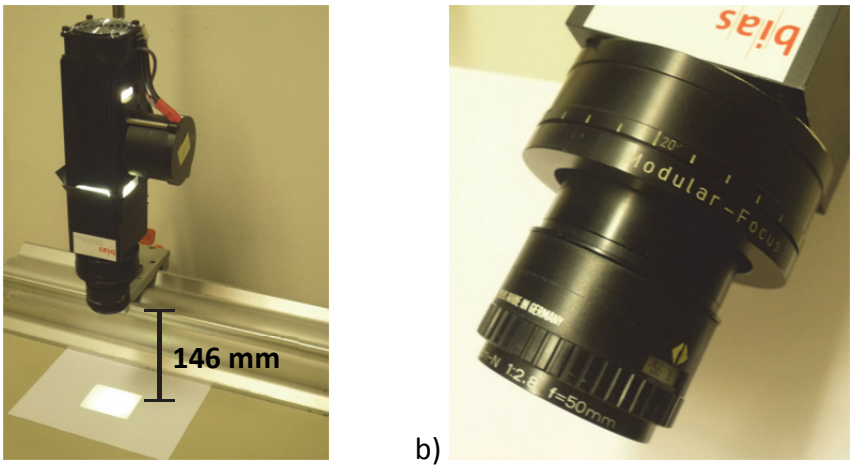

Figure 17: Projector MiniPro, custom-built at BIAS for usage in FP measurements with small to mid-sized measurement fields: a) Projector focused at maximal working distance of 146 mm, with an illuminated field of 65 x 48 mm²; b) Lens of the projector, assembled from Rodenstock Modular-Focus and Apo-Rodagon-N lens with focal length of 50 mm.

With the short maximum working distance of the projector, and in order to avoid shadowing the field of view of the cameras, the projector had to be placed on the side of the setup, illuminating the measurement object at a rather large angle between projector optical axis and normal of the reference object plane. This resulted in a tilted focal plane, which was not

critical due to the relative invariance of the sinusoidal reference patterns to defocussing, but could in future development be solved by adjusting the projector's LCD to satisfy the Scheimpflug condition [Ray02].

Camera 2 was integrated at the side of the setup, as a compromise between a position near camera 1 to avoid shadowing for object surfaces with steep slopes, and a position located farther from camera 1, in order to achieve a larger triangulation basis. For simplified processing with the measurement software *BIAS Fringe Processor 5.7* (see section 10.1) camera 2 was configured to symmetrically crop recorded images from 1936 x 1456 pixels to 1392 x 1040 pixels to have equal image size as camera 1. The aperture of the camera was set to an f-number of 4 (compare to f-number of 2.8 for camera 1) as a compromise between low image noise for short exposure durations (high photon flux), and a large depth of focus needed due to a tilt of the focal plane. As camera 1 was already focused to the object plane and calibrated, no changes to the lens aperture were made to avoid necessary re-calibration of the camera, see section 5.1.2. A list of hardware components used for the GOP setup is given in Table 3.

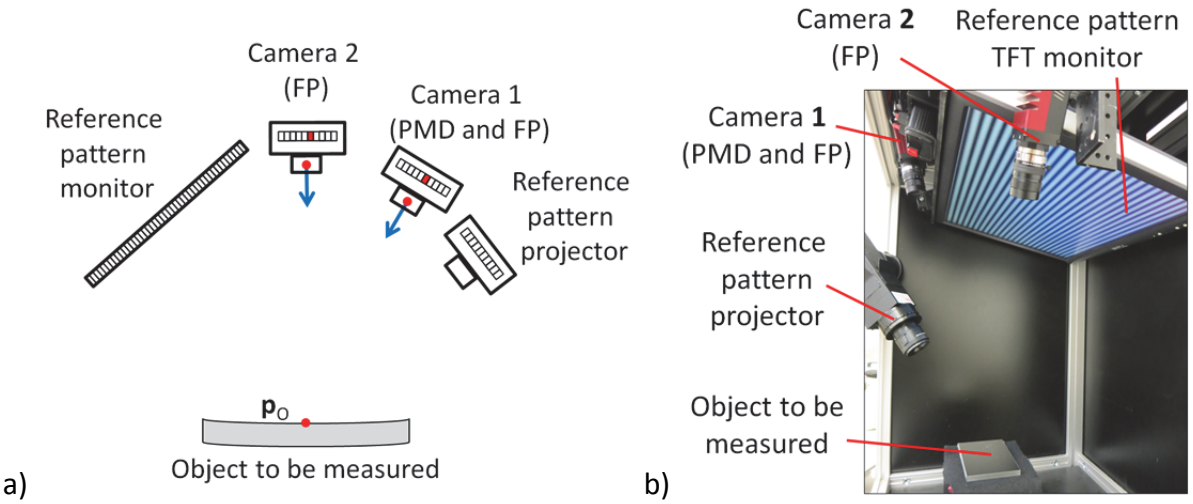

Figure 18: Experimental combined GOP measurement setup; a) Principle drawing of the setup with projector and a TFT display as signal sources, and a stereo camera system for FP measurements. Camera 1 is also used for PMD measurements; b) Photo of the test setup in the laboratory.

Table 3: Hardware components used in the developed combined GOP setup. As for the custom-built projector no data sheet was available, the pixel pitch was calculated from width and height of the LCD (uncertainty: 2 mm) and resolution.

Component	Product ID	Resolution / Pixels	Pixel pitch / µm	Lens focal length / mm	Lens f-number
Camera 1	AVT Marlin F146B + Pentax TV lens	1392 x 1040	4.54	25	2.8
Camera 2	AVT GT 1920 + Pentax TV lens	1392 x 1040, native: 1936 x 1456	4.65	25	4
TFT monitor	DELL 2001FP	1600 x 1200	255	-	-
LCD projector	VEW MiniPro + Apo-Rodagon-N lens + Rodenstock focusing unit	1024 x 768	26.7 ± 1.4	50	8

5.1 System calibration

5.1.1 Reference pattern source linearization

As consumer TFT monitors are designed for human viewing purposes and not for usage in measurement applications, the output irradiance is not linear to the input grayscale value. The response curve, which is dependent on the TFT type (IPS, TN…) [Fis10], can be measured and the inverted function can be used as a look-up table for the grayscale values sent to the monitor. For the sampling of the response curve, for every grayscale value (e.g. 0-255 for an 8 Bit display) an image consisting of uniform grayscale value is displayed on the TFT monitor, and the monitor surface is imaged with a camera. The response value for each input grayscale value is then retrieved by calculating the average value in the image of the TFT monitor surface. For the assembled system, the response curve of the reference pattern monitor shown in Figure 19a was measured with the camera in the setup. As the camera is not pointed at the monitor, a mirror was used to record the monitor surface with the camera. The look-up table generated from this response curve measurement was used for all subsequent measurements which involved the TFT monitor. A linearization was also performed for the projector in the HR setup. Here, the measurement was performed by illuminating a quasi-Lambertian surface (white paper) with the projector, and imaging the surface with the camera. In the response curve of the projector shown in Figure 19b a saturation of the projector response can be seen for input grayscale values $\gtrapprox 0.68 = g_{max}$ (i.e. grayscale value 2785 for the 12-Bit *MiniPro* projector). To avoid saturation, the grayscale value range used for the projector was scaled to $[0, g_{max}]$. Although a narrowed dynamic range of the signal source in general is disadvantageous regarding the signal-to-noise ratio, it is deemed to be beneficial for an accurate signal transfer in this case, because the discarded range has a response curve with a gradient of nearly zero.

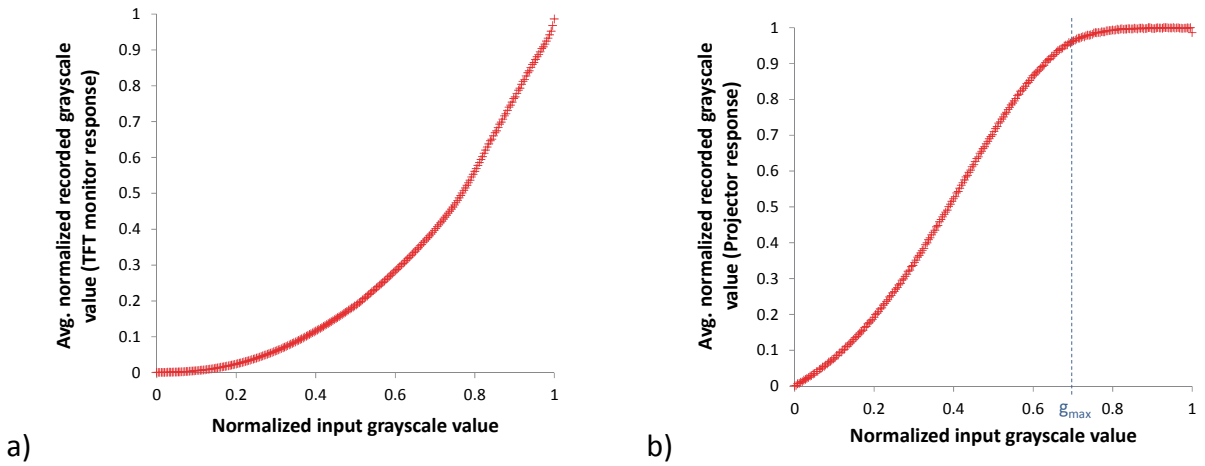

Figure 19: Non-linear illumination response curves of the reference pattern sources used in the combined GOP setup: a) Response curve of the TFT monitor; b) Response curve of the data projector, showing saturation at normalized input grayscale value $g_{max} \approx 0.68$. To avoid saturation, the grayscale value range used for measurement was scaled to $[0, g_{max}]$.

5.1.2 Camera calibration

Camera systems, comprising of a pixelated optical sensor and an imaging lens, have been used in a wide range of measurement applications for several decades, during which extensive investigations were performed concerning their relevant properties such as spectral sensitivity and geometric imaging behavior. This resulted in the development of efficient models for calibration [Luh10] and estimation of statistic deviations [Fis11, Fis12], with the description of noise properties of the camera being thoroughly described in the EMVA 1288 Standard [EMVA12]. As the cameras used in the combined GOP setup have industry-type grayscale CCD sensors, in the following it is assumed that the camera sensor has a uniform linear illumination sensitivity and amplification for all pixels, which reduces the calibration of the camera to the camera geometry calibration. In camera geometry calibration, the geometric imaging of the camera system including distortions by the lens is sampled, resulting in a mapping of each sensor pixel to a ray of sight in space. The standard geometric camera calibration approach described in [Zha00] is based on a pinhole camera model (see Figure 20a), i.e. all rays of sight of the camera originate at a single point in the entrance pupil of the camera, and are altered by radially symmetric distortion terms. Due to the finite entrance pupil diameter in real camera lenses, the pinhole model does not describe the imaging geometry appropriately. A different calibration approach, known as the *Vision Ray Calibration* (VRC) [Bot03, Bot10] allows different coordinates of origin in the entrance pupil for the individual rays of sight (see Figure 20b), and the correction of highly unsymmetrical, local distortions of the optical system. The VRC technique uses a black box, quasi model-free approach, with the main constraint being that each pixel is assigned a line of sight in the measurement volume, originating in the entrance pupil plane, see Figure 20b. The calibration output is a set of vectors describing the lines of sight for each pixel individually. As the VRC technique has the potential of delivering a highly accurate description of imaging optics [Bot10], it was used for the calibration of the camera in the combined GOP setup.

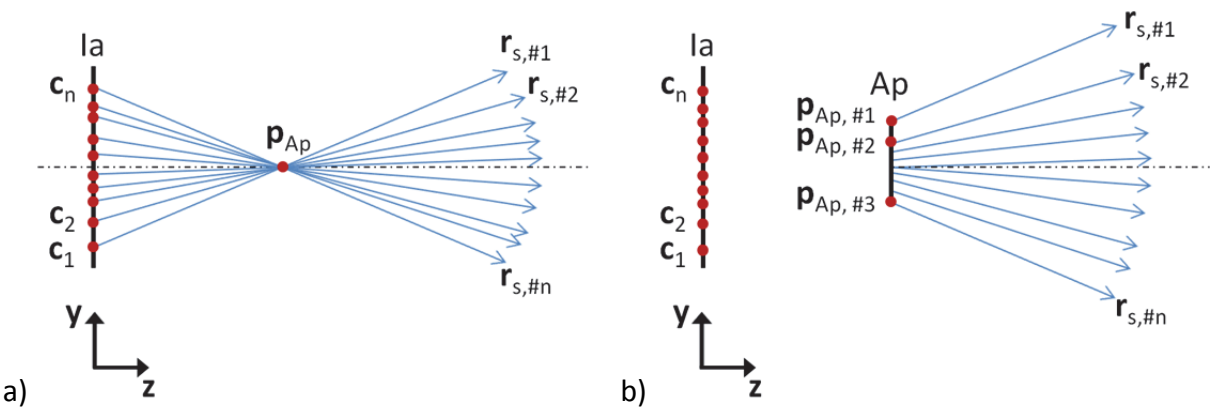

Figure 20: Methods for geometric camera calibration, resulting in mappings of rays of sight $r_{s,\#n}$ to sensor pixel positions c_n in the imaging plane *Ia*: a) Standard photogrammetric camera calibration [Zha00] is based on a pinhole model, i.e. all rays of sight $r_{s,\#n}$ are assumed to intersect at aperture point p_{Ap}. Additionally, the rays of sight can be corrected with radial-symmetric aberration terms; b) The model used in generic Vision Ray Calibration is limited to the rays of sight emerging from an aperture plane *Ap*, providing a better description of the imaging geometry than the standard method.

Camera 2 was calibrated using an implementation of the VRC in the Fringe Processor software. As the camera calibration becomes invalid when lens parameters such as focal distance or f-number are changed, camera 2 was integrated into the setup, and focal distance and f-number were set before performing the calibration.

In the calibration, the phase measurement was performed for 5 positions of the reference pattern TFT monitor. The pixelwise error *E* from calculation of the lines of sight is calculated as the RMS of distances Δr_n of the calculated penetration points in the monitor plane at position *n* to the calculated ray of sight, see Figure 21. For the calibration of camera 1 and camera 2, the pixelwise error is shown in Figure 22a and Figure 22b. The average of the pixelwise error from calculation of the lines of sight (5.02 µm for camera 1, 6.42 µm for camera 2) is acceptable, as it is far less than the lateral resolution in the object plane (78 µm for camera 1, 114 µm for camera 2).

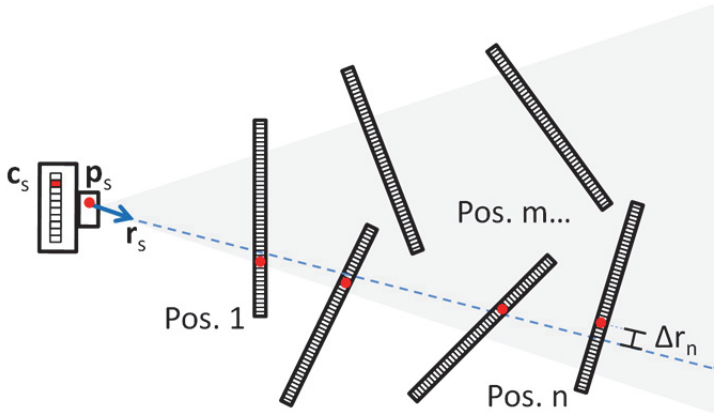

Figure 21: Camera calibration using the Vision Ray Calibration (VRC) approach: In the calibration procedure, phase measurements are performed with a TFT monitor used as reference source being put in different positions shown here exemplary, in the cone of sight (shown in gray) of the camera. From evaluation of the phase measurements, for each camera pixel coordinates in space are retrieved at the different monitor positions, from which a ray of sight can be calculated. The ray of sight is described as a base point in the camera's entrance pupil, and a directional vector (from: [Reh13], modified).

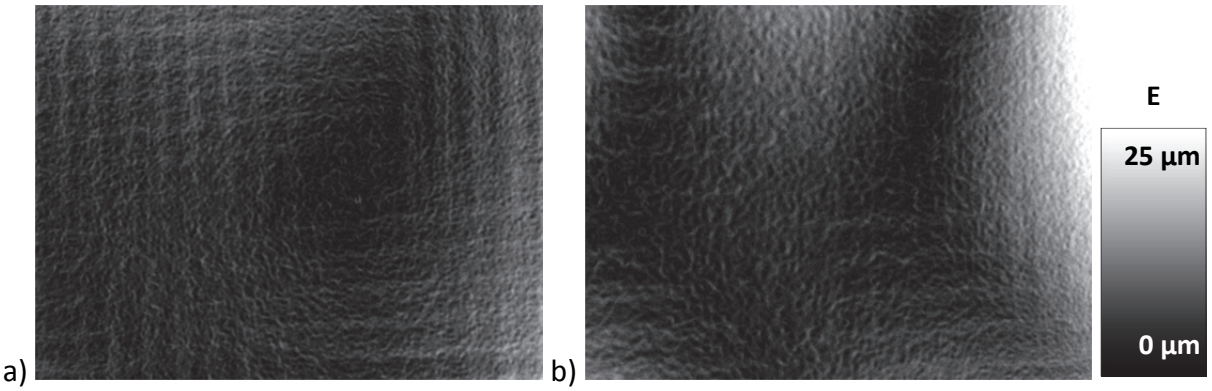

Figure 22: Camera calibration error (pixelwise lateral RMS distance of the calculated penetration points in the monitor plane to the calculated ray of sight): a) Error from camera 1 calibration (average: 5.02 µm); b) Error from camera 2 calibration (average: 6.42 µm).

5.1.3 System geometry calibration

After calibration of signal sources (TFT monitor and projector) and sinks (cameras) in the assembled GOP system, described in the previous sections, the system geometry calibration is performed in which the relative positioning of these components is computed. Geometry calibration was performed separately for the PMD subsystem (Reference pattern display and camera 1) and FP subsystem (Reference pattern projector, camera 1 and camera 2) of the GOP system using calibration algorithms implemented in the Fringe Processor software.

5.1.4 PMD subsystem geometry calibration

In the geometry calibration of the PMD subsystem, the relative orientation of the reference pattern TFT display and camera 1 is established. Additionally, a reference coordinate system in the measurement volume is defined, which is used as output coordinate system for shape data from PMD measurement. The measurements needed for this calibration can be performed directly by geometric-optical phase measurement, using the reference pattern TFT display and camera 1 as assembled and positioned in the GOP setup. For the measurement, a high-precision mirror (λ/10 planarity deviation) with metallic surface is placed in the measurement volume so that its surface includes the reference point $\boldsymbol{p}_{Ref}$ in the measurement volume. The reference point is visually marked by the intersection between the rays of two low-power laser pointers which are mounted in the setup, see Figure 23a.

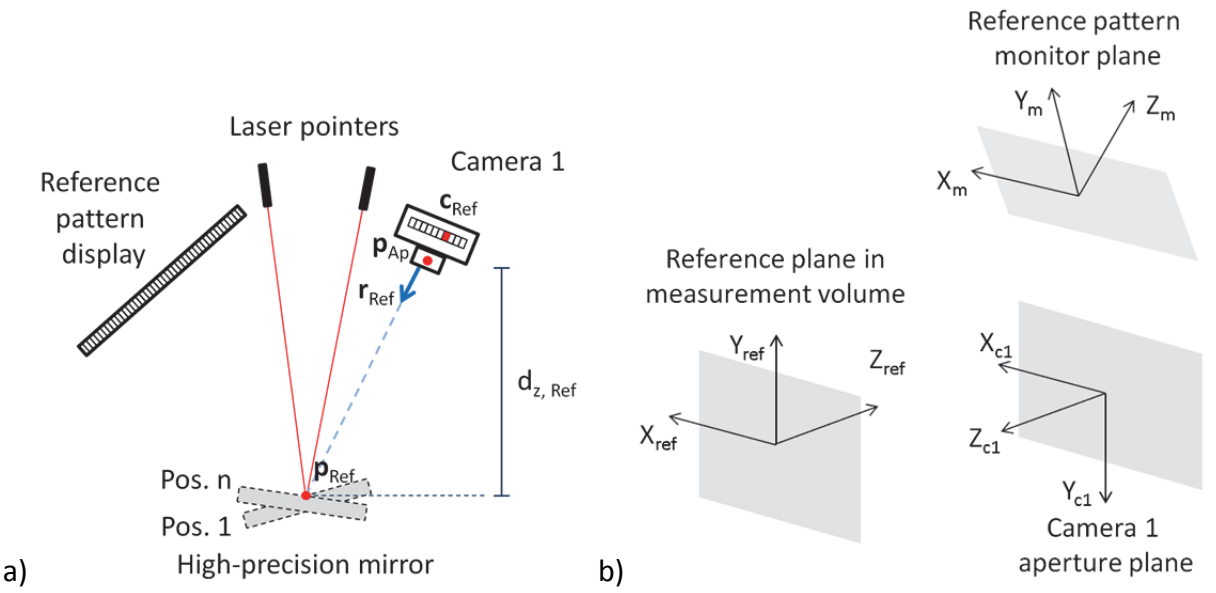

Figure 23: Geometry calibration of the PMD-subsystem: a) For the geometry calibration, geometric-optical phase measurements are performed for a flat mirror with λ/10 planarity deviation which is manually placed in the measurement field so that its surface intersects with the reference point p_{Ref} visually marked by the intersection of two laser pointers. Between measurements, the mirror is tilted at a different angle and repositioned to intersect with p_{Ref}. With the surface intersecting with p_{Ref} for every measurement, the relative geometrical orientation between the reference pattern display and camera 1 can be calculated. Additionally, the distance $d_{z,Ref}$ between center of the camera lens aperture p_{Ap} and p_{Ref} (along the z-axis of the reference plane) is retrieved for the point in space viewed by the ray of sight r_{Ref} (not necessarily originating at p_{Ap}, see section 5.1.2), and imaged to sensor pixel c_{Ref}; b) Coordinate system definition for camera, reference pattern monitor, and reference plane in measurement volume.

With the object positioned correctly, a phase measurement is performed. After an initial untilted positioning of the object, sequentially the measurement object is tilted arbitrarily and repositioned to intersect with $\boldsymbol{p}_{Ref}$, and additional phase measurements are performed. For the geometry calibration of the PMD subsystem, three phase measurements were performed and evaluated with the Fringe Processor software. The initial untilted mirror position is then used for definition of the ($\boldsymbol{X}_{Ref}$, $\boldsymbol{Y}_{Ref}$) - plane of the reference plane coordinate system.

As an output of the calibration, the relative orientation of the coordinate systems of the reference pattern display $V_m(\boldsymbol{X}_m, \boldsymbol{Y}_m, \boldsymbol{Z}_m)$ from the coordinate system of camera 1, $V_{c1}(\boldsymbol{X}_{c1}, \boldsymbol{Y}_{c1}, \boldsymbol{Z}_{c1})$, and of the coordinate systems of the reference plane $V_{Ref}(\boldsymbol{X}_{Ref}, \boldsymbol{Y}_{Ref}, \boldsymbol{Z}_{Ref})$ in the measurement volume from the coordinate system of camera 1 (see Figure 23b) are retrieved as a translation vectors $\boldsymbol{T}(T_x, T_y, T_z)$ and Eulerian angles rotation vectors $\boldsymbol{R}(R_x, R_y, R_z)$. The center of the camera coordinate system is defined as the central subpixel position. Additionally the distance d_{Ref} between the center of the camera lens aperture $\boldsymbol{p}_{Ap}$ and $\boldsymbol{p}_{Ref}$ is calculated in the calibration measurement. For the ray of sight $\boldsymbol{r}_{Ref}$ (not necessarily originating at $\boldsymbol{p}_{Ap}$, see section 5.1.2) mapped to sensor pixel $\boldsymbol{c}_{Ref}$, the distance to the object can then be calculated. For measurements later performed with the calibrated setup, objects can be positioned at $\boldsymbol{p}_{Ref}$ using the intersecting rays from the laser pointers, and the measurement can be evaluated using RDR with an estimated object distance of $d_z = d_{z,Ref}$. The results from the geometry calibration, given in Table 4 and Table 5, agree with rough measurements performed with a tape measure, the retrieved rotations around the x axis agree with the physical orientation of the coordinate systems, see Figure 23b.

Table 4: Results from geometry calibration of PMD subsystem with reference subpixel position c_{Ref} (c_x, c_y) on sensor, distance d_{Ref} between camera pupil center and reference point p_{Ref} in measurement volume, and translation vector T (T_x, T_y, T_z) and rotation vector R (R_x, R_y, R_z) for the transformation of coordinates in camera 1 coordinate system to coordinates in monitor coordinate system. The calibration was performed using the Fringe Processor software.

c_{Ref} (c_x, c_y)/ Pixel	d_{Ref} / mm	T^T / mm	R^T / rad
(689.97, 539.82)	444.952	(-4.252, -194.192, 80.179)	(2.658, -0.028, -0.010)

Table 5: Translation vector T (T_x, T_y, T_z) and rotation vector R (R_x, R_y, R_z) for the transformation of coordinates in camera 1 coordinate system to reference plane coordinate system, from geometry calibration of PMD subsystem.

T^T / mm	R^T / rad
(1.337, -110.884, 430.409)	(2.903, -0.004, 0.001)

With the calibrated PMD subsystem, test measurements were performed using a flat mirror (λ/4 planarity) as measurement object. The measured phase data were evaluated separately using ISR with plane shape model, and using RDR with an input $d_z = d_{z,Ref}$. On the calculated shape data patch (lateral size 64x56 mm²), tilt was removed using a numerical best fit plane. The shape data with tilt removed are shown in Figure 24, and the statistics for the fit

residuals are in shown in Table 6. The results from ISR-based evaluation (shape residuals have peak-to-valley dynamic of 293 nm, standard deviation of 45 nm) shows that the PMD calibration was successful.

Table 6: Results from test measurement of a plane mirror (λ/4 planarity) with calibrated PMD subsystem. The shape data were calculated separately using ISR (with plane shape model), and RDR (with input $d_z = d_{z,Ref}$) regularization, respectively. On the calculated shape data, a numerical fit with plane shape model was performed, for which the statistics are shown here. As a result of the calculation using ISR, the value Δd_z for d_z output by the ISR algorithm is given. The specified uncertainty was calculated as the standard deviation of three repeated measurements, to be interpreted as the measurement repeatability.

Regularization method	Shape residuals peak-to-valley / µm	Shape residuals standard deviation / µm	Output Δd_z / mm
ISR (plane model)	0.293 ± 0.001	0.045 ± 0.001	0.641 ± 0.001
RDR ($d_z = d_{z,Ref}$)	3.040 ± 0.005	0.620 ± 0.001	n. a.

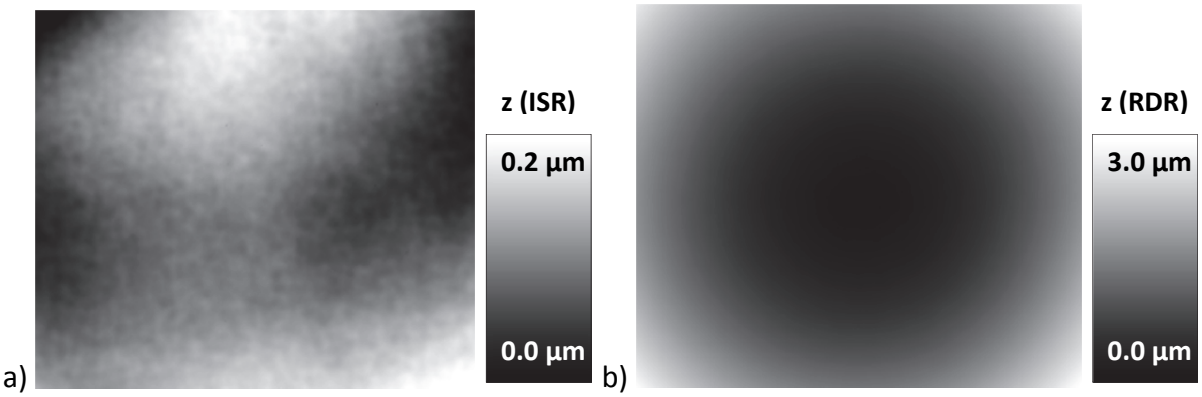

Figure 24: Residuals of tilt-corrected shape data from measurement of flat mirror (λ/4 planarity) with calibrated PMD setup (measurement field size: 64x56 mm²). Data from calculation using: a) ISR with plane shape model, b) RDR (using input $d_z = d_{z,Ref}$).

With the difference Δd_z between the input value used for d_z in the RDR-based shape calculation and the output value for d_z given by the ISR algorithm (see Table 6), the reference point distance $d_{z,Ref}$ (calculated from d_{Ref} from PMD system geometry calibration), and the half diagonal of the measurement field x_{field}, the expected depth error Δz expected as output from RDR-based shape calculation is calculated using equation (9) as:

$$\Delta z \approx \frac{\Delta d_z \cdot {x_{field}}^2}{2 \cdot {d_{z,Ref}}^2} = \frac{0.641\ mm \cdot (42.52\ mm)^2}{2 \cdot (432.347\ mm)^2} = 3.10\ \mu m\,. \qquad (10)$$

The calculated value for $\Delta z \approx 3.1$ µm is in good accordance with the residuals of the tilt-corrected shape data from RDR-based calculation with of Δz (peak-to-valley) = 3.040 µm and Δz (standard deviation) = 0.620 µm, see Table 6. This again indicates that the PMD system geometry calibration was successful.

5.1.5 FP subsystem geometry calibration

The FP subsystem consists of a reference pattern projector and two cameras. As two cameras are available, shape measurement (and geometry calibration) solely require performing phase measurements with both cameras and finding pixels of common phase in the respective recorded phase images, see section 2.2.3. This eliminated not only the need for projector calibration, but also for determining the projector's position, reducing the geometry calibration to a measurement of the orientation between camera 1 and camera 2.

The FP subsystem calibration was performed after the PMD subsystem calibration, with the components positioned inside the GOP system. For the FP subsystem calibration, two measurement series were performed. As shown in Figure 25a, the first series consisted of measurements of a scattering plane object with the projector as reference pattern source. Between measurements, the plane was repositioned arbitrarily in the measurement volume (in contrast to PMD system geometry calibration) without the need for alignment with a reference point. The second series was performed without using the projector and consisted of placing a TFT monitor in the measurement volume, which itself acted as reference pattern source. As a result of the calibration calculation, the relative orientation of the coordinate systems of camera 2 $V_{c2}(\boldsymbol{X}_{c2}, \boldsymbol{Y}_{c2}, \boldsymbol{Z}_{c2})$ from the coordinate system of camera 1 $V_{c1}(\boldsymbol{X}_{c1}, \boldsymbol{Y}_{c1}, \boldsymbol{Z}_{c1})$ (see Figure 25) were retrieved as a translation vector $\boldsymbol{T}$ and rotation vector $\boldsymbol{R}$, see Table 7. The retrieved translations again agree with rough measurements performed using a tape measure; and the retrieved rotation angle of approximately π around the z-axis (optical axis of the camera) agrees with the rotation of the field of view of both cameras, see Figure 25b.

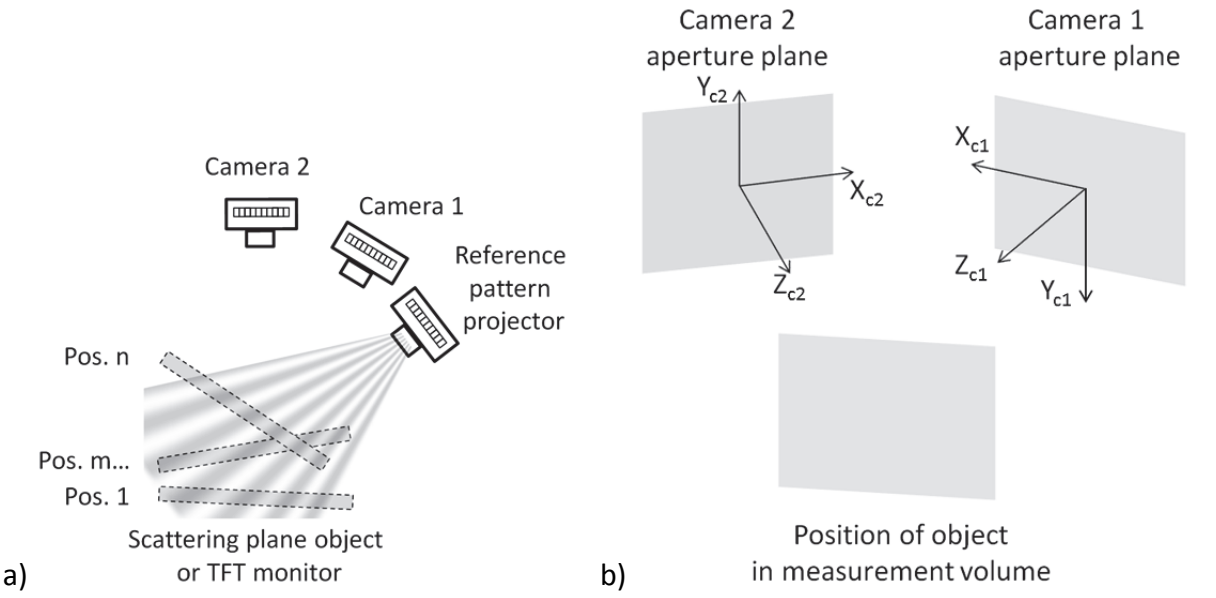

Figure 25: Geometry calibration of the FP subsystem: a) For the FP subsystem, only the orientation between camera 1 and camera 2 needs to be calibrated. This is done by performing phase measurements with both cameras using either i) projector as reference pattern source and a scattering, plane surface as object or ii) a TFT monitor reference pattern source and object at the same time. Between measurements, the objects are repositioned arbitrarily in the measurement volume b) Coordinate system definition for camera 1 and camera 2, camera 2 is mounted upside down, so that the main rotation component is around the z-axis.

Table 7: Results from geometry calibration of FP subsystem with translation vector T (T_x, T_y, T_z) and rotation vector R (R_x, R_y, R_z) for the transformation of coordinates in camera 1 coordinate system to coordinates in camera 2 coordinate system. The calibration was performed using the Fringe Processor software.

T^T / mm	R^T / rad
(223.747, -98.445, 99.473)	(0.277, 0.523, -3.018)

To verify the performed FP system geometry calibration, measurements of a normal object with spheres of different radii (see Figure 26) were performed with the FP subsystem and, as a reference, with a coordinate measurement machine (*CMM*, Mitutoyo Crysta-Apex C, model 7106). On the measured shape data, numerical shape fits were performed using a spherical model without radius constraint. As shown in Table 8, the best-fit radii from FP and CMM measurements show maximum deviations of 45 µm.

Table 8: Results of test measurements of sphere normal object with calibrated FP system with best-radii $r_{fit,CMM}$ and $r_{fit,FP}$ from reference measurements with coordinate measuring machine and FP system, respectively. The uncertainty specified for FP was calculated as the standard deviation of three repeated measurements.

	Sphere #1	Sphere #2	Sphere #3
Best-fit radius $r_{fit,CMM}$ from CMM shape data / mm	25.0523 ± 0.0017	31.8073 ± 0.0017	37.5981 ± 0.0017
Best-fit radius $r_{fit,FP}$ from FP shape data / mm	25.0176 ± 0.0004	31.8190 ± 0.0007	37.5962 ± 0.0003

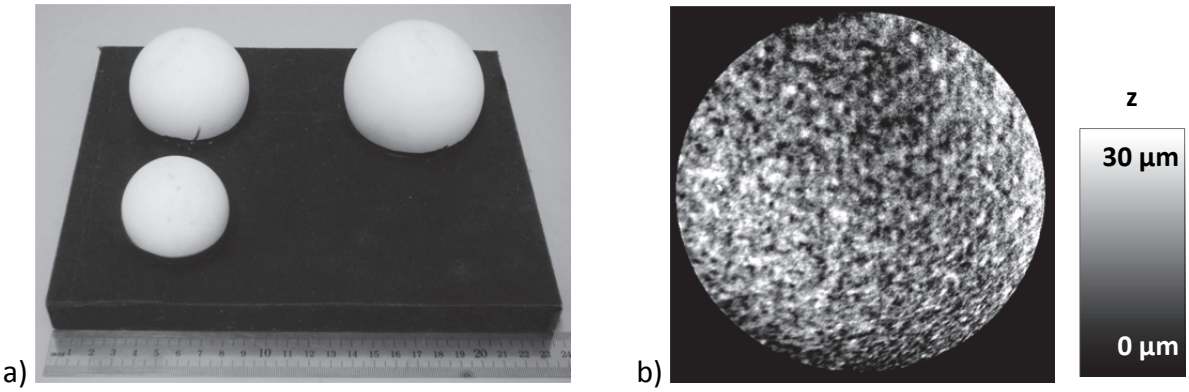

Figure 26: Measurement of reference sphere normal with the calibrated FP subsystem: a) Photo of reference sphere normal with scale. The object consists of three bearing balls, sprayed with permanent white paint for making the surfaces scattering; b) Circular masked region (lateral diameter: 47 mm) in shape residuals from numerical sphere fit (R=25.0523mm) of shape data for the smallest sphere from FP measurement.

6 Hybrid Reflectometry regularization (HRR)

6.1 Main shape calculation algorithm

The algorithm for performing shape calculation based on Hybrid Reflectometry regularization (HRR), is based on the RDR algorithm, modified to use input shape data from FP measurement. The HRR-algorithm is shown in Figure 27, explained in detail in the following, and in short at the end of this section. Two coordinate systems are used: A three-dimensional coordinate system (***x***,***y***,***z***) = $V_{Ref}(\boldsymbol{X}_{Ref}, \boldsymbol{Y}_{Ref}, \boldsymbol{Z}_{Ref})$) in continuous space, describing a point in the reference plane coordinate system. The other one is the coordinate system (c_x, c_y) in discrete space, describing a pixel position on the sensor of camera 1.

Input parameters of the algorithm are the two-dimensional phase data $\boldsymbol{\varphi}_{PMD}(c_x, c_y)$ from PMD measurement (mapping sensor coordinates to pattern coordinates, see section 2.2.1), and the z component $z_{FP}(c_x, c_y)$ of the shape data from FP measurement. The data processing is described in the following:

- An image $z(c_x, c_y)$ is initialized with $z(c_x, c_y) := z_{FP}(c_x, c_y)$ and the main *Integration Loop* is entered. This loop is iterated a defined number of times, a good working setting is six iterations.
- From the input image $z(c_x, c_y)$ and the rays of sight $\boldsymbol{r}_s(c_x, c_y)$ from camera calibration, *x* and *y* components for each pixel are calculated, which gives a point cloud with elements $\boldsymbol{p}_O(c_x, c_y)$ in space, with a point $\boldsymbol{p}_O(x, y, z)$ in the measurement volume mapped to every sensor pixel.
- Using equations (8), from every element $\boldsymbol{p}_O(c_x, c_y)$ of the point cloud and the respective monitor position $\boldsymbol{p}_M(c_x, c_y)$ on the monitor (known from $\boldsymbol{\varphi}_M(c_x, c_y)$), the respective ray of sight $\boldsymbol{r}_p(c_x, c_y)$ to the monitor is calculated, and from $\boldsymbol{r}_p(c_x, c_y)$ and $\boldsymbol{r}_s(c_x, c_y)$, the surface normal $\boldsymbol{n}(c_x, c_y)$ is calculated (see Figure 8)
- From the normals $\boldsymbol{n}(c_x, c_y)$ and the point cloud $\boldsymbol{p}_O(c_x, c_y)$, gradients $\boldsymbol{g}(c_x, c_y)$ are calculated.
- The gradients $\boldsymbol{g}(c_x, c_y)$ are integrated using the Fourier transform approach described in [Fra88], invalid pixels are interpolated from surrounding valid pixels. The result is a new scalar shape image $z(c_x, c_y)$.
- As the shape data are retrieved via integration of gradient data, the average height $\bar{z}_{FP}$ of the input shape image $z_{FP}(c_x, c_y)$ is added as an offset: $z(c_x, c_y) := z(c_x, c_y) + \bar{z}_{FP}$.
- Same as in the beginning of the loop, from the scalar image $z(c_x, c_y)$ and the rays of sight again a point cloud $\boldsymbol{p}_O(c_x, c_y)$ is calculated.
- Finally, another iteration of the loop is started or, if the maximum iteration count has been reached, the point cloud $\boldsymbol{p}_O(c_x, c_y)$ is output as $(x_{PMD}, y_{PMD}, z_{PMD})$.

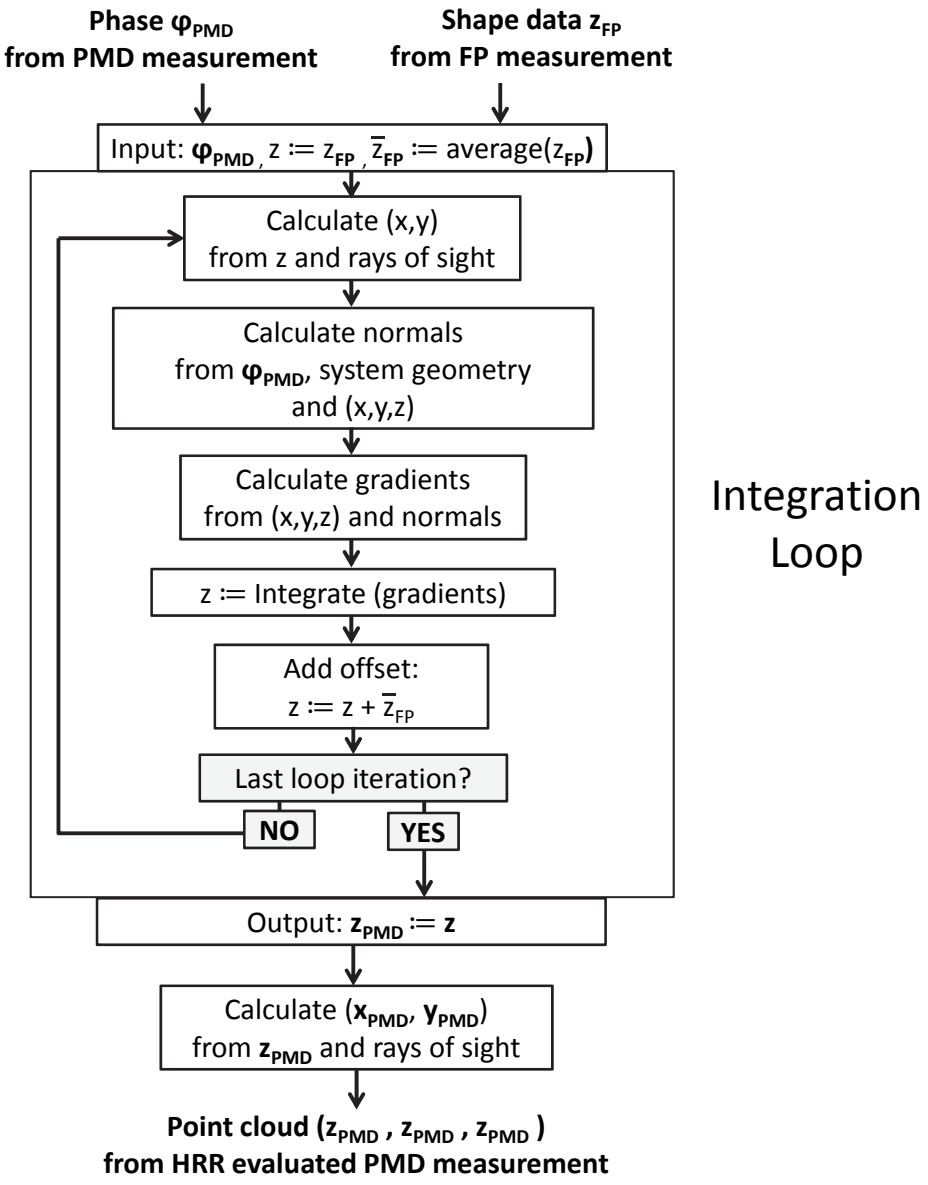

Figure 27: Algorithmic implementation of HRR-based shape calculation from phase data φ_{PMD} from PMD measurement and shape data z_{FP} from FP measurement. The integration is repeatedly performed in the integration loop, for a fixed number of iterations.

In short, the mode of operation can be described as follows: The input shape data z_{FP} are used for an initial, coarse calculation of surface normals and gradients. The shape retrieved by integration of the gradients lacks the offset of the original shape image, so that the average of the original input shape data z_{FP} is added. After one iteration, locally improved output shape z_{PMD} (using the measured PMD phase data φ_{PMD}) with corrected global offset (from FP shape data z_{FP}) is retrieved, so that the normal calculation in the next iteration will be more accurate. For all PMD measurements presented in this thesis, an iteration count of 6 was used for the integration loop.

The HRR-algorithm was implemented in the *FringeReflectionHybrid* tool in FringeProcessor version 5.7, see section 10.1.1.

6.2 Preparation of FP shape data

Shape data retrieved from FP measurement and evaluation are in the coordinate system of camera 1, while shape data used in the HRR algorithm and also retrieved from PMD measurement using ISR and RDR are in the reference plane coordinate system. Thus, prior to usage in the described algorithm, a coordinate transform from camera 1 coordinate system to reference plane coordinate system is performed for the data from FP, using the coordinate transform parameters given in Table 5.

7 Measurements with the combined GOP system

With the developed combined GOP system test measurements were performed. Object surfaces with hybrid scattering and specularly reflective behavior were measured and the shape was calculated using HRR. Additionally, to show the potential for using the combined GOP setup for the measurement of surfaces with arbitrary reflective behavior, surfaces with different, but globally constant reflective behavior, and surfaces consisting of unconnected regions with locally varying reflective behavior were measured. Prior to each measurement series, the fringe periods *P* for FP and PMD phase measurement were manually adapted for best signal quality. When performing FP measurements on partly reflective surfaces, the environment was darkened to avoid loss of contrast from stray light scattered on the surface and reflected by the specular regions. In the combined PMD setup, the inner walls are cladded with absorbing black velvet in order to avoid multiple reflections of the projector light. For the FP measurement of highly reflective objects, the reference pattern TFT monitor was completely switched off in order to avoid distortions of the measured phase due to reflection of the remaining illumination from the monitor.

7.1 Description of evaluation standards

7.1.1 Representation of shape data

In the evaluations presented in this section, all shape data are represented in the reference plane coordinate system shown in Figure 23b. The z coordinate is represented as grayscale value or color, with the color coding chosen for best data visibility. For measurement shape data valid at each pixel position (as in section 7.2), the data originally output with a slight perspective distortion from the camera are resampled to constant lateral resolution (see Figure 28a), the coordinate system is omitted in the following. Data with invalid pixels (as in section 7.23) are not resampled since resampling of the data validity mask is not sensible. The z coordinate is always coded in color, invalid pixels are shown in black (see Figure 28b).

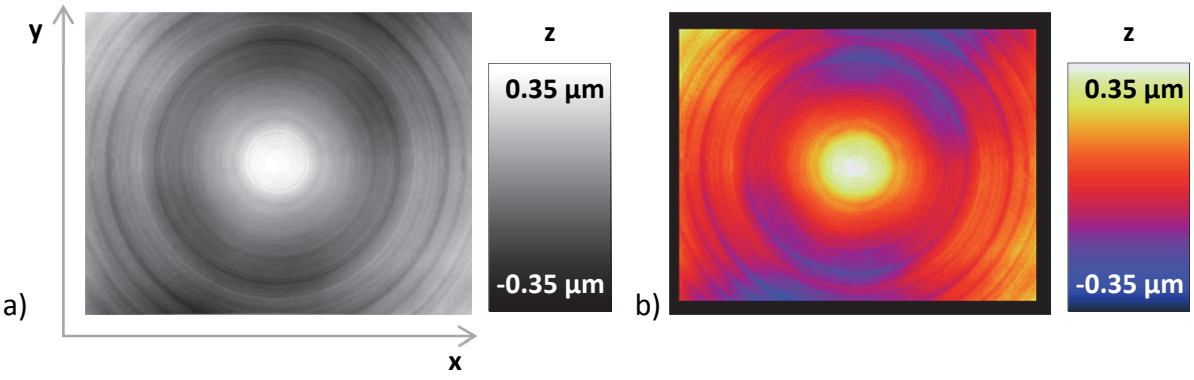

Figure 28: Representation of shape data: a) Shape data resampled to constant lateral resolution (coordinate system omitted in the following), b) Shape data with invalid pixels: not resampled, invalid pixels are shown in black.

7.1.2 Employed method for measurement repeatability estimation

For each measurement configuration, FP and PMD phase measurement including evaluation was performed three times in order to retrieve an estimation of the repeatability of the measurement. For each triples (x_1, x_2, x_3) of scalar values, the standard deviation σ [Bro01] is employed as an estimator for the repeatability:

$$\sigma = \sqrt{\frac{\sum_1^n (x_n - \bar{x})^2}{n-1}} = \sqrt{\frac{(x_1 - \bar{x})^2 + (x_2 - \bar{x})^2 + (x_3 - \bar{x})^2}{2}} \quad (11)$$

$$, with \quad \bar{x} = \frac{\sum_1^n x_n}{n} \quad ; \quad n = 3 \, .$$

The calculation of σ can also be applied to triples of shape images z in order to get a spatially resolved estimation of the repeatability. Using the input images z_1, z_2 and z_3, the resulting image $\sigma z(c_x, c_y)$ at each pixel position (c_x, c_y) is calculated as the standard deviation of the values $(z_1(c_x, c_y)$, $z_2(c_x, c_y)$, $z_3(c_x, c_y))$ in the three input images.

The pixelwise standard deviation image σz_p shows statistic as well as systematic deviations in the input images, an interpretation of the resulting images σz_p using exemplary input test images is shown in Figure 29. For the input images in Figure 29 a showing dominant noise, the output σz_p image (Figure 29 b) shows a high dynamic range. Images with low noise, but offset or slight tilt in reference to each other (Figure 29 c) result in output σz_p with a low dynamic range (Figure 29 d) and standard deviation $\sigma\,(\sigma z_p)$ of σz_p, with the average value of $Avg\,(\sigma z_p)$ being a measure of the deviation of the mean value in the input images.

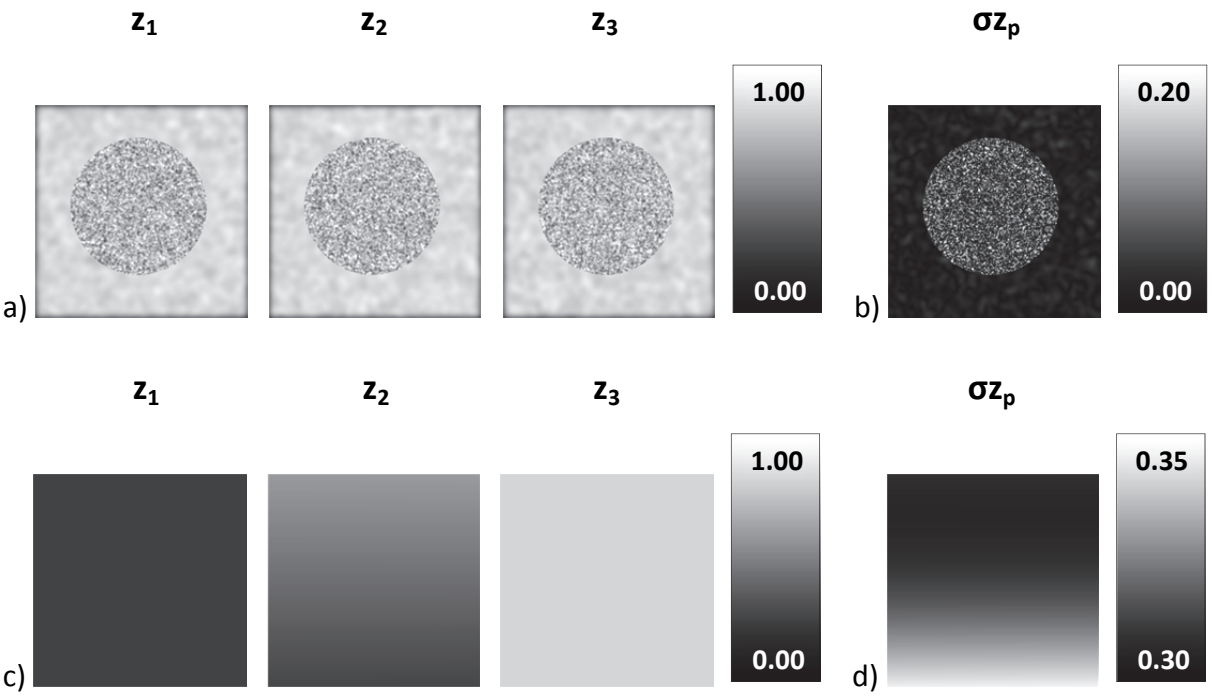

Figure 29: Calculation of pixelwise standard deviation image $\sigma z(c_x, c_y)$ from input images z_1, z_2, z_3 using artificial test images. Noise in input images (a) results in high dynamic in the output σz image (b). If input images have low noise, but offset or slight tilt in reference to each other (c), the output σz image (d) has a low dynamic, as can be seen when comparing compare scales for (b) and (d).

7.2 Technical surfaces with hybrid reflective properties

In this subsection, measurements of object surfaces with hybrid, i.e. specularly reflective and scattering behavior are presented, using FP and PMD with HRR, ISR and RDR evaluation. As test specimen, a flat metallic plate of unknown shape and a diamond-turned sphere with known nominal radius (given by the manufacturer) were used.

7.2.1 Flat metal plate

The flat metal (Invar) plate shown in Figure 16 in section 3 is a typical example of a technical surface with hybrid reflective behavior. In order to test the performance of the regularization algorithms for coarse object positioning, the plate was first positioned manually using the positioning laser pointers, and then displaced by z = -10.00 mm ± 0.01 mm in the reference coordinate system using a sliding caliper (Mitutoyo Digimatic). FP and PMD measurements were performed one after the other, and the shape data retrieved from FP were used for HRR-based evaluation of the PMD measurement. The phase measurements were performed using fringe periods of 12 pixels for FP, and 240 pixels for PMD measurement.

As shown in Figure 30, the modulation *M* for FP and PMD measurement are similar regarding the dynamic, but have individual lateral distributions of *M*. For the FP measurement, *M* shows dependence on the metallic surface structure, whereas for the PMD measurement *M* shows tarnished streaks on the surface which were not removable. Additionally, shape was calculated using ISR evaluation with a plane shape model, and RDR evaluation with input $d_z = d_{z,Ref}$, so that the estimation error Δd_z for the input d_z is -10.00 mm ± 0.01 mm. The shape data from FP and PMD shape calculations, with tilt removed, are shown in Figure 31, filtered FP data (Gaussian kernel, 20x20 pixels) and difference images to PMD shape data are shown in Figure 32. As can be seen, the PMD shape data are smoother than the FP shape data, which is partly due to less noise in the PMD data, but might also be resulting from the numerical integration.

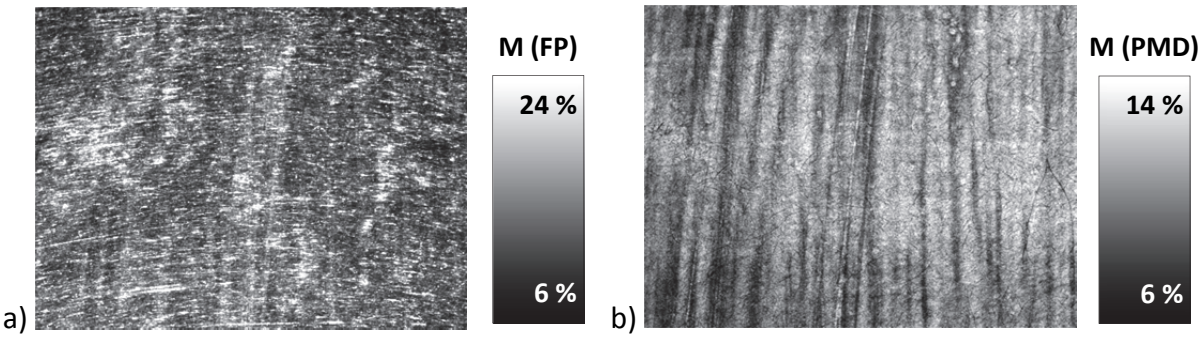

Figure 30: Fringe modulation *M* averaged from phase measurement in horizontal and vertical direction for measurement of flat plate object, lateral size of evaluated field: 38 x 28 mm²: a) *M* from FP phase measurement (fringe period: 12 pixels), showing dependence on the metallic surface structure; b) *M* from PMD phase measurement (fringe period: 240 pixels) revealing tarnished streaks on the surface which were not removable, and dark lines indicating scratches.

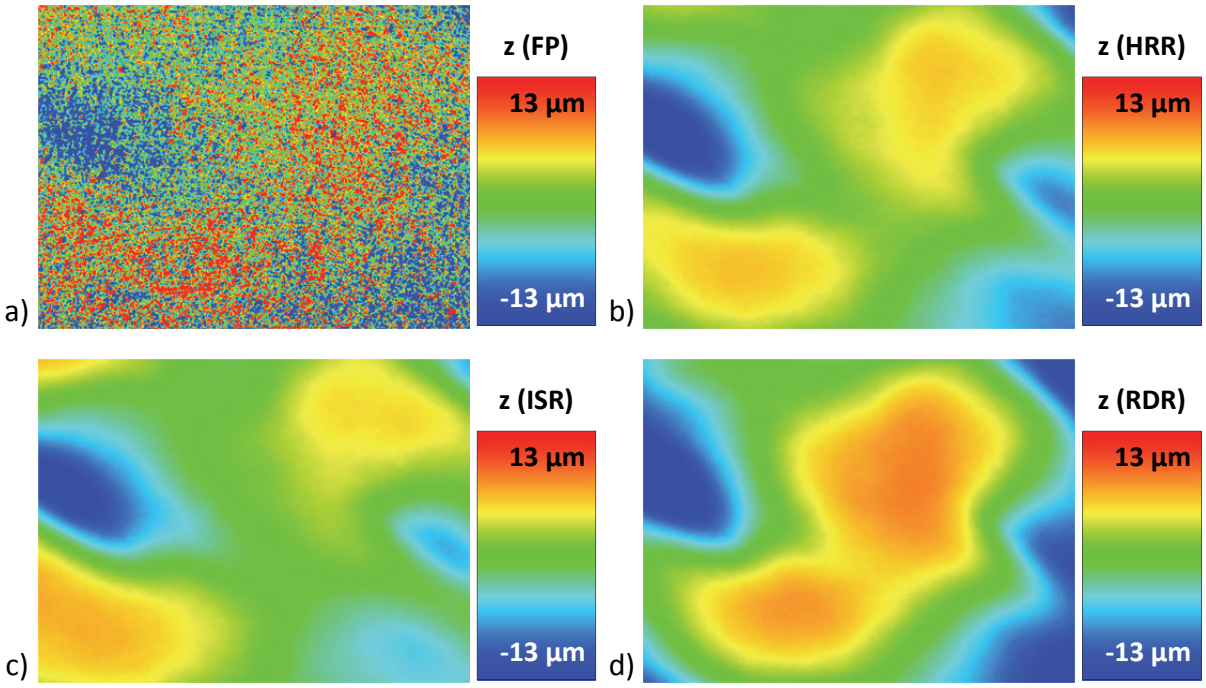

Figure 31: Shape with tilt removed, from measurement of plane technical surface (see Figure 16 in section 3, lateral size of evaluated field: 38 x 28 mm²) displaced by z=-10 mm to the reference point p_{Ref} in the reference coordinate system (i.e. input $d_z \neq d_{z,Ref}$), with FP and PMD using different regularization methods: a) Data from FP measurement; b) Data from HRR-evaluated PMD measurement; c) Data from ISR-evaluated PMD measurement, using a plane shape model; d) Data from RDR-evaluated PMD measurement, using input $d_z = d_{z,Ref}$, showng an increased dynamic due to incorrect object position (see text).

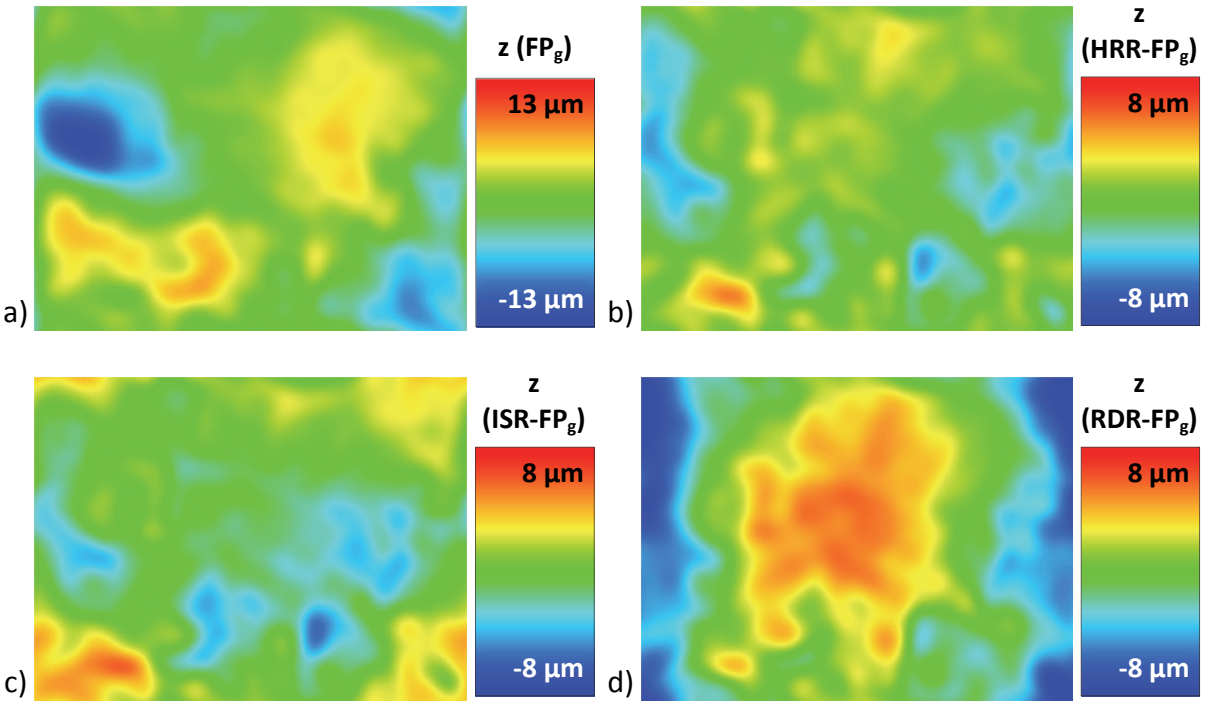

Figure 32: Filtered FP shape data $z(FP_g)$ (with tilt removed) and its differences to PMD shape images shown in Figure 31. a) Filtered FP shape data $z(FP_g)$ (Gaussian kernel, 20x20 pixels) with tilt removed; b) z(HRR)- $z(FP_g)$, showing only local deviations; c) z(HRR)-$z(FP_g)$, showing parabolic deviations (see edges of image) due to an inaccurate shape model (compare to calculated error $\Delta z \approx 7$µm) d) z(RDR)-$z(FP_g)$, showing stronger parabolic deviations due to an incorrect input distance d_z (compare to calculated error $\Delta z \approx -14$µm).

From ISR evaluation of repeated measurements, an average corrected output value of d_z= - 15.03 mm ± 0.01 mm was retrieved. As the object was correctly positioned, this indicates that the plate is not flat, but has a curved form so that the ISR algorithm converges to a solution which gives the best plane-like shape data (see Figure 31c), but at an incorrect distance estimate with Δd_z = 5.03 mm ± 0.02 mm. This is of course an inherent problem that emerges when applying ISR for the measurement of objects of unknown shape. Using equation (9), a parabolic shape error of $\Delta z \approx 7.50$ µm is retrieved, which shows as an increased dynamic of the error image (using FP shape data as reference) shown in Figure 32c. The distance estimation error Δd_z = -10.00 mm ± 0.02 mm for the RDR-evaluated measurement results in an increased dynamic in the shape data, see Figure 31d. The parabolic shape error of $\Delta z \approx$ -14.09 µm calculated from Δd_z is in good agreement with the dynamic of the error image in Figure 32d. As the distance errors for ISR and RDR evaluation have opposite sign, the parabolic errors have an opposite orientation, as can be seen comparing the respective error images in Figure 32c and Figure 32d.

From repeated measurements and evaluation, the pixelwise standard deviation images σz_p were calculated, which are shown in Figure 33. The σz_p images express a spatially resolved repeatability (see section 7.1.2), including offset between measurement. It can be seen here that the HR-regularized shape data have a much better repeatability than the data from FP and ISR evaluated PMD measurements. RDR-based shape data have very low deviations between measurements, since a constant input $d_z = d_{z,Ref}$ is used for evaluation, resulting in nearly constant Δd_z and thus shape error Δz.

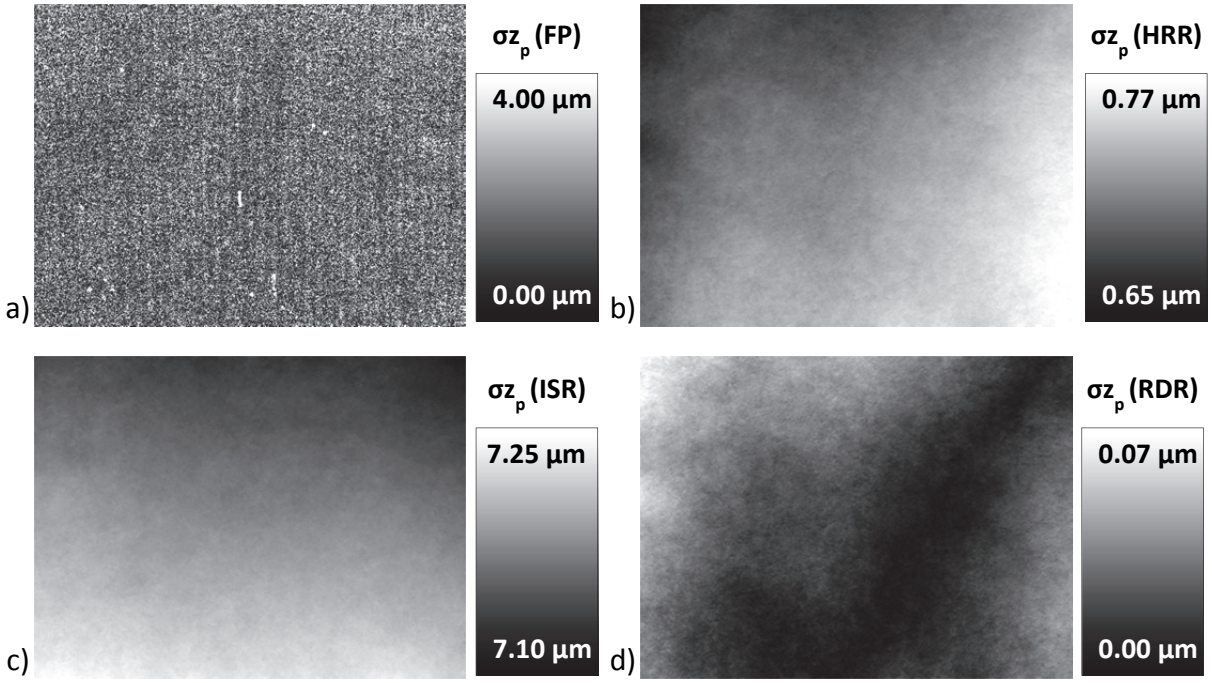

Figure 33: Pixelwise standard deviation images σz_p (see section 7.1.2) of shape data from repeated measurements of plane technical surface (see Figure 16 in section 3), for: a) FP, showing high pixelwise variation, suggesting lower repeatability; b) PMD using HRR, low offset deviation with small dynamic range; c) PMD using ISR (plane shape model), large deviations due to individual shape model and object distance approximations in each measurement; d) PMD using RDR, minimal deviation between calculated shapes. See Table 9 for image statistics.

Statistics for the standard deviation images σz_p are shown in Table 9. $Avg(\sigma z_p)$ can be interpreted as the average global repeatability, while $\sigma(\sigma z_p)$ describes the spatial variation of the measurement deviation. The data from repeated HRR measurements have much less deviations than the input FP shape data, which suggests that local errors in the FP data are not directly propagated to the HRR shape output.

Shape data from ISR-based PMD evaluation have low spatial variations, but large global deviations, as for each measurement the global position is calculated from a best-fit of the phase measurement data to the shape model. Lowest deviations are found for shape data from RDR evaluation, as here a static position for the reference point is set and the deviations are only attributed to noise in the phase measurement data.

As a summary of the measurements of the flat metallic plate presented in this section, it can be stated that the global shape from HRR-based evaluation is smoother than the input FP shape data, and is in better accordance to the shape from FP measurement than the shape from ISR- and RDR-based evaluation.

Table 9: Statics of pixelwise standard deviation images (see Figure 29) from shape measurement of flat metallic plate, describing the repeatability of the measurements as scalar values (see section 7.1.2). Shape data from repeated HRR measurements have much lower global and local deviations than the input data from FP measurement and shape data from ISR evaluation.

Method	**Avg (σz_p) / µm**	**σ (σz_p) / µm**
FP	1.99	16.30
PMD (HRR)	0.72	0.02
PMD (ISR)	7.18	0.03
PMD (RDR)	0.02	0.01

7.2.2 Diamond-turned mirror with known radius

The diamond-turned concave spherical mirror shown in Figure 34 is another example for a technical surface with mixed reflective behavior, a photo of the reflective object is shown in Figure 34a. As shown in Figure 34b and c, the surface generally gives good modulation for both scattered and reflected fringes, making HRR-based evaluation feasible. The phase measurement was performed using fringe periods of 50 pixels for FP and 100 pixels for PMD measurements. As can be seen in Figure 35 (left: *M* for camera 1, right: *M* from camera 2), for the FP measurement *M* is acceptable, the central point of the diamond turning process has the best *M*, and in both images scratches can be seen. For PMD, the modulation of the reflected reference pattern is generally high, but decreases with distance from the center (see Figure 34c and Figure 35c), which is induced by a lateral variation of the tooling traces from the production process.

From measurements of the surface using a CMM, performed by the manufacturer, a nominal radius of the mirror of r_{nom} = -200.063 mm ± 0.005 mm is known. To test the ability of the HRR, ISR and RDR based evaluation to retrieve the correct radius of the object as a function of the measurement object's position in the setup, a series of measurements was performed with the spherical mirror positioned at three different distances d_z. The object was initially positioned as accurately as possible at $d_z = d_{z,Ref}$, and moved upwards and downwards by 10 mm between the measurement series.

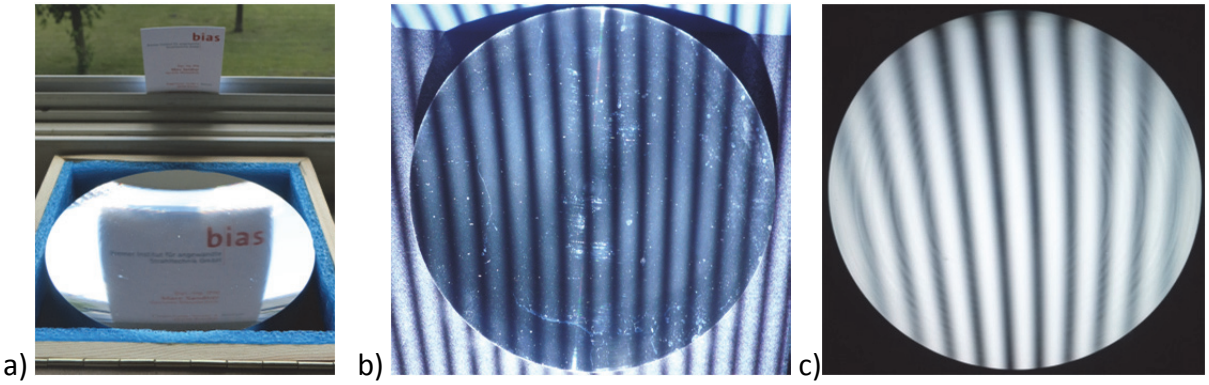

Figure 34: Diamond-turned concave spherical mirror (radius of curvature r_{cur} = -200mm, lateral diameter = 159 mm) with mixed and locally varying reflective properties; a) Photo of the object; b) Fringe pattern projected on the surface with a standard computer projector. c) Fringe pattern (from a computer monitor) reflected by the surface.

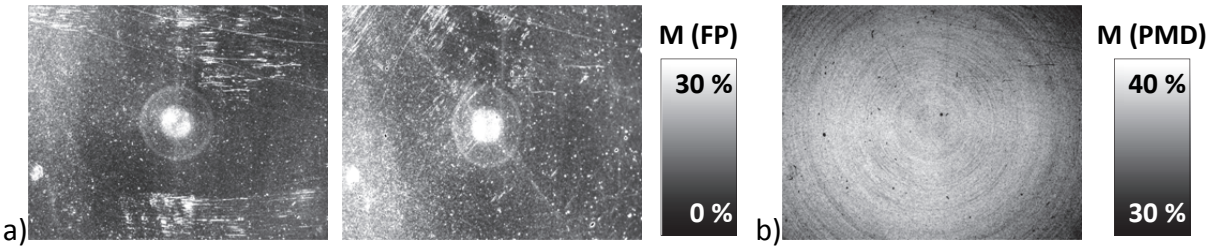

Figure 35: Fringe modulation *M* averaged from phase measurement in horizontal and vertical direction for measurement of spherical mirror, lateral size of evaluated field: 47 x 37 mm². a) *M* for FP phase measurement using fringe period of 50 pixels, with *M* from camera 1 (left image) and M from camera 2 (right image, rotated for comparability), showing locally varying modulation; b) *M* for PMD phase measurement using a fringe period of 100 pixels.

The evaluation with RPR was performed with a constant input $d_z = d_{z,Ref}$, and in ISR evaluation a spherical shape model was chosen. In the FP measurement scratches on the surface are visible in the fringe modulation images (see Figure 35a). These scratches could not be avoided by rotating the measurement object, and resulted in measurement artifacts in the output shape data (see Figure 36a). For each of the measured shape data sets, a numerical fit using a spherical model was performed. In the residuals from the spherical fit for FP and PMD measurement with the object at $d_z = d_{z,Ref}$, shown in Figure 36, the tooling traces from the production process can be seen in the PMD shape data, but not in the data from FP measurement due to lacking depth resolution.

A comparison of constancy of the evaluated shape data depending on the object position d_z is shown in Figure 37 and in Table 10. For RDR-based PMD evaluation, the radius r_{fit} of the best-fit sphere varies strongly for different object positions (approx. 7 mm fit radius difference for $|\Delta d_z| = 10$ mm) due to an assumed constant object position d_z. Sphere radii retrieved from shape data from ISR evaluation show only weak dependence on the object distance d_z, but maximum deviations of 805 µm to the nominal radius. This is surprising, especially when comparing this to the radii from FP measurement (maximum deviations of 424 µm to the nominal radius); also, both deviations appear to be symmetric. This is a topic of further research, which is outside the scope of this work.

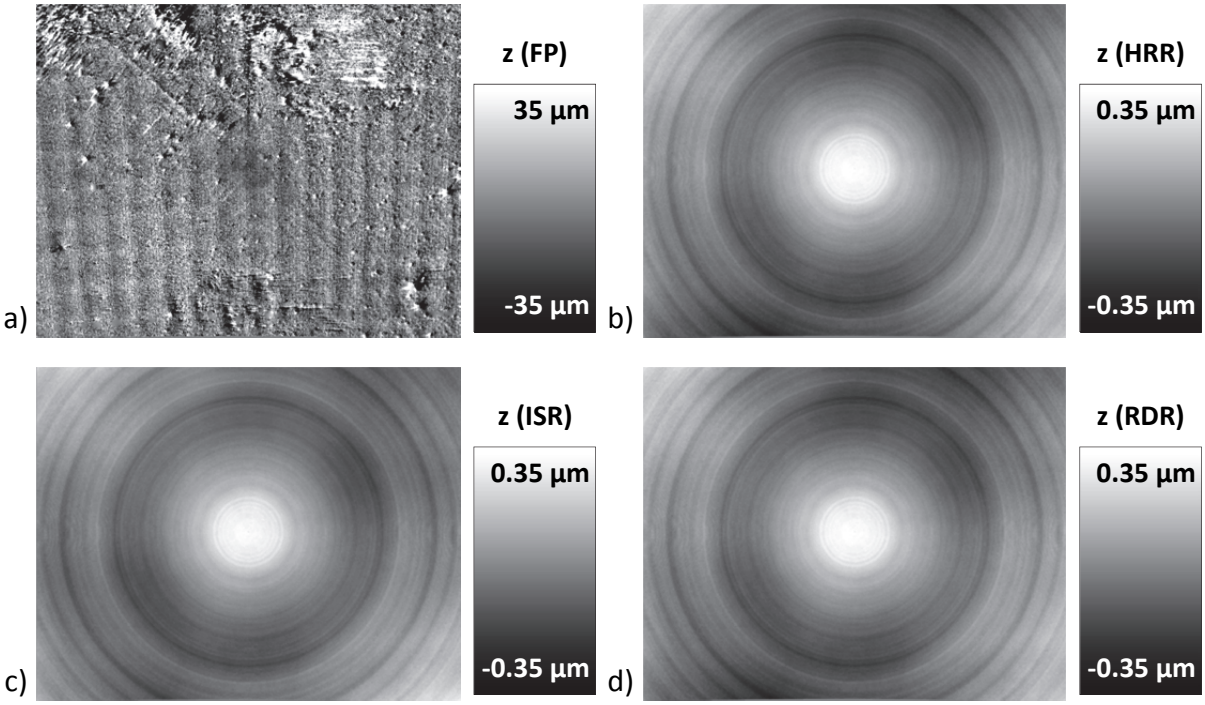

Figure 36: Residuals of numerical fit (spherical model without radius constraint) of shape data from measurement of diamond-turned spherical mirror (see Figure 34, lateral size of evaluated field: 47 x 37 mm²) with FP and PMD at z = 0mm in the reference coordinate system (i.e. input $d_z = d_{z,Ref}$), evaluated using different regularization methods: a) Data from FP measurement (fit radius r_{fit} = 199.878 mm) showing strong noise, artifacts from specular reflection at scratches, and phase measurement artifacts (periodic structures); b) Data from HRR PMD measurement (r_{fit} = 200.197 mm); c) Data from ISR PMD measurement, using a spherical shape model without radius constraint (r_{fit} = 200.843 mm); d) Data from RDR PMD measurement, using input $d_z = d_{z,Ref}$ (r_{fit} = 200.278 mm).

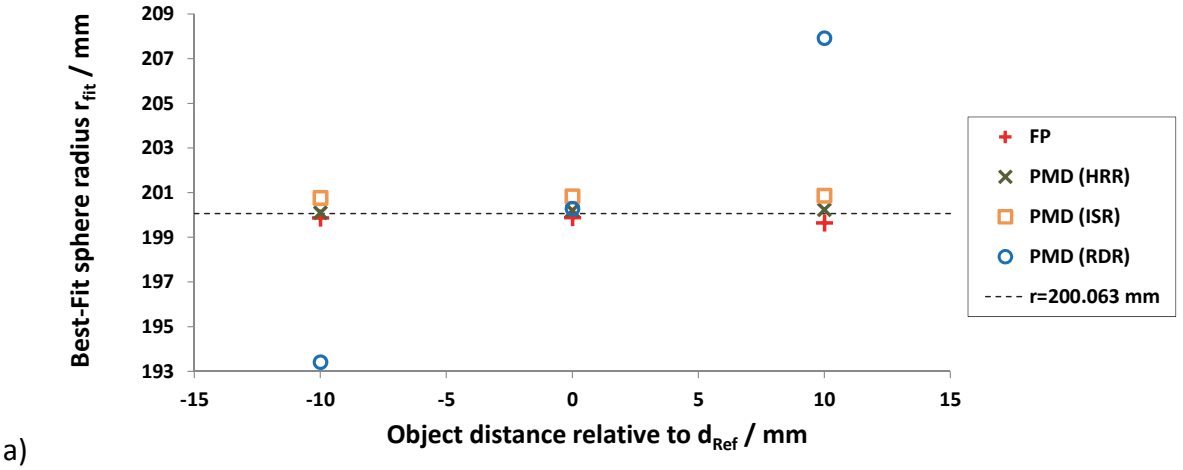

a)

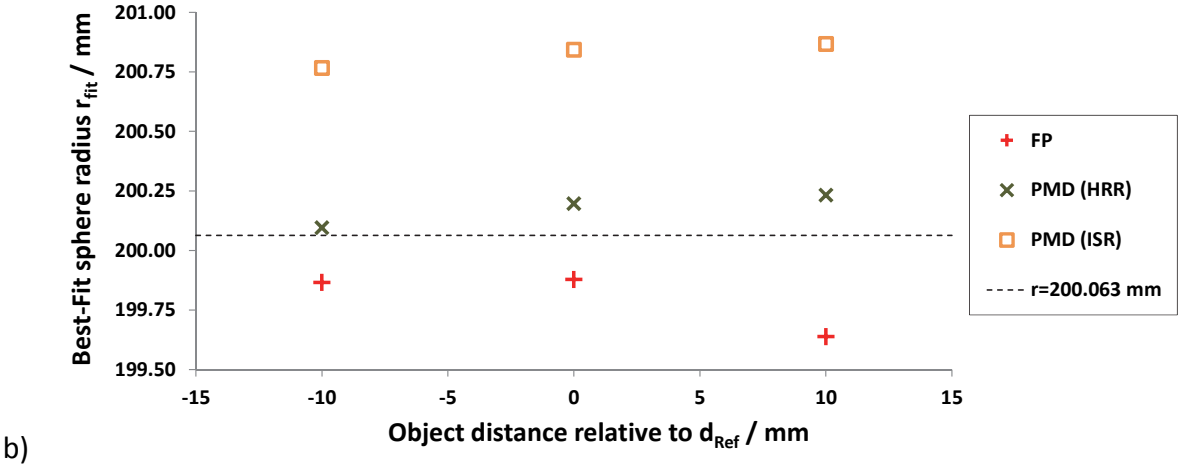

b)

Figure 37: Comparison of consistency of shape calculated from FP and PMD using different regularization methods: Measured radius of spherical object shown in Figure 34 (nominal radius of curvature: 200.063 mm ± 0.005 mm) calculated from shape data from measurements with FP and PMD using evaluation methods, with the object positioned in the measurement volume and object distance d_z varied by -10 mm, 0 mm, and 10 mm to the reference distance $d_{z,Ref}$. The same data are shown in (a) and (b) with different scaling on the y-axis. Uncertainties from repeated measurements have been omitted but are given in Table 10 (part of the data from [San14]).

Table 10: Measured radii of spherical mirror shown in Figure 34 (nominal radius of curvature: 200.063 mm ± 0.005 mm), from shape measurements with FP and PMD (evaluated using HRR, ISR and RDR), with object positioned at different object positions d_z. Specified errors were calculated from standard deviation of three repeated measurements. The fit radius r_{fit} of the best-fit sphere from HRR-based shape calculation shows much better constancy over varying object positioning than r_{fit} from RDR -based shape calculation, indicating that object positioning is not needed for HRR measurement (part of the data from [San14]).

	$d_{z1} = d_{z,Ref} - 10$ mm	$d_{z2} = d_{z,Ref}$	$d_{z3} = d_{z,Ref} + 10$ mm
r_{fit} (mm) (**FP**)	**199.866** ± 0.006	**199.878** ± 0.006	**199.639** ± 0.012
r_{fit} (mm) (**PMD** (**HRR**))	**200.096** ± 0.002	**200.197** ± 0.015	**200.232** ± 0.003
r_{fit} (mm) (**PMD** (**ISR**))	**200.767** ± 0.007	**200.843** ± 0.002	**200.868** ± 0.022
r_{fit} (mm) (**PMD** (**RDR**))	**193.407** ± 0.002	**200.278** ± 0.006	**207.920** ± 0.005

The radius r_{fit} from data from HRR evaluation is less sensitive to a change in the object position than the data from RDR-based evaluation, showing a fit radius variation of less than 137 µm ± 20 µm for all object positions.

The measurement results in this section show that HRR-based evaluation can be used for accurate shape reconstruction. As in ISR-based evaluation, the shape data from HRR-based evaluation are much less susceptible to the object position in the measurement volume than the shape data from RDR-based evaluation, indicating that manual positioning of the object is obsolete for HRR measurement.

7.3 Technical surface with spatially varying reflective properties

In this subsection, combined GOP measurements of a free-form object with unconnected surface regions with varying reflective behavior are presented. The object surface, shown in Figure 38, can be segmented into the regions shown in Figure 38c by its height and lateral connectedness:

- R1: Specularly reflective, rectangular region (with hole), left side of the image
- R2: Scattering milled region around R3 (with holes)
- R3: Specularly reflective, circular region in the object center
- R4: Specularly reflective, rectangular region (with hole), right side of the image

Since the specular regions R1, R2 and R4 are unconnected this object is well suited for demonstrating the capability of HRR for single-camera PMD shape measurement of discontinuous surfaces, which is not feasible using ISR or RDR for PMD measurement evaluation. As a reference measurement, the object has been measured with a sliding caliper (Mitutoyo Digimatic) along the axis z_M shown in Figure 38b.

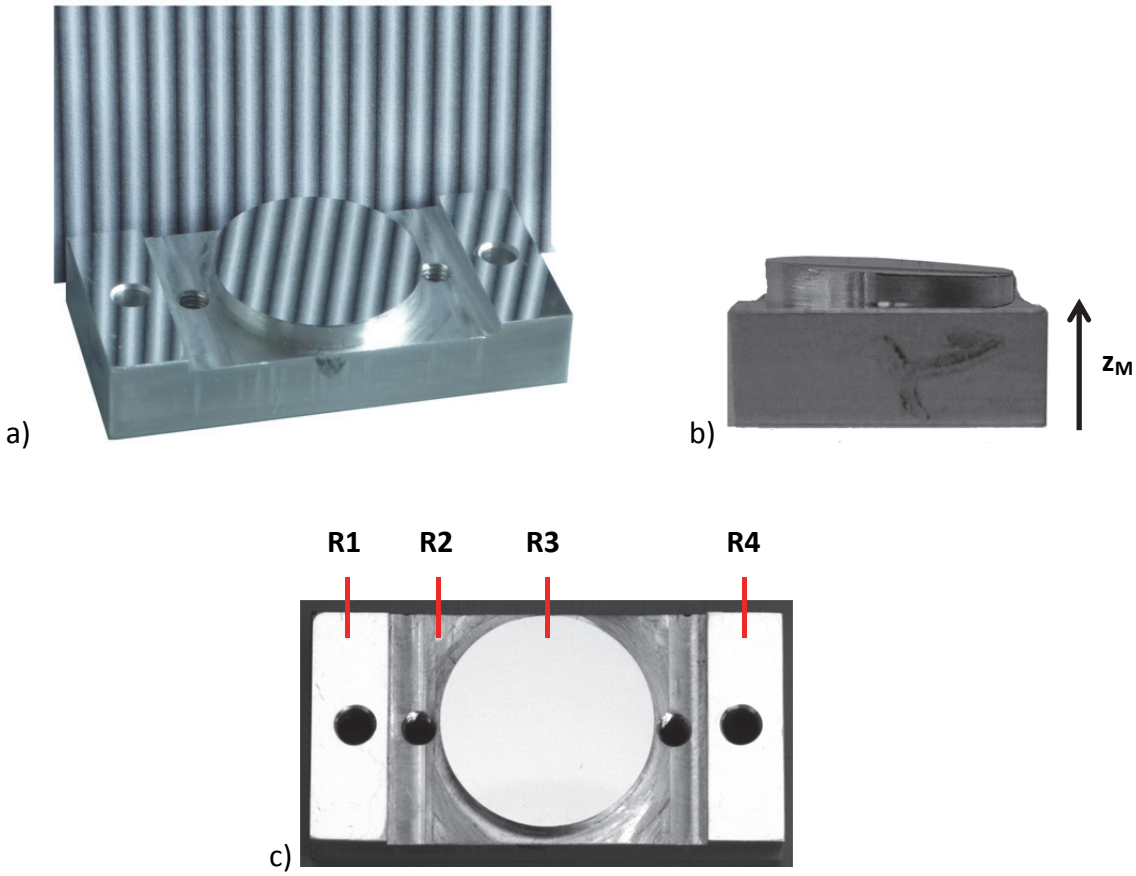

Figure 38: Photos of free-form object consisting of unconnected surface regions with locally varying reflective behavior: Specular reflectance in the central circular region and in rectangular regions at the left and right border, scattering in the lower-set region. a) The object in front of a printed-out sinusoidal pattern; b) Side view of the object showing tilt of the central circular region, with arrow indicating axis z_M of the mechanical measurement; c) View from top as imaged with object inside the combined GOP measurement system, with depiction of regions R1, R2, R3 and R4.

As shown in Figure 39b, the circular central region R3 is slightly tilted in reference to R1, R2 and R4, which are parallel to each other. For the tilt of R3 in reference to R2, a peak-to-valley height difference of 0.86 mm ± 0.04 mm (uncertainty from repeated measurements) was measured. The lateral diameter s_{R3} of R3 was measured as 19.00 mm ± 0.02 mm.

The average heights in the flat regions R1, R2 and R4 were calculated as the average of laterally distributed sample measurements on the surfaces. As described at the end of this subsection (7.3.2) , from HRR-based measurement it was found that R3 approximately resembles a concave sphere with a radius r_{fit} of 397.063 mm ± 0.007 mm. The center of area c_z on the symmetry axis of a spherical section of height h is positioned at $h/2$ ([Bre29], [Wik15]), to be calculated using the sphere radius r_{fit} and the lateral diameter s_{R3}:

$$c_z = \frac{h}{2} \;, with \quad h = r_{fit} - \sqrt{{r_{fit}}^2 - \left(\frac{s_{R3}}{2}\right)^2} \,. \tag{12}$$

Using this formula and accounting for the influence of the slight tilt of R3 (2.82° ± 0.02°), the average height h_{R3} of R3 in reference to R2 can be calculated from the mechanically measured minimum and maximum heights of R3 as:

$$\begin{aligned} h_{R3} &= \left(\frac{3.20\ mm + 2.26\ mm}{2} - cz\right) \cdot \cos(2.82°) \\ &= (2.73\ mm - 0.06\ mm) \cdot 0.999 = 2.67\ mm \,. \end{aligned} \tag{13}$$

This allows calculation of the relative positioning of all regions in reference to each other. All results from the mechanical measurement and the calculated average height for R3 are shown in Table 11.

Table 11: Average height of regions shown in Figure 38 along axis z_M, in reference to region R2 plane, from sample measurements with Mitutoyo Digimatic sliding caliper. For every region, measurements at different positions were performed, for which the average value is given with the standard deviation of the values as measurement uncertainty. While for the parallel regions R1, R2 and R4, the measurement positions were chosen randomly, for the tilted region R3 the peak height positions in reference to R2 were measured. The average height in R3 was calculated using knowledge of the shape from HRR measurement (concave sphere with r_{fit} =397.063 mm ± 0.007 mm), see section 7.3.2.

Region	Average z_M in region / mm	Peak-to-valley z_M difference in region / mm	Average z_M in reference to R3 / mm
R1	1.16 ± 0.01	0.00 ± 0.01	1.52 ± 0.08
R2	0.00 ± 0.01	0.00 ± 0.01	2.67 ± 0.08
R3	2.67 ± 0.07	0.86 ± 0.02	n. a.
R4	1.16 ± 0.01	0.00 ± 0.01	1.52 ± 0.08

Three repeated combined GOP phase measurements (each consisting of a FP and PMD phase measurement) of the object were performed using FP (P = 24 pixels) and PMD (P = 24 pixels). The resulting fringe modulation M images are shown in Figure 39 and Figure 40. The fringe modulation from the FP phase measurement (shown in Figure 39a and b for camera 1 and camera 2 respectively) is high in the scattering regions and partly acceptable in the specularly reflective regions. Due to the reference patter projector, camera 1 and camera 2 having different perspectives on the object, shadowing occurs (indicated by arrows in Figure 39 b). Additionally, in R2 multiple reflections from surrounding shape elements can be observed, which does not alter the fringe modulation in phase measurement but, as well as shadowing, leads to a large remaining error when intersecting rays of sight in the FP shape calculation. From this error, the *FringeProcessor* software automatically calculates a mask which is shown in Figure 39c). As not all pixels are valid, images shown in this section are not rescaled (see section 7.1.1).

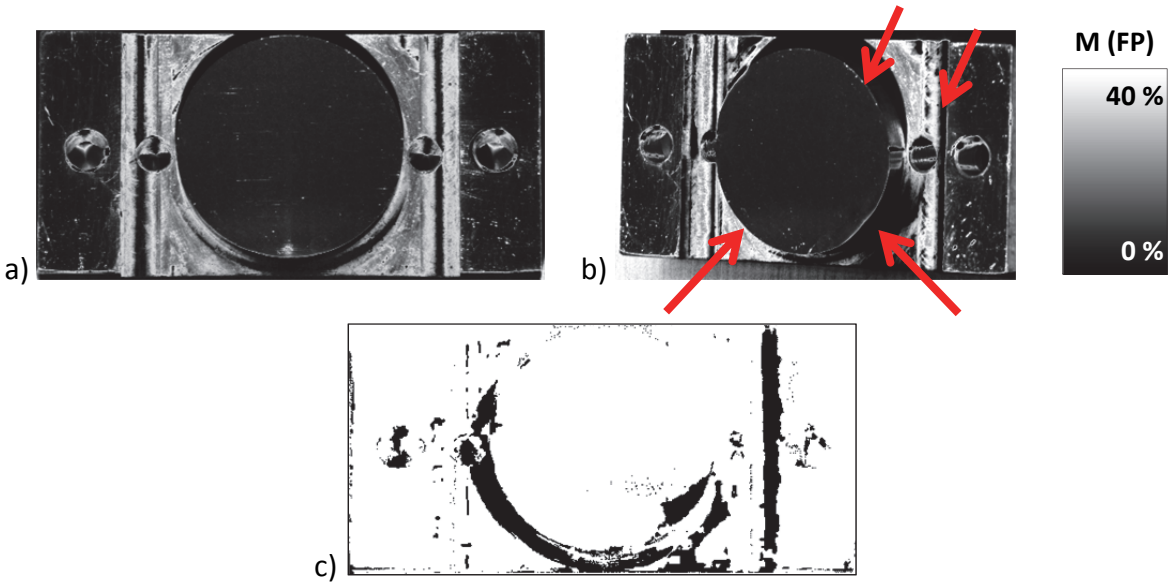

Figure 39: Fringe modulation *M* and validity mask from FP phase measurement of a free-form object (lateral size: 40x20 mm²) consisting of unconnected surface regions shown in Figure 38: a) *M* from FP phase measurement of camera 1. The scattering region has high modulation, while the specular regions have lower modulation; b) *M* from FP phase measurement of camera 2 (rotated by 180° for compliance with image a), arrows point to regions shadowed due to the different perspectives on the object; c) Data validity mask containing the valid pixels from both cameras calculated from ray intersection error. Not all shadowed regions are correctly identified.

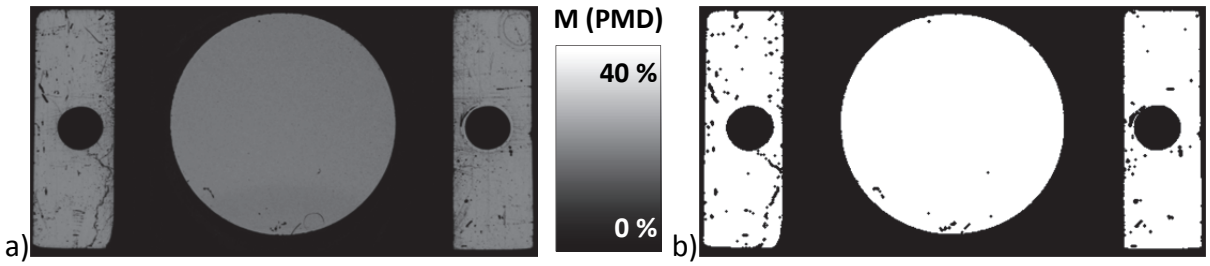

Figure 40: a) *M* from PMD measurement, showing high values for *M* only in reflective regions; b) Data validity mask for PMD showing areas with *M* larger than the global threshold t_{Mask} = 10%, after applying a morphological erosion filter (3x3 cross kernel) in order to remove pixel on the regions' edges . Black pixels denote exclusion from shape calculation.

For the PMD phase measurement (Figure 40a), the specularly reflective regions show higher values for *M*, with a few dark line-like segments indicating scattering induced by scratches on the surface. Very low values for *M*, leading to invalid PMD data, are observed on R2. The data validity mask, created by setting pixels with $M > 10\%$ as valid and applying a morphological erosion filter (3x3 cross kernel) in order to remove pixels on the regions' edges, is shown in Figure 40b.

7.3.1 Evaluation and preparation of shape data from FP measurement

The shape data calculated from the FP phase measurement are shown in Figure 41, invalid areas are shown in black. In the shape image, the different heights of the separate surface regions can be identified. These regions can also be identified as three distinct distributions (from left to right: R2, (R1 and R4), R3) in the histogram of the shape image shown in Figure 42. The fringe-like vertical structures visible in the specular regions R1, R3 and R4 in Figure 41 are artifacts from the phase measurement.

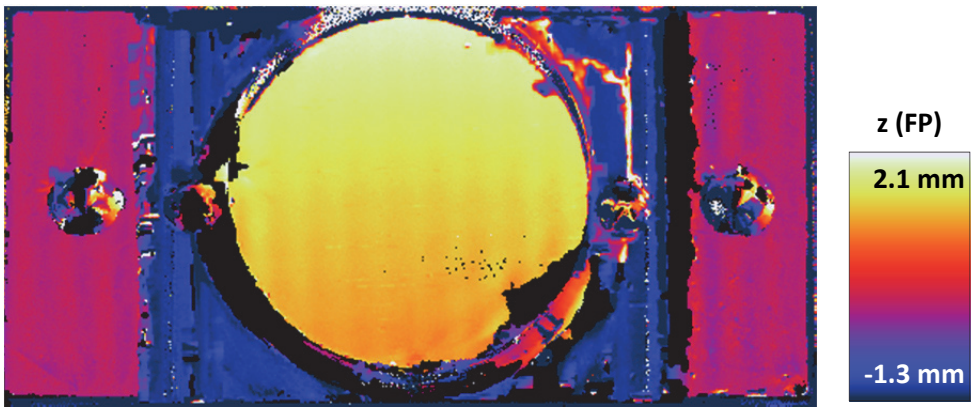

Figure 41: Shape data from FP measurement, with tilt removed using shape data from R2 for calculation of the reference plane, invalid pixels shown in black.

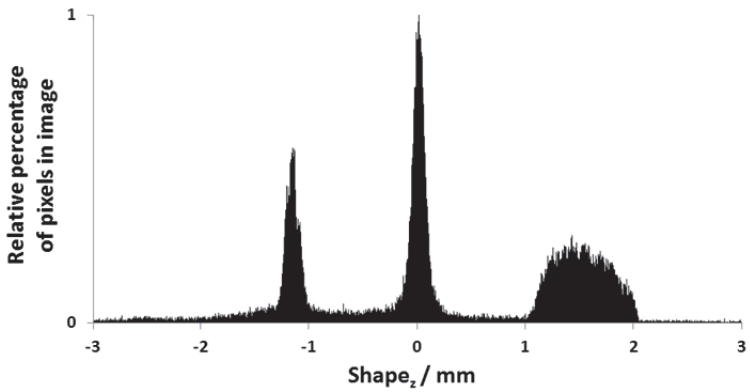

Figure 42: Histogram of the shape image from FP measurement shown in Figure 41, showing three separable distributions (left distribution: R2, central distribution, R1 and R4, right distribution: R3)

The pixelwise standard deviation from repeated FP measurements shown in Figure 43 can be regarded as the repeatability of the measurement. Although it contains several invalid regions, the best repeatability is found in the scattering region R2 with an average value of 4.0 µm. The standard deviation of repeated measurements is higher in the reflective regions, with an average of 8.8 µm in R3 and an average of 11.6 µm in regions R1 and R4 combined.

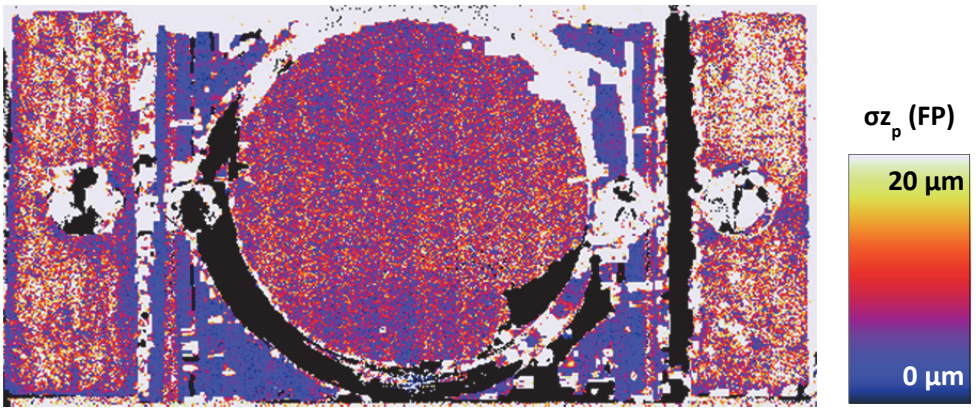

Figure 43: Pixelwise standard deviation σz_p of shape data from repeated FP measurements, invalid pixels shown in black.

As described in section 2.2.2.1 and shown in Figure 10, shape calculation in single-camera PMD systems is extremely sensitive to the accuracy of the input height data. For evaluation of data consisting of a single larger region, as shown in section 7.2, it was assumed that the large count of shape data points from FP measurement available in HRR-based shape calculation makes the algorithm more robust to local outlier values. In order to provide initial shape data of better quality for HRR-evaluation of the smaller and unconnected valid PMD regions from measurement of the freeform object, outlier FP shape data with a pixelwise standard deviation of larger than 7 µm were also set as invalid in the FP pixel validity mask.

In order to use FP data for HRR evaluation, each evaluated pixel has to be valid in the FP shape data as well as in the PMD phase data. To allow evaluation of the data at all pixel positions set as valid by the PMD validity mask, an interpolation of FP shape data was needed for invalid pixels. As Figure 41 shows, not only do the FP data have local peaks of outliers, but also larger invalid areas which are sometimes located at the edges of the valid image data. Because of this, simple kernel-based image filtering was not considered to be adequate. Thus, a method suitable for filling data at the invalid regions by interpolation and extrapolation (i.e. at the data boundary) was developed (see section 10.1.2) and applied to the FP shape data as a preparation for HRR evaluation.

7.3.2 HRR evaluation

Since in the PMD phase measurement *M* was insufficient in region R2, the HRR-based shape calculation was only performed in the valid regions shown in Figure 40b. As the regions R1, R3 and R4 are not connected to each other, HRR evaluations were performed separately for each of the regions, using the filtered FP shape data as input. After evaluation, the separate shape images were recombined. The resulting shape image, with overall tilt removed using input data from R1 and R4, is shown in Figure 44. The dynamic range of the image shows good agreement with the mechanically measured object proportions shown in Table 11.

Again, the spatially resolved repeatability error was calculated as the pixelwise standard deviation of the raw shape data (i.e. without tilt removal) from repeated combined GOP measurements. Maps of the repeatability are shown in Figure 45. A repeatability of < 1.03 µm for all regions demonstrates the general feasibility of HRR for evaluation of unconnected regions. The dynamic range of the repeatability maps is quite narrow, which indicates an overall offset between the individual measurements rather than spatial variation of the measurement result.

Figure 44: HRR- based shape reconstruction of the mirror shown in Figure 34 using filtered shape data from FP measurement as input data. For regions R1, R3 and R4, separate shape calculations were performed using the respective segments in the PMD mask shown in Figure 47, the image shown here is a combination of the individual shape results.

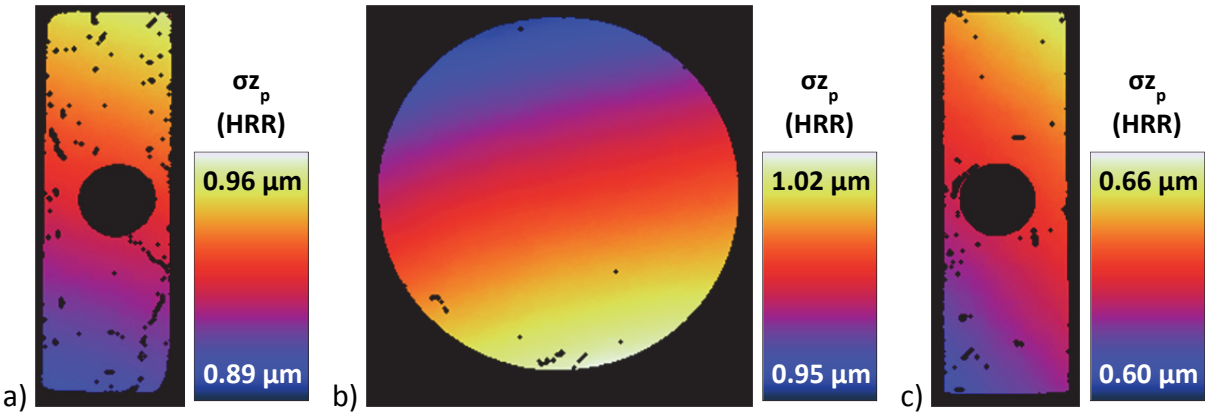

Figure 45: Pixelwise standard deviation of absolute shape (no tilt removed) for HRR-evaluated PMD measurements, for regions R1(a), R3(b) and R4(c), which can be interpreted as a spatially resolved repeatability.

The average z position in the shape data with overall tilt removed using R1 and R4, and deviations to the mechanical measurement are shown in Table 12. For HRR-evaluated regions R1, R3 and R4, the repeatability of the average height in each region is < 285 nm. Taking the mechanically measured shape values (see Table 11) as ground truth data, the resulting height differences between surface regions from HRR evaluation using filtered data have errors of <24 µm, which are within the uncertainty of the mechanical measurement (80 µm, see Table 11). The height difference for R2 (from FP measurement) also is in good agreement with the mechanical measurement, with an error of 9 µm.

Table 12: Statistics for different regions in the shape images (with tilt removed using data from R1 and R4), from repeated HRR-evaluated measurements using filtered data from FP shape measurement as input (for regions R1, R3 and R4), and from FP measurements (R2). Uncertainties were calculated as standard deviation from repeated measurements. In the rightmost column, deviations to the mechanical measurement are given, with uncertainties calculated as the sum of the uncertainties from mechanical and HRR (R1, R4) and FP (R2) measurements.

Region	Average z in region / µm	Peak-to-valley z difference in region /µm	Average z in reference to R3 / µm	Deviation to mech. meas. of (Average z in ref. to R3) / µm
R1	-0.231 ± 0.003	16.596 ± 0.001	1495.271 ± 0.281	23 ± 80
R2	-1168.303 ± 1.633	455.801 ± 7.898	2663.751 ± 1.354	9 ± 81
R3	1495.448 ± 0.284	957.753 ± 0.093	n. a.	n. a.
R4	-0.226 ± 0.003	30.048 ± 0.092	1495.674 ± 0.287	16 ± 80

As R3 is the only region with a non-flat shape and no reference measurement was available for the object, the shape was to be determined from the measured data. From visual observation, the region was assumed to be a concave sphere, so that a numerical fit with a spherical model without radius constraint was performed on the shape data in R3. In the shape residuals from this fit (output radius r_{fit} = 397.047 mm ± 0.007 mm, uncertainty from repeated measurements), shown in Figure 46a, strong astigmatism can be seen, indicating that the shape has deviations to the spherical form. The standard deviation of the fit residuals (fit radii varying by ± 0.007 mm), shown in Figure 46b, are less than 2 nm.

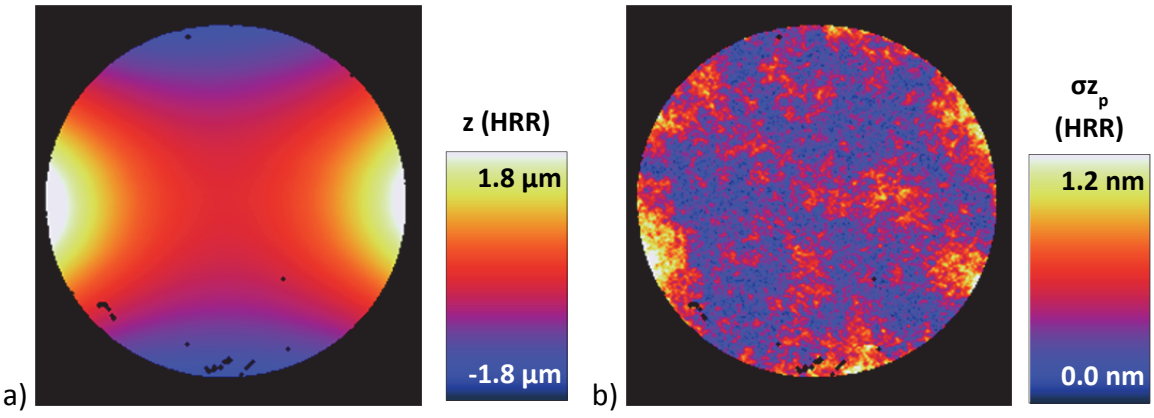

Figure 46: a) Residuals of numerical fit (spherical model without radius constraint) of HRR-evaluated PMD measurement, with output radius r_{fit} = 397.047 mm ± 0.007 mm, the residuals show strong astigmatism. b) Standard deviation images σz_p of residuals from repeated measurements (fit radii varying by 0.007 mm).

Fusing the measured data of all surface regions, the shape images from FP and HRR-based PMD measurement were combined. A tilt removal was performed on the combined point cloud using the shape in regions R1 and R4 as input data, applying the coordinate transformation to the complete data set so as to maintain the relative positions of the individual surface regions. The resulting shape image is shown in Figure 47.

Summarizing the measurements presented in this section, it was shown that shape measurement of unknown objects with unconnected surfaces is feasible with HRR-based PMD measurement evaluation, and that the output shape data is in good accordance with reference measurements performed mechanically with a sliding caliper.

Figure 47: Combined shape image from FP measurement and HRR-based shape calculation. After fusion of the masked, but otherwise unprocessed data output from shape calculation, tilt removal was performed using the shape in H1 and H4 as input data. FP data from region R2 and HRR-evaluated PMD data from R1, R3 and R4 resemble the measured object well, showing the feasibility of measurement of unconnected surfaces with mixed reflective properties with HRR.

8 Summary, Conclusions and Outlook

In the work presented here a novel technique for measuring the shape of surfaces with partly specular or locally varying reflective behavior, such as technical surfaces, has been investigated. The technique is based on subsequently performing measurements of the object with the geometric-optical phase measurement techniques (GOP) Fringe Projection (FP) and Phase Measuring Deflectometry (PMD), and fusing the acquired phase data. A novel regularization scheme for PMD data evaluation, termed *Hybrid Reflectometry regularization* (HRR), was implemented and described. For experiments, a combined GOP system was assembled and calibration of a camera and the system geometries of the FP and PMD was performed. With this combined GOP system FP and PMD phase measurements of two partly specular technical surfaces, namely a planar and a spherical object with known radius, as well as an object comprised of unconnected surfaces with dissimilar reflective properties were performed. From the measured data, PMD shape calculations were performed using HRR and the established Initial Shape (ISR) and Reference Distance (RDR) regularization methods, and the resulting shape data were compared with data from mechanical and FP measurements.

- The comparison showed that for the planar object, shape data from HRR-based PMD evaluation are similar to data from ISR-based evaluation and much smoother than shape data from FP measurement which is used as the input initial shape.

- It was shown that the radius of a spherical object measured using HRR evaluation was closer to the nominal radius given by the manufacturer than the radius retrieved from ISR or RDR-based evaluation, and shows very small dependence on the object position in the measurement volume.

- The feasibility of HRR-based shape measurement for unknown objects with unconnected surfaces was shown, which is not feasible using ISR or RDR shape evaluation.

In summary, a proof of principle for the HRR-based PMD shape evaluation was demonstrated, which has a large potential for measuring partly reflective objects with unconnected surface regions using FP and single-camera PMD.

In the experiments, while PMD measurements and evaluation were performed using a single camera, a second camera was used for FP measurement. For further development of the technical implementation, two possible courses of action can be identified. The potential of using a single camera in the setup for both FP and PMD measurement would enhance the potential for integrability of the combined GOP technique into portable systems. Additionally, HRR could be used to help resolve shape ambiguities arising when measuring certain surfaces with Stereo-PMD (see section 2.2.2.1).

As a future improvement for the described algorithm, the existing integration algorithm could be replaced by a least-squares based evaluation approach yet to be developed, which implements weighting of the input FP shape data and PMD phase data by a data reliability estimator (e. g. the fringe modulation M). This approach would not only replace data interpolation for locally invalid input FP shape data, but could be considered as being optimized for the acquired data, as all available measurement information would be used. A similar approach could be used for developing a combined system geometry calibration in order to achieve an optimal alignment between the FP and PMD subsystems' coordinates. The strategy for combined FP / PMD system geometry calibration described in [Bre09] could be modified for usage in single-camera PMD systems.

To this time, integration of gradient data from single-camera PMD measurements has not yet been thoroughly characterized in its system theoretical properties. As the work presented here, to the best knowledge of the author, describes the first approach of incorporating data from FP measurement into PMD gradient integration, investigations on the influence of outliers in the initial shape on the calculated output are necessary in order to make the described technique robust for usage in industrial environments.

9 References

[Abh14] Abheiden, M.: *Optische Methoden zur Bestimmung von Oberflächenrauheiten.* MSc Thesis, University of Oldenburg / BIAS, 2014.

[Bal08] Balzer, J.: *Regularisierung des Deflektometrieproblems-Grundlagen und Anwendung.* Universität Karlsruhe, Karlsruhe: Universitätsverlag Karlsruhe, 2008

[Bal10] Balzer, J.; Werling, S.: *Principles of Shape from Specular Reflection*. Measurement 43, pp. 1305-1317, 2010

[Bal12] Balzer, J.: *A Gauss-Newton Method for the Integration of Spatial Normal Fields in Shape Space.* Journal of Mathematical Imaging and Vision 44, Springer US, pp. 65-79, 2012

[Bau08] Bauer, N., (Ed.): *Handbuch zur Industriellen Bildverarbeitung*. Stuttgart: Fraunhofer IRB, 2008

[Bey97] Beyerer, J.; Perard, D.: *Automatische Inspektion spiegelnder Oberflächen anhand von Rasterreflexion*. Technisches Messen 64, pp. 394-400, 1997.

[Bey12] Beyerer, J.; Puente León, F.; Frese, C.: *Automatische Sichtprüfung: Grundlagen, Methoden und Praxis der Bildgewinnung und Bildauswertung*. Berlin: Springer, 2012

[Bor97] M. Born, E. Wolf: *Principles of Optics*. Cambridge: Cambridge University Press, 1997

[Bot03] Bothe, T.; Gesierich, A.; Legarda-Sáenz, R.; Jüptner, W.: *3D-Camera*. Proc. SPIE 5144, pp. 295-306, 2003

[Bot04] Bothe, T.; Li, W.; v. Kopylow, C.; Jüptner, W.: *High-resolution 3D shape measurement on specular surfaces by fringe reflection*. Proc. SPIE. 5457, pp. 411-422, 2004

[Bot08] Bothe, T.: G*rundlegende Untersuchungen zur Formerfassung mit einem neuartigen Prinzip der Streifenprojektion und Realisierung in einer kompakten 3D-Kamera*. Dissertation, Strahltechnik Vol. 32, Bremen: BIAS Verlag, 2008

[Bot10] Bothe, T.; Li, W.; Schulte, M.; von Kopylow, C.; Bergmann, R. B.; Jüptner, W.: *Vision ray calibration for the quantitative geometric description of general imaging and projection optics in metrology*. Appl. Opt. 49, pp. 5851-5860, 2010

[Bre09] Breitbarth, M.; Kühmstedt, P., Notni, G.: *Calibration of a combined system with phase measuring deflectometry and fringe projection*. Proc. SPIE 7389, pp. 738909-1-8, 2009

[Bre29] Brewer, J. P.: *Lehrbuch der Statik fester Körper (Lehre vom Gleichgewicht der Kräfte an festen Körpern)*. Düsseldorf: Johann Eckhardt Schaub. URL: https://books.google.de/books?id=MydeAAAAcAAJ , 1829

[Bro01] I. N. Bronstein, K. A. Semendjajew, G. Musiol, H. Mühlig: *Taschenbuch der Mathematik*. Frankfurt am Main: Harri Deutsch, 2001

[Bur13] Burke, J.; Li, W.; Heimsath, A.; von Kopylow, C.; Bergmann, R.B.: *Qualifying parabolic mirrors with deflectometry*. J. Europ. Opt. Soc. Rap. Public. 8, pp. 13014, 2013

[Cre88] Creath, K.: *Phase-measurement interferometry techniques*. Progress in optics 26, pp. 349-393, 1988

[DEI98] DIN EN ISO 4287: 1998-10, *Geometrische Produktspezifikationen (GPS) – Oberflächenbeschaffenheit: Tastschnittverfahren – Benennungen, Definitionen und Kenngrößen der Oberflächenbeschaffenheit*, Berlin: Deutsches Institut für Normung e.V. (DIN), 1998

[DEI98b] DIN EN ISO 13565-1: 1998-04, *Geometrische Produktspezifikationen (GPS) - Oberflächenbeschaffenheit: Tastschnittverfahren - Oberflächen mit plateauartigen funktionsrelevanten Eigenschaften - Teil 1: Filterung und allgemeine Messbedingungen*, Berlin: Deutsches Institut für Normung e.V. (DIN), 1998

[DIN82] DIN 4760: 1982-06, *Gestaltabweichungen; Begriffe, Ordnungssystem*, Berlin: Deutsches Institut für Normung e.V. (DIN), 1982

[Ehr14] Ehret, G.; Quabis, S.; Schulz, M.; Andreas, B. & Geckeler, R.: Osten, W. (ed.): *New Sensor for Small Angle Deflectometry with Lateral Resolution in the Sub-millimetre Range*. Proc. Fringe 2013, Springer Berlin Heidelberg, pp. 887-890, 2014

[EMVA12] European Machine Vision Association: *EMVA Standard 1288 – Standard for Characterization of Image Sensors and Cameras Release 3.1, Release Candidate,* 2012

[Fis10] Fischer, M., Petz, M.; Tutsch, R.: *Bewertung von LCD-Monitoren für deflektometrische Messsysteme*. Sensoren und Messsysteme 2010, 2010.

[Fis11] Fischer, M.; Petz, M.; Tutsch, R.: *Phase Noise in Structured Illumination Systems*. Zagar, B.: Proc. 20th IMEKO TC2 Symposium on Photonics in Measurement, pp. 63-68, 2011

[Fis12] Fischer, M.; Petz, M., Tusch, R.: *Prediction of Phase Noise in Structured Illumination Measurement Systems*. tm - Technisches Messen 79, pp. 451-458, 2012

[Fis14] Fischer, M.; Petz, M.; Tutsch, R.: *Modellbasierte deflektometrische Messung von transparenten Objekten*. tm - Technisches Messen 81 , pp. 190–196, 2014

[Fra88] Frankot, R. T., Chellappa, R.: *A method for enforcing integrability in shape from shading algorithms*. IEEE Transactions on Pattern Analysis and Machine Intelligence 10, pp. 439-451, 1988

[Hal89] Halioua, M.; Liu, H.-C.: *Optical three-dimensional sensing by phase measuring profilometry*. Optics and Lasers in Engineering 11, pp. 185-215, 1989

[Häu08] Häusler, G.; Richter, C.; Leitz, K.-H; Knauer, M.C.: *Microdeflectometry – a novel tool to acquire three-dimensional microtopography with nanometer height resolution*. Opt. Lett. 33, pp. 396-398, 2008

[He91] He, X. D.; Torrance, K. E.; Sillion, F. X., Greenberg, D. P.: *A Comprehensive Physical Model for Light Reflection*. SIGGRAPH Comput. Graph. 25 , New York: ACM, pp. 175-186, 1991

[Hec01] E. Hecht: Optics. Reading: Addison-Wesley, 2001

[Höf13] Höfer, S.; Roschani, M., Werling, S.: *Pattern coding strategies for deflectometric measurement systems*. Proc. SPIE 8791, pp. 87911O-1-11, 2013

[Ike81] Ikeuchi, K.: *Determining Surface Orientations of Specular Surfaces by Using the Photometric Stereo Method*. Pattern Analysis and Machine Intelligence, IEEE Transactions on PAMI 3, pp. 661-669, 1981

[Jon15] Jonker, W.: *Final report on metrology based process control.* Project MEGaFiT (http://www.megafit-project.eu), expected to be published in February 2015

[Kes06] Kessler, R. W.: *Strategien für wissensbasierte Produkte und Verfahren*. In: Kessler, R. W. (Ed.): *Prozessanalytik: Strategien und Fallbeispiele aus der Industriellen Praxis.* Weinheim: Wiley-VCH, 2006.

[Kna04] Knauer, M. C.; Kaminski, J.; Häusler, G.: *Phase measuring deflectometry: a new approach to measure specular free- form surfaces.* Proc. SPIE 5457, pp. 366-376, 2004

[Kna06] Knauer, M.C.; Bothe, T; Lowitzsch, S.; Jüptner, W.; Häusler, G.: *Höhe, Neigung oder Krümmung?* Proc. DGaO 107, B30, URL: http://www.dgao-proceedings.de/download/107/107_b30.pdf , 2006

[Kow12] Kowalschuk, C.: *Möglichkeiten der Deflektometrie zur Verzugsmessung beim Laserstrahlschweißen im Mikrobereich*. MSc Thesis, Fraunhofer IPA / BIAS, 2012

[Li12] Li, W.; Sandner, M.; Gesierich, A.Burke, J.: *Absolute optical surface measurement with deflectometry*. Proc. SPIE 8494, pp. 84940G-1-7, 2012

[Li14] Li, L.; Zhao, W.; Wu, F.; Liu, Y.; Gu W.: *Experimental analysis and improvement on camera calibration pattern*. Optical Engineering 53, 2014

[Luh10] Luhmann, T.: *Erweiterte Verfahren zur geometrischen Kamerakalibrierung in der Nahbereichsphotogrammetrie*. Habilitation treatise, DGK, C 645, 2010

[MegF] EU Project MEGaFiT homepage, URL: http://www.megafit-project.eu

[Nad96] Nadeborn, W.; Andrä, P., Osten, W.: *A robust procedure for absolute phase measurement*. Optics and Lasers in Engineering 24, pp. 245-260, 1996

[Pet04] Petz, M.: *Rasterreflexions-Photogrammetrie zur Messung spiegelnder Oberflächen*. tm - Technisches Messen 71, pp. 389-397, 2004

[Pyz03] Pyzdek, T.; Keller, P. A.: *The six sigma handbook*. Vol. 486, New York: McGraw-Hill, 2003.

[Ray02] Ray, S. F.: *Applied Photographic Optics: Lenses and Optical Systems for Photography, Film, Video and Digital Imaging.* Focal Press, 2002.

[Reh13] Reh, Tobias; Li, W. Gesierich, A.; Bergmann, R. B.: *Vision Ray Camera Calibration for Small Field of View*. Proc. DGaO 114, A19, URL: http://www.dgao-proceedings.de/download/114/114_a19.pdf, 2013

[Sal91] Saleh, B. E. A.; Teich, M. C.: *Principles of Photonics*. New York: Wiley, 1991

[San88] Sanderson, A.; Weiss, L.; Nayar, S.: *Structured highlight inspection of specular surfaces*. IEEE Transactions on PAMI 10, pp. 44-55, 1988

[San11] Sandner, M.; Li, W.; Bothe, T.; Burke, J.; von Kopylow, C.; Bergmann, R. B.: *Absolut-Abstandsreferenz für die Streifenreflexionstechnik zur Verringerung systematischer Messfehler*. Proc. DGaO 112, A2, URL: http://www.dgao-proceedings.de/download/112/112_a2.pdf, 2011

[San12] Sandner, M.; Burke, J.; von Kopylow, C.; Bergmann, R. B.: *Messen und Prüfen mit Licht: Optische 3D-Formmesstechniken - hochauflösend, berührungslos und schnell.* wt Werkstattstechnik online 102, pp. 777-782, 2012

[San13] Sandner, M.; Li, W.; Burke, J.: *Sub-µm genaue Formmessung spiegelnder Oberflächen mittels Deflektometrie*. Proc. Oldenburger 3D-Tage 2013, Augsburg: Wichmann, pp. 208-216, 2013

[San14] Sandner, M.: *Reflection Characterization: 3D shape measurement of a surface using its diffuse and specular reflections.* Proc. DGaO 115, A29, URL: http://www.dgao-proceedings.de/download/115/114_a29.pdf, 2014

[Seß04] Seßner, R.; Häusler, G.: *Richtungscodierte Deflektometrie (RCD)*. Proc. DGaO 105, A16, URL: http://www.dgao-proceedings.de/download/105/105_a16.pdf, 2004

[Sch96] Schreiber, W.; Notni, G.; Kühmstedt, P;.Gerber. J.; Kowarischik, R.: *Optical 3D measurements of objects with technical surfaces*. In: Jüptner, W.; Osten, W. (ed.): Simulation and Experiment in Laser Metrology, Berlin: Akademie, 1996

[Wah86] Wahl, F. Hartmann, G. (ed.): *A Coded Light Approach for Depth Map Acquisition.* Mustererkennung 1986, Berlin Heidelberg: Springer, pp. 12-17, 1986

[Wik15] Wikipedia: *Geometrischer Schwerpunkt*. Online (Retrieved 16:14, January 6, 2015). URL:http://de.wikipedia.org/w/index.php?title=Geometrischer_Schwerpunkt&oldid=135555104 San Francisco: Wikimedia Foundation, 2014

[Wer11] Werling, S. B.: *Deflektometrie zur automatischen Sichtprüfung und Rekonstruktion spiegelnder Oberflächen*. KIT Scientific Publishing, 2011

[Wer11b] Werling, S.; Beyerer, J.: *Oberflächenrekonstruktion mittels Stereodeflektometrie*. tm - Technisches Messen 78, pp. 398-405 , 2011

[Woi13] Woizeschke, P.; Vollertsen, F: *Challenges of investigating distortion effects in laser micro welding*. In: Hinduja, S.; Li, L., Proceedings of the 37th International MATADOR Conference, Heidelberg: Springer, pp. 319-322, 2013

[Zha00] Zhang, Z.: *A flexible new technique for camera calibration*. Pattern Analysis and Machine Intelligence, IEEE Transactions on 22(11), pp.1330-1334, 2000

[Zwi11] Zwick, S.; Kühmstedt, P.; Notni, G.: *Phase-shifting fringe projection system using freeform optics*. Proc. SPIE 8169, pp. 81690W-1-9, 2011

10 Appendices

10.1 Implementation in FringeProcessor software

For Fringe Projection (FP) and HRR-based Phase Measuring Deflectometry (PMD) measurement and evaluation, the *FringeProcessor* software was modified. The modified version is *FringeProcessor* 5.7.1 B383 (BIAS SVN revision: 12245). The version used For ISR and RDR-based evaluation, *FringeProcessor* version 3.5.12 beta 9 was used as these algorithms had not yet been implemented into the 5.x versions. At the time this thesis is completed, ISR and RDR-based evaluation should be available in *FringeProcessor* version 6.

10.1.1 Implementation of Hybrid Reflectometry Regularization algorithm

In order to serve as initial shape for HRR-based PMD evaluation, data must be available in reference to the coordinate system of camera 1 shown in Figure 23b and Figure 25b. As the default output coordinate system for shape data from FP stereo camera setups in *FringeProcessor* 5.x is located between the cameras, the *FringeProjection* plugin was modified to allow output in the camera 1 coordinate system which can be set in the tool's *Preferences* dialog, see Figure 48.

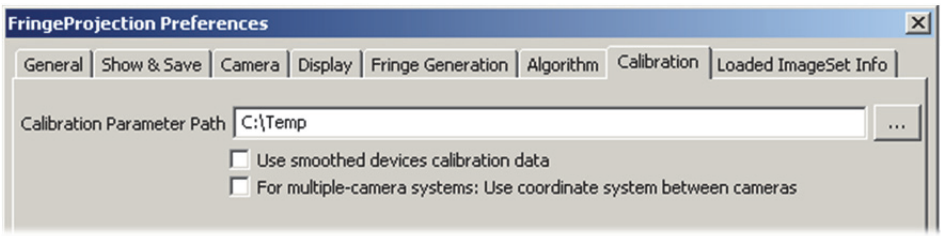

Figure 48: Preferences dialog of modified *FringeProjection* plugin (*Calibration* tab) in *FringeProcessor* 5.7.1 B383 software: For FP measurement of shape data as input for HRR-based PMD measurement evaluation, the lower checkbox ('For multiple-camera systems…') should be set to unchecked state in order to retrieve shape data in coordinate system of camera 1.

The *FringeReflectionHybrid* plugin (BIAS SVN revision: 12243) to be used for PMD phase measurement and HRR-based evaluation is a modified version of the *FringeReflection* plugin, in which the preparation of the input shape data from FP measurement is implemented. To use the plugin for HRR-based evaluation, the HRR algorithm has to be selected in the plugin's Preferences dialog (Radio button 'Pre-measured ini-shape', see Figure 49).

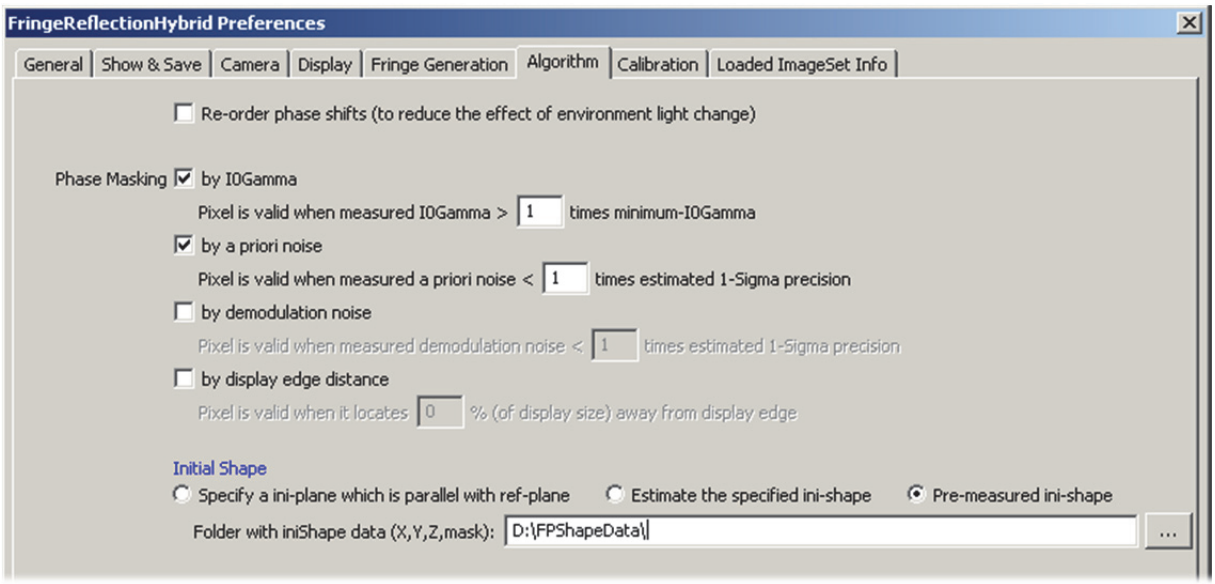

Figure 49: Preferences dialog of *FringeReflectionHybrid* plugin (*Algorithm* tab): For HRR-based evaluation, the radio button '*Pre-measured ini*-shape' should be selected, and the path to the input shape data from FP measurement should be set.

To perform measurement and evaluation using the Hybrid Reflectometry Regularization algorithm, the following steps must be performed:

1. Start *FringeProcessor* 5.7.1 B383
2. Perform FP measurement using the *FringeProjection* tool. Make sure that the output shape coordinate system is set correctly (see Figure 48).
3. Load (*X*,*Y*,*Z*) shape data and mask from FP measurement. If an interpolation of data is needed, prepare data validity mask and data output mask (see next section), and perform interpolation by selecting the '*Interpolate Data*' menu item.
4. Select '*Save (X,Y,Z) FringeProjection data for HybridReflectometry evaluation*' menu. Select the images as requested and select output directory which is set in the Preferences dialog, see Figure 49. The images will be renamed and copied to the given directory.
5. Perform PMD measurement. All data are generated automatically and saved to the paths set in the preferences (standard behavior for *FringeProcessor* measurement tools).

10.1.2 Developed pixel interpolation filter

The developed filtering algorithm for data interpolation has shape data, a data validity mask, and a data output mask, shown in Figure 50a, b and c respectively, as input parameters. The input shape data are copied to another image which is subsequently low pass filtered with a Gaussian kernel, with the size of the kernel being decreased in every iteration. The motivation behind this is to initially interpolate structures of low spatial frequency, such as offset, and iteratively add more energy of finer structures with high spatial frequency. In-between the filtering, values of pixels in the filtered image which are known to be valid (pixel value=true in data validity mask) are replaced by values from the original input image. In this fashion, valid data are used as seed points for the interpolation, with the influence zone of the seed points getting smaller in every iteration. After the last iteration step, valid data from the original image are again re-inserted into the filtered image, and the filtered image, shown in Figure 50d, is returned. The preparation of FP data described in section 7.3 was performed using 7 iterations and kernel sizes between 20x20 pixels (initial kernel size) to 3x3 pixels (final kernel size).

For the example shown below, the standard deviation was reduced by a factor of about 15, from 870 µm in an input shape image (Figure 50a) to 57 µm in the output image shown in Figure 50d, which is attributed mostly to the removal of extreme outlier values in small regions.

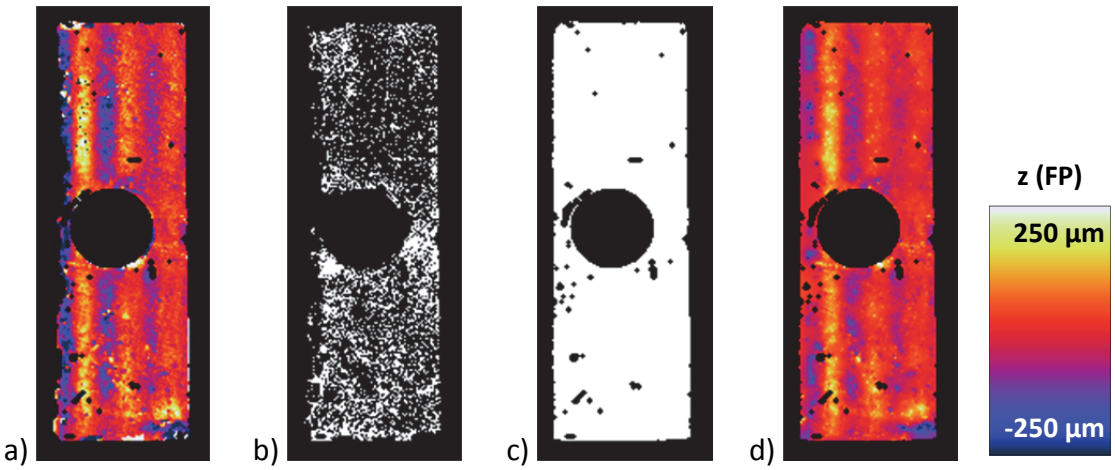

Figure 50: Filling of pixels with invalid data in shape image (tilt removed) with an iterative interpolation algorithm; a) Input shape data with local outliers (invalid pixels in black); b) Input mask for the interpolation algorithm generated from pixelwise standard deviation of repeated measurements; c) Output mask of the algorithm, computed from average *M* of a PMD measurement of the same object; d) Output shape image with interpolated pixel replacing pixels marked invalid in the mask shown in (b) (invalid pixels in black).

10.2 List of used abbrevations

arcsec	Arcseconds
BIAS	Bremer Institut für angewandte Strahltechnik
CCD	Charge coupled device
CMM	Coordinate measuring machine)
dpt	Diopter
EMVA	European machine vision association
FP	(Phase Measuring) Fringe Projection
RDR	Reference Distance regularization
GOP	Geometric-optical phase measurement technique
HRR	Hybrid Reflectometry regularization
IPS	In-plane switching
ISR	Initial Shape regularization
LCD	Liquid crystal display
PMD	Phase Measuring Deflectometry
SVN	Subversion - versioning and revision control system
TFT	Thin film transistor
TN	Twisted nematic
UV	Ultraviolet
VRC	Vision ray calibration

10.3 List of used symbols

Ap	Camera aperture plane
Δd_z	Deviation between estimated and actual object distance
Δr_n	Distance of the calculated penetration points in the monitor plane to the calculated ray of sight
Δz	One-dimensional error distribution in shape image
λ	Wavelength of light
Λ_c	Cut-off filter wavelength
θ_i θ_r	Incident angle, reflection angle
μ, μ_0	Permeability, vacuum permeability
σ	Standard deviation
σ_{Phase}	Estimated phase noise
σz_p	Pixelwise standard deviation
$\sigma(\sigma z_p)$	Standard deviation of pixelwise standard deviation
$\varphi(x,y)$	Phase of a sinusoidal pattern
φ_{PMD}	Phase of a sinusoidal pattern, from PMD measurement
Avg (σz_p)	Average of pixelwise standard deviation
B	Magnetic field
$\mathbf{c}_1$, $\mathbf{c}_2$, $\mathbf{c}_n$ $\mathbf{c}_s$, $\mathbf{c}_{s1}$, $\mathbf{c}_{s2}$	Camera pixel coordinates, $\mathbf{c}_{s1}$ = Pixel coordinate in camera 1, $\mathbf{c}_{s1}$ = Pixel coordinate in camera 2
$\mathbf{c}_{Ref}$	Camera pixel viewing reference point $\mathbf{p}_{Ref}$
$\mathbf{c}_p$	Projector pixel position
c_z	Center of area for sphere cap
d, d_z	Distance between camera aperture center and object point, component of this distance parallel to z – axis of reference plane coordinate system
d_{Ref}, $d_{z,Ref}$	Distance between camera aperture center and reference point on surface, component of this distance parallel to z – axis of reference plane coordinate system
E	Electrical field
f_c	Cost function in ISR evaluation
g (c_x, c_y)	Surface gradient
g	Grayscale value
g_{max}	Maximum grayscale value used for pattern display
h	Height of spherical cap
Ia	Camera image plane
I_1, I_2, I_3, I_4	Recorded intensities in phase measurement
M	Modulation of sinusoidal fringe pattern
n_i, n_1,n_2	Refractive index
n	Surface normal vector

List of used symbols (continued)

P	Period of a sinusoidal pattern
$\mathbf{p}_{Ap}$, $\mathbf{p}_{Ap,\#1}$, $\mathbf{p}_{Ap,\#2}$, $\mathbf{p}_{Ap}$, $\mathbf{p}_{Ap,\#1}$, $\mathbf{p}_{Ap,\#2}$, $\mathbf{p}_{Ap,\#n}$	Point in camera aperture
$\mathbf{p}_O$	Point on object surface
$\mathbf{p}_M$	Monitor pixel position
$\mathbf{p}_O$	Point on object surface
$\mathbf{p}_{Ref}$	Reference point on object surface
R_a	Arithmetical mean deviation of the roughness profile
$\mathbf{R}(R_x, R_y, R_z)$	Vector of Eulerian rotation angles
R_1, R_2, R_3, R_4	Surface regions
r_{fit}, $r_{fit,CMM}$, $r_{fit,FP}$	Output radius of numerical fit with spherical shape model r_{fit} for data from CMM, r_{fit} for data from FP
$\mathbf{r}_p$	Line of sight on monitor (mapped to monitor pixel position)
$\mathbf{r}_s$, $\mathbf{r}_{s,\#1}$, $\mathbf{r}_{s,\#2}$, $\mathbf{r}_{s,\#n}$ $\mathbf{r}_{s1}$, $\mathbf{r}_{s2}$	Camera ray of sight (mapped to sensor pixel position), $\mathbf{r}_s$ for camera 1, $\mathbf{r}_s$ for camera 2
r_{TE}, r_{TM}	Reflection coefficient for transversal electric incident, Reflection coefficient for transversal magnetic incident
$\mathbf{S}$, $\mathbf{S}_i$, $\mathbf{S}_t$	Poynting vector
s_{R3}	Lateral diameter of circular region R3 on measured surface
t_{mask}	Threshold value for mask generation
$\mathbf{T}(T_x, T_y, T_z)$	Translation vector
$U(z_p)$	Scalar wave function
$V_{c1}(\mathbf{X}_{c1}, \mathbf{Y}_{c1}, \mathbf{Z}_{c1})$	Coordinate system of camera 1
$V_{c2}(\mathbf{X}_{c2}, \mathbf{Y}_{c2}, \mathbf{Z}_{c2})$	Coordinate system of camera 2
$V_m(\mathbf{X}_m, \mathbf{Y}_m, \mathbf{Z}_m)$	Coordinate system of reference pattern display
$V_{Ref}(\mathbf{X}_{Ref}, \mathbf{Y}_{Ref}, \mathbf{Z}_{Ref})$	Coordinate system of reference plane in measurement volume
$(\mathbf{x},\mathbf{y},\mathbf{z})$	Coordinate system of reference plane in measurement volume (=V_{Ref})
x_{field}	Maximum width of measurement field
$(x_{PMD}, y_{PMD}, z_{PMD})$	Shape data calculated from PMD measurement (in $V_{Ref)}$
y	See (x, y, z)
y_{PMD}	See (x_{PMD}, y_{PMD}, z_{PMD})
z	See (x, y, z)
z_{Avg}.	Average value of input shape data
z_{FP}	z-coordinate from FP measurement
z_M	Axis of mechanical height measurement
z_{PMD}	See (x_{PMD}, y_{PMD}, z_{PMD})
z_p	Propagation distance
z_1 , z_2 , z_3	(Example) shape images from repeated measurements

10.4 Data sheets

Marlin F-146 camera (camera 1)

///ALLIED Vision Technologies SEEING IS BELIEVING

Specifications

Marlin	F-146B
Interface	IEEE 1394a - 400 Mb/s, 1 port
Resolution	1392 x 1040
Sensor	Sony ICX267
Sensor type	CCD Progressive
Sensor size	Type 1/2
Cell size	4.65 µm
Lens mount	C
Max frame rate at full resolution	17 fps
A/D	12 bit
On-board FIFO	8 MB
	Output
Bit depth	8-10 bit
Mono modes	Mono8, Mono16
	General purpose inputs/outputs (GPIOs)
Opto-coupled I/Os	2 inputs, 2 outputs
RS-232	1
	Operating conditions/Dimensions
Power requirements (DC)	8 V - 36 V
Power consumption (12 V)	<3 W
Mass	<120 g
Body Dimensions (L x W x H in mm)	72 x 44x 29 mm including connectors, w/o tripod and lens
Regulations	CE, FCC Class B, RoHS

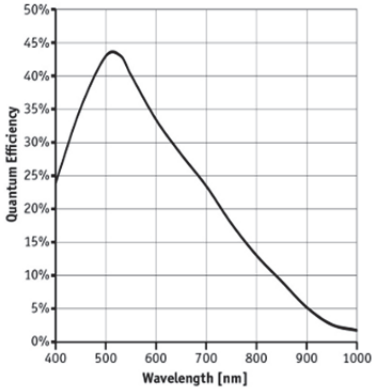

GT 1920 camera (camera 2)

///ALLIED Vision Technologies SEEING IS BELIEVING

Specifications

Prosilica GT	1920
Interface	IEEE 802.3 1000baseT
Resolution	1936 x 1456
Sensor	Sony ICX674
Sensor type	CCD Progressive
Sensor size	Type 2/3
Cell size	4.54 µm
Lens mount	C (adjustable)
Max frame rate at full resolution	40.7 fps
A/D	14 bit
On-board FIFO	128 MB
	Output
Bit depth	14 bit
Mono modes	Mono8, Mono12, Mono12Packed, Mono14
	General purpose inputs/outputs (GPIOs)
TTL I/Os	1 input, 2 outputs
Opto-coupled I/Os	1 input, 2 outputs
RS-232	1
	Operating conditions/Dimensions
Operating temperature	-20°C ... +60°C
Power requirements (DC)	PoE, or 7-25 VDC
Power consumption (12 V)	4.9 W @ 12 VDC
Mass	224 g
Body Dimensions (L x W x H in mm)	92 x 53.3 x 33 (including connectors, w/o tripod and lens)
Regulations	CE, FCC Class A, RoHS (2011/65/EU)

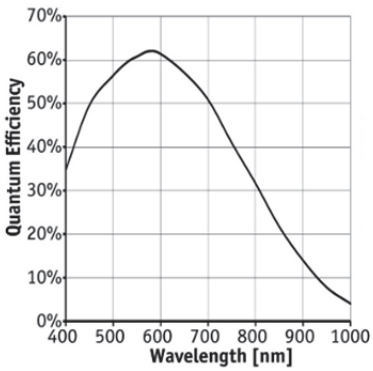

Pentax TV Lens (f=25 mm), used for camera 1 and camera 2

Manual, fixed focal lengths

FIXED FOCAL LENGTH, MANUAL IRIS
Megapixel, with Locking Screws

Part No.	Designation	Format size	Mount	Focal length	Iris range	M. O. D.	Horizontal angle of view	Filter size in mm	Specials
HIGH-RESOLUTION, FOR STANDARD, IP AND MEGAPIXEL CAMERAS									
C60636KP	H614-MQ (KP)	1/2"	C	6.0mm	1.4 - 16	0.20m	57.4°	30.5	compact, 32.0mm Ø
C61232KP	H1214-M (KP)	1/2"	C	12.0mm	1.4 - 16	0.25m	28.9°	27.0	compact, 29.5mm Ø
C31634KP	C1614-M (KP)	2/3"	C	16.0mm	1.4 - 16	0.25m	31.0°	27.0	compact, 29.5mm Ø
C32500KP	C2514-M (KP)	2/3"	C	25.0mm	1.4 - 16	0.25m	20.0°	27.0	compact, 29.5mm Ø
C33500KP	C3516-M (KP)	2/3"	C	35.0mm	1.6 - 16	0.40m	14.8°	27.0	compact, 29.5mm Ø
C35001KP	C5028-M (KP)	2/3"	C	50.0mm	2.8 - 22	0.90m	10.1°	27.0	compact, 29.5mm Ø
C37500KP	C7528-M (KP)	2/3"	C	75.0mm	2.8 - 32	0.70m	6.9°	30.5	compact, 34.0mm Ø

(KP): 3 locking screws on each of the aperture and focus rings plus 2 optional thumb screws

The M series had been developed as an extension of the existing series of lenses for image processing applications.

The overall image quality is kept high through many aspects. The picture geometry has been enhanced by reduced distortion and the lens resolution has been designed around the requirements of mega pixel sensors. The contrast of the image boarders exceeds the standard requirement many times over due to our new applied manufacturing technologies. These lenses are purposely designed to maximise picture performance at short distances. Also the lens coatings set new standards in quality and are ideal for taking images of particularly high-contrast scenes or intensely illuminated high-speed exposures.

Rodenstock Apo_Rodagon-N lens (f=50 mm), used for projector

Apo-Rodagon-N

Technical data

Lens	Maximum film format	Scale range	Smallest aperture	Pre-selection aperture	Click-stop disable	Illuminated f-stop display	Filter thread	Flange focal length [1]	Overall length	Max. diameter	Screw thread	Flange to rear edge
50 mm f/2.8	24×36 mm	2-20×	16	•	•	•	M 40.5×0.5	46.0 mm	46.5 mm	50.0 mm	M 39×1/26"	15.7 mm
80 mm f/4	6×7 cm	2-15×	22	•	•	•	M 40.5×0.5	77.0 mm	43.0 mm	50.0 mm	M 39×1/26"	12.2 mm
105 mm f/4	6×9 cm	2-15×	22	•	•	•	M 40.5×0.5	99.1 mm	54.3 mm	50.0 mm	M 39×1/26"	18.0 mm

[1]) Flange focal length at scale ∞

10.5 Acknowledgements

As a private conclusion on this thesis, I want to give thanks to the people who contributed to the success of this work.

At first I would like to thank Prof. Dr. Ralf B. Bergmann for giving me the chance to work at BIAS as a scientist, which motivated me to perform my Master's study program in parallel, and for trusting a priori in my ability to succeed in my studies.

I would like to thank my supervisors Prof. Dr. Jürgen Jahns from the University of Hagen and Dr. Jan Burke at BIAS, for supporting me and guiding my development as a scientist.

As I studied and worked on this thesis mostly at the BIAS laboratories and office, I spent much time there. From this, two separate acknowledgements derive:

- Having spent much time at BIAS, I would like to thank my colleagues at BIAS. A few examples, without the claim of completeness: Colin and Simon for philosophical discussions and hugs, Claas for an occasional pat on the shoulder and excellent scientific knowledge transfer, Tobi for discussions on this and that *and* topics closely related to my work, Vijay for being Vijay and the guys at MBS (material processing group at BIAS) for *keeping it real*.

- Having spent not that much time with my family, I would like to warmly thank May for paving the way for me to study and finish my thesis. Hugs go out to Nuri, I'm proud of you, my friend. I also want to thank the rest of my closer family (in alphabetical order: Aziz, Enno, Gisela, Lieselotte, Patrick & Sylvia) for not making me feel like I HAD to finish my studies, which in fact helped me a lot doing so. Moral support was also given to me by the Toro family and by Michael.

Last but not least I would like to thank the people who originally set me on track for what I am doing. I would not have chosen this path without the confidence given to me by my parents of course but, later on, also by the professors of my original study course, *Optotechnik und Bildverarbeitung* at the University of Applied Sciences in Darmstadt.